The Electric Field of a Weakly Electric Fish

Thesis by

Brian Rasnow

In Partial Fulfillment of the Requirements

for the Degree of

Doctor of Philosophy

California Institute of Technology

Pasadena, California

1994

(Submitted 14 March, 1994)

Acknowledgement

I owe a lot of gratitude to many who have helped me achieve this work. Foremost, to my wife and family, thank you for your patience, support, and alternative perspectives. After learning about weakly electric fish from Mark Konishi, Catherine Carr and Leonard Maler provided great encouragement to study these creatures. Jim Bower accepted and kindly supported the study of yet another sensory system in his lab. Thank you, Jim, for also accepting my unconventional and nonlinear trajectory through life and graduate school, and for your advice and support throughout these many years. I also owe special gratitude to Jerry Pine. Research in his lab taught me valuable lessons about experimental science, and after moving on, Jerry's door was always open for consultation. Mark Nelson and Chris Assad have been great partners in exploring electric fish. Thank you both, and may your pursuits be fruitful. To the many other students, staff, and faculty at Caltech, who have provided ideas, friendship, and more, sincere thanks. Finally, I thank the two managers of my farm in Costa Rica, and my good friends, Orlando Rojas and Abel Coto, for their extremely hard work in running Ganaderia Queberí. Este tesis no hubiera sido posible sin su apoyo. Understanding electric fish means little if they become extinct, thus a part of my work was to preserve their habitat.

Abstract

Freshwater fish of the genus *Apteronotus* (family Gymnotidae) generate a weak, high frequency electric field (<100 mV/cm, 0.5-10 kHz) which permeates their local environment. These nocturnal fish are acutely sensitive to perturbations in their electric field caused by other electric fish, and nearby objects whose impedance is different from the surrounding water. This thesis presents high temporal and spatial resolution maps of the electric potential and field on and near *Apteronotus*. The fish's electric field is a complicated and highly stable function of space and time. Its characteristics, such as spectral composition, timing, and rate of attenuation, are examined in terms of physical constraints, and their possible functional roles in electroreception.

Temporal jitter of the periodic field is less than 1 μsec. However, electrocyte activity is not globally synchronous along the fish's electric organ. The propagation of electrocyte activation down the fish's body produces a rotation of the electric field vector in the caudal part of the fish. This may assist the fish in identifying nonsymmetrical objects, and could also confuse electrosensory predators that try to locate *Apteronotus* by following its fieldlines. The propagation also results in a complex spatiotemporal pattern of the EOD potential near the fish. Visualizing the potential on the same and different fish over timescales of several months suggests that it is stable and could serve as a unique signature for individual fish.

Measurements of the electric field were used to calculate the effects of simple objects on the fish's electric field. The shape of the perturbation or "electric image" on the fish's skin is relatively independent of a simple object's size, conductivity, and rostrocaudal location, and therefore could unambiguously determine object distance. The range of electrolocation may depend on both the size of objects and their rostrocaudal location. Only objects with very large dielectric constants cause appreciable phase shifts, and these are strongly dependent on the water conductivity.

Table of Contents

Acknowledgement iii

Abstract iv

List of Illustrations vii

1. Introduction

1.1. What are Electric Fish? 1

1.2. Attributes of Electric Sense 4

1.3. Why Study Electric Fish? 7

1.4. Prior Knowledge and Contribution of this Research 9

References 12

2. Mapping Electric Fish Fields

2.1. Background 17

2.2. Hardware 20

2.3. Software 25

2.4. Calibration with a Dipole 29

2.5. Calibration with a Fish 37

References 41

Appendix 1. Electronics 42

Appendix 2. Vu Command Summary 47

3. The Electric Potential of *Apteronotus leptorhynchus*

Summary 50

3.1. Introduction 51

3.2. Materials and Methods 52

3.3. Results 57

3.4. Discussion 64

References 75

4. The Electric Field of *Apteronotus*

4.1. Introduction 78

4.2. Materials and Methods 79

4.3. Results 84

4.4. Discussion 97

References 107

5. The Effects of Simple Objects on the Electric Field of *Apteronotus*

5.1. Introduction 110

5.2. Methods 112

5.3. Results 113

5.4. Discussion 126

References 136

Appendix 1. A Sphere in a Uniform Electric Field 138

List of Illustrations

Chapter 2.

Fig. 2.1. Stability of the EOD 19

Fig. 2.2. Block diagram 21

Fig. 2.3. Electrode array and video frame 22

Fig. 2.4. Phase and dipole potentials 33

Fig. 2.5. Dipole calibration potentials 35

Fig. 2.6. Measured and simulated dipole potentials 36

Fig. 2.7. Dipole electric field components 38

Fig. 2.8. Differential vs. difference of potentials 39

Fig. A1.1. Bode plot of a recording electrode 43

Fig. A1.2. Bode plot of recording electronics 44

Fig. A1.3. Noise spectra 45

Fig. A1.4. Analog-to-digital converter performance 46

Chapter 3.

Fig. 3,1. Diagram of apparatus 54

Fig. 3.2. Stability of the EOD 58

Fig. 3.3. Spectral amplitudes and phase along the fish's midline 60

Fig. 3.4. Construction of the grayscale images 61

Fig. 3.5. Potential maps in the midplane and on the skin 62

Fig. 3.6. Comparison of the EOD between fish 64

Chapter 4.

Fig. 4.1. Stability of the EOD 85

Fig. 4.2. Cartesian field component waveforms 86

Fig. 4.3. Potential and field grayscale maps in the midplane 88

Fig. 4.4. Potential and field grayscale maps in the dorsoventral plane 89

Fig. 4.5. Spectral amplitudes and phases along three lines 91

Fig. 4.6. The electric field vector along the midline and back 94

Fig. 4.7. Electric field direction in midplane and dorsoventral plane 96

Fig. 4.8. Lateral decay rate of potential and field.....103

Chapter 5.

Fig. 5.1. Potential and perturbation below a conducting sphere 115

Fig. 5.2. Electric field components at the sphere 116

Fig. 5.3. Simulated and measured perturbation waveforms 118

Fig. 5.4. Simulated and measured perturbation amplitude vs. distance 119

Fig. 5.5. Attenuation rate of the potential perturbation 121

Fig. 5.6. Simulated and measured potential images 122

Fig. 5.7. Electric images from different field directions 123

Fig. 5.8. Offset and width of electric images 125

Chapter 1

Introduction

It is not enough that you should understand about applied science in order that your work may increase man's blessings. Concern for man himself and his fate must always form the chief interest of all technical endeavors, concern for the great unsolved problems of the organization of labor and the distribution of goods–in order that the creations of our mind shall be a blessing and never a curse to mankind. Never forget this in the midst of your diagrams and equations.

Albert Einstein in a 1938 address to the student body of the California Institute of Technology

1.1. What are Electric Fish?

This thesis is about an exercise in extrasensory perception. Whereas humans possess a variety of sensory modalities, other animals have evolved different sensory systems appropriate to their environments. In particular, numerous aquatic animals have acute sensitivity to electric fields, which are generated by muscle and nerve activity [1], [2] (often of prey), and the movement of the animal in the geomagnetic field (sharks may use this field for navigation [3]). In subsequent chapters, I will describe how a group of fish generate and sense electric fields for communication and detection of objects.

Electric sense has evolved independently at least five times [4]. An order of salamanders (Urodela) has demonstrated sensitivity to field strengths of 5 μV/cm [5].

The duck-billed platypus, a primitive egg-laying mammal (monotreme), was recently discovered to possess electroreceptors on its bill that are sensitive to 50 μV/cm low frequency fields [6]. This presumably helps them hunt invertebrate prey (they also dig up charged batteries buried in mud, and show a snapping reflex response to electric pulses when sleeping [7]). The echinda (spiny anteater), a terrestrial monotreme, is also electroreceptive [8], although behavioral thresholds to electric fields have not yet been established. Elasmobranchs (sharks, skates, and rays), lampreys, and possibly the coelocanth [9] –some of the most primitive living fish, are sensitive to field strengths ≤ 1 μV/cm below 10 Hz [10], and behavioral thresholds to fields as low as 5 nV/cm have been recorded [11].

In addition to detecting weak (and generally low frequency: DC-15 Hz) electric fields, some fish have developed effector organs for electrogenesis-the generation of stronger fields. A local field expands the fish's perception to include passive objects whose electrical impedances differ from the surrounding water. The electric field is also extensively utilized for communication between conspecifics [12]. In addition, two or possibly three groups of fish: electric rays (Torpedinoids); electric eels (Electrophoridae); and perhaps the "electric stargazer" (*Astroscopus*, Uranoscopidae), a mysterious saltwater fish [13], [14]; have electric discharges strong enough to immobilize prey. The majority of body tissue of the Amazonian electric eel is an electric organ, that can generate 1-2 msec pulses of 800 volts at one ampere [15].

This thesis examines so-called weakly electric fish, which produce ≤ 100 mV/cm fields that they use for communication and sensing their environment-or "electrolocation." There are two orders of freshwater weakly electric fish: the Gymnotiformes, living in the neotropics, and the Mormyriformes, found throughout Africa. There are hundreds of species within each order, most are nocturnal and many prefer turbid waters. In some species, vision is poor, and it is clear from their behavior that electric sense is their dominant sensory modality. For example, gravid females will

lay eggs in response to tape recordings of male electric discharge patterns played across electrodes [16].

Electric fish generate their field with specialized "electric organs" (EO) consisting (in all but one Gymnotid family, *Apteronotus*) of series and parallel piles of modified muscle cells, that produce sodium action potentials instead of contracting [17]. In some species, the EO is short and located near the end of the tail, and in other species, the EO runs nearly the entire length of the fish. Many electric fish have greatly elongated bodies and long point like tails that are nearly completely filled with electric organ tissue. Such fish swim by generating traveling waves along a dorsal or ventral fin, which propels them forward or backwards with almost equal ease while maintaining their bodies rigid. These fish often probe novel objects with their tail while swimming backwards, and demonstrate other behaviors which are not seen in non-electrosensory fish [18].

The electric field is transduced and sensed by several thousand electroreceptor organs in the fish's skin [19]. The neural coding of the electric field by these receptors is complicated and still a subject of active study [20], [21]. In general, the receptor organs have been classified into three classes. "Ampullary receptors" morphologically and physiologically resemble the electroreceptors of electrosensitive fish without electric organs [22]. They have high sensitivity to low frequency ambient fields (< 30 Hz). A second receptor class encodes phase and timing of the fish's EOD, and a third class encodes EOD amplitude [23], [24]. However, there is considerable overlap between the two high frequency receptor classes [25], [26]. For example, a recent study showed that a Mormyrid receptor previously classified as an amplitude coder responded to phase shifts of < 1 μsec [21]. In wave fish, the amplitude coding receptors are tuned (i.e., have lowest threshold) to the fish's own EOD frequencies [27].

The electroreceptor organs consist of a tube or ampulla, filled with a high conductivity jelly, that runs from the fish's outermost skin layers to the receptor cell

bodies [28], [29], which are derived from hair cells (acoustic transducers) [30]. The receptor cells are surrounded by support cells that form high impedance tight junctions, thus channeling the current through the active membranes. The electroreceptors project to a brain structure called the electrosensory lateral line lobe (ELL) located in the medulla [19], [31], [32]. The ELL is remarkably similar in structure to the cerebellum [33]. Furthermore, the cerebellum of many species of electric fish is the largest of any animal in proportion to their brain size, constituting over half the fish's brain [34]. Some electric fish have brain-to-body mass ratios similar to humans. These are among the largest relative brain sizes in vertebrates.

Generating an electric field takes energy, and nature has chosen two strategies for maximizing field strength at minimal expense. Some "pulse fish," such as the above mentioned electric eel, generate brief current pulses, lasting from < 100 μsec (an impressive feat since typical neurons fire 1 msec duration pulses) to 50 msec, depending on the species [35]. The fish is electrically blind to passive objects between discharges, but by operating at low duty cycle, it can increase the pulse energy, and therefore the range, of its electric sense. However, by making the pulse short, the fish is spreading its energy across a wide frequency spectrum, which increases noise.

"Wave fish" such as *Apteronotus* take an alternative approach to minimize noise and energy expenditure by generating a continuous, periodic discharge, with fundamental at 100 Hz - 2 kHz, depending on species. In contrast to pulse fish, these fish sample their environment at discrete points in the frequency domain. Wave and pulse fish have evolved independently within both families of freshwater weakly electric fish.

1.2. Attributes of Electric Sense

Electric sense differs from other modalities in a number of fundamental ways. Like bat echolocation and dolphin sonar, the sensory stimulus originates from the

animal. Thus the fish's behavior, particularly tail angle and body position, will have profound sensory consequences. In modalities which detect an exogenous sensory field such as vision, movement of the receptor array (head or eye) causes a shift in the stimulus pattern. However in the case of the fish's endogenous electric field, movement of the fish's body repositions both the field sources and detectors. How these fish deconvolve an object's motion from that of its electric organ and receptors remains an open question.

The spatial range of electric sense is much less than vision [36]. The far field, beyond a few body lengths, is dipolar and thus attenuates with the third power of distance. Fish can detect the discharge of conspecifics within approximately 5-10 body lengths. However, it has been demonstrated behaviorally that fish can only electrolocate passive objects in their near field [37]. For the simplest object-a small conductive or dielectric sphere, the fish's electric field induces a dipole moment proportional to the cube of the object's radius and the field at the object. Moving the sphere away from the fish results in a smaller induced dipole moment from the attenuated fish field, and additional attenuation from the larger distance between the perturbation dipole and the fish's electroreceptors. Although the near field attenuates with distance from the fish less rapidly than the far field, the perturbation attenuates faster than the fish's field.

Electric fish partially compensate for the steep distance dependence of electric sense computationally. Neurons have been isolated in the cerebellum that show greater constancy in their firing rates to electric field modulations than do the electroreceptors and ELL neurons involved in earlier stages of electrosensory information processing [38]. Other regions of cerebellum send feedback to ELL, possibly as a gain control signal to adjust the neuron's relatively limited dynamic range within the larger dynamic range of peripheral stimuli [39], [40].

The spatial resolution of electric sense is considerably inferior to vision. Fish have no electrical analogy to the lens of the eye, so electric fields cannot be focused on

the receptor array. Spatial resolution depends on both receptor density and the geometry of electric perturbations. The receptor density is highly variable over the fish's body [19]. At the head, there are several high frequency receptor organs per square mm, and substantially fewer on the trunk and tail. The genus, *Apteronotus*, also has a dense line of electroreceptors running along its back, called the dorsal filament, whose role in electric sense is still unclear [41]. Electric "images" or perturbations of the fish's field due to objects are also of relatively low spatial resolution (Chapter 5). High spatial frequency features, or multipole moments, of an image rapidly attenuate with distance from an object as the current spreads through the water.

The temporal acuity of electric sense is excellent, because the EOD field does not propagate as a wave, but exists as an electrostatic field [42]. Dispersion in water at EOD frequencies is negligible and there are no perceptible delays in the arrival times of signals from different places. In comparison, acoustic signals, which propagate in air and water at approximately 0.3 and 1.5 mm/μsec respectively, are distorted by diffraction, interference, echoes, etc. Whereas vegetation and the ground have profound effects on the acoustic properties of bird songs [43, 44], the temporal properties of electrical signals will be minimally affected by environmental transmission. It is likely for this reason that the spectral composition of EODs span a much wider bandwidth than acoustic signals. For example, Hopkins [45] found the dominant frequencies of 23 sympatric species ranged from 150 Hz to 12 kHz, or 7 octaves. In comparison, the dominant frequencies of all North American bird species span 3 octaves [46].

Many species of electric fish use waveform and temporal cues of their EOD for species and sex recognition [47]. Novel coding mechanisms, such as scan sampling (similar to the method used in high speed sampling oscilloscopes), have been suggested to account for the temporal hyperacuity these fish display [48], [49]. Although temporal cues in EOD signals clearly are an important element in communication between fish [50], [51], their role in electrolocation of passive objects remains uncertain.

Summarizing the physical model of an electric fish as was established before my research (substituting data from a potpourri of electric fish species where comparable data is not available for *Apteronotus.*), the electric organ of a 22 cm *Apteronotus* behaves as a current source with dipole moment approximately 1 mA-cm in 2 kΩ-cm^2 water [52]. The poles are stationary, separated by approximately 6 cm, and oscillate with opposite phase. Sensitivity thresholds measured by behavioral experiments suggest such a fish could be detected by conspecifics within a 1.5 meter radius (*Eigenmannia*) [52], and 2 mm cylinders are detectable within a few cm (*Eigenmannia* and mormyrids–the range for *Apteronotus* may be less because they have an order of magnitude weaker EOD). The fish live in water of highly variable resistivity (ρ = 2-100 kΩ-cm; *Apteronotus*) [37]. The body interior is a good conductor (ρ = 100Ω-cm; *Eigenmannia*) and is isopotential [53]. The skin has a high impedance (ρ = 1-4 kΩ-cm^2; *Eigenmannia*) [53], an order of magnitude larger than nonelectric freshwater fish [54]. The electroreceptor organs are situated at the base of the fish's skin, below a canal filled with conductive jelly and surrounded by insulating tight junctions [17]. This geometry channels current across the active membranes of the receptor cells. It has not been clearly shown whether the tuberous electroreceptors are primarily voltmeters or current meters [53], [2], [55]. By measuring the startle response to uniform electric fields in water with different conductivity, Knudsen [37] showed that the current density threshold was a function of water resistivity. This data suggests the receptors are neither ideal current meters or voltmeters.

1.3. Why Study Electric Fish?

Scientists have been aware of the discharge of strongly electric fish since at least 1786 [56]. That weakly electric fish were indeed electrogenic was not discovered until 1951 [57]. Using the twitch of a freshly dissected frog's sciatic muscle as a voltmeter, Lissmann showed that Mormyrids produce weak electric discharges. In just a few

decades, electric fish went from a zoological curiosity to become one of the best understood neuroethological systems. There are many reasons for this extraordinary success. For example, it is relatively easy to noninvasively eavesdrop on the sensory stimulus, the EOD, which is also a motor output. The sensory receptor organs are not tightly crammed into complex and inaccessible structures, such as the retina and cochlea. The neural circuitry associated with at least the initial stages of electrosensory information processing and electrogenesis is simple (relative to most other vertebrate sensory systems). Electric fish also have a rich repertoire of stereotypical behaviors that have been used, for example, to assay sensitivity thresholds [58].

The brains of most electric fish are unusual in the similar structure of cerebellum and ELL, and the enormous hypertrophy of cerebellum. This suggests that cerebellar circuitry is somehow optimal for the kinds of computation electric fish perform on their electrosensory input stream. The neuroanatomy of cerebellum is nearly constant in animals from primitive fish to humans. Its involvement in sensorimotor function of the organism has been recognized for nearly 100 years, yet its computational function remains unproven. Much of the difficulty of understanding cerebellar computation can be attributed to the unknown coding of its inputs and outputs, which are both several synapses from the sensory periphery and motor neurons. In contrast, ELL granule cells are one synapse distant from peripheral electrosensory input.

Understanding the general principles of sensorimotor systems, including the function of cerebellum, may have profound applications to a wide variety of scientific and engineering fields, including theories of computation and computability, complex systems, self-organization, robotics, etc. In particular, poor coupling between sensory and motor systems is one of the major obstacles facing the field of robotics. The transduction and coding of electrosensory information has revealed novel coding schemes, which along with the associated neural circuitry, may have significance to the growing applications of artificial neural network computations. Relevance to general

issues in biology and neurobiology has repeatedly emerged from electric fish studies, often unexpectedly. Bullock lists some of these contributions: transduction and neural coding; serial and parallel processing; hodology and circuit analysis; convergence of modalities; sensorimotor integration; function of the cerebellum, tectum, and other central nervous system structures; ontogenetic, ethological, and ecological strategies; homology and homoplasy; and repeated appearance and loss in evolution [59].

1.4. Prior Knowledge and Contribution of this Research

Prior to my research on electric fish, only low resolution measurements had been made of the electric potential on the fish's skin, and no measurements existed of the vector electric field. Elaborating on Lissmann's sketches of a dipolar field, Knudsen mapped the far field amplitude of several weakly electric fish species at approximately 5 cm resolution [52]. He described the fish, "...as a field source, represents a distributed rostral pole and a point-like caudal pole (Fig. 2)." Although he noted that the near field deviated from this simple description, the details were largely ignored. Hoshimiya et al. published the first measurements and analysis of the complicated near field of *Apteronotus* [60]. They measured the potential with an array of 32 electrodes, and constructed an analog electronic circuit that showed how superposition of phase-shifted electrocyte-like signals might generate the complex waveforms. However, no functional significance was attributed to the "complex" EOD.

A number of elegant behavioral studies showed the limits of what electric fish can detect. Lissmann first demonstrated electrolocation by training *Gymnarchus* to discriminate between porous pots containing objects of different conductivity [61]. *Gymnarchus* could detect the presence of 2 mm but not 0.8 mm diameter glass rods within 2.5 cm pots. Some fish naturally follow the movement of nearby objects (this likely affords them camouflage in swaying vegetation). Heiligenberg [62] found that *Eigenmannia* would barely follow an oscillating 2 mm thick plexiglass rod at a lateral

distance of 3 cm. Other species tend to rest on the tank bottom. These show a startle response when they detect a change in their electrical environment. In a number of species tested, thresholds were 1-4 cm for 4 mm plexiglass cylinders [62]. Startle responses also have shown that electric fish can distinguish between resistive and capacitive shunts with similar impedance magnitude [63], [64].

What does an object do to a fish's electric field that makes it detectable? Measurements of object perturbations were first obtained using metal and plastic sheets [23], [53]. These experiments didn't attempt to measure the voltage perturbations at the fish's skin. Instead, they recorded the electrophysiological responses of electroreceptors as the objects passed nearby. Bastian later measured EOD amplitude perturbations by rectifying and low-pass filtering the signal from a stationary electrode on the fish's skin as objects passed above the electrode [38]. Temporal and phase information was lost by averaging, but perhaps more importantly, the spatial characteristics of electric images could only be estimated indirectly because the measurements were all from a single point.

Unable to accurately measure the minute perturbations due to small objects, Heiligenberg [65] pioneered computer simulations of the fish's field and object perturbations. His coarse 2-dimensional finite difference model provided the first "view" of electric images and some of their spatial properties. This was followed by 2-dimensional finite element simulations of electric images (on an elliptical fish) [60]. Bacher extended these simulations to 3-dimensions, using a pair of line charges to model the fish, and a dipole for the object [66]. These simulations revealed several fundamental properties of electric images, such as their low resolution and range. However, for the most part, they did not explain how electric fish might extract relevant features of an object from its electric image. For example, how the size, shape, distance, and impedance of an unknown object could be determined from a fuzzy pattern of small voltage changes across a fish's skin is not obvious.

Electric sense is foreign and unintuitive, but it is arguable whether our intuition about other modalities has actually helped (or perhaps hindered) our understandings of their operating principles. In this thesis, I have attempted to improve our intuition about electric sense. Chapter 2 explains the apparatus and methodology I developed for mapping electric fish fields. Chapter 3 shows maps of the electric organ discharge potential of *Apteronotus leptorhynchus*. These maps reveal a wealth of high spatial and temporal frequency information present in the fish's near field. This approach of visualizing the fish's electric organ discharge is continued in Chapter 4, which presents maps of the electric field vector. In Chapter 5, the electric field data are used to simulate electric images of objects. Analysis of these images suggests algorithms that could be used by electric fish to determine object distance, location, size, and impedance.

References

[1] Montgomery, J.C., & Bodznick, D., "Hindbrain Circuitry Mediating Common Mode Suppression of Ventilatory Reafference in the Electrosensory System of the Little Skate, *Raja erinacea*," *J. Exp. Biol.*, **183**:203-215, 1993.

[2] Kalmijn, J., "The Detection of Electric Fields from Inanimate and Animate Sources other than Electric Organs," in *Electroreceptors and Other Specialized Receptors in Lower Vertebrates*, Fessard, A. (Ed.), chap. 5, pp. 147-200, Springer-Verlag, 1974.

[3] Kalmijn, A.J., "Experimental Evidence of Geomagnetic Orientation in Elasmobranch Fishes," in *Animal Migration, Navigation, and Homing*, Schmidt-Koenig, J., & Keeton, W.T. (Eds.), pp. 347-353, Springer-Verlag, 1978.

[4] Bullock, T.H., Bodznick, D.A., & Northcutt, R.G., "The Phylogenetic Distribution of Electroreception: Evidence for Convergent Evolution of a Primitive Vertebrate Sense Modality," *Brain Res. Rev.*, **6**:25-46, 1983.

[5] Fritzsch, B., & Wahnschaffe, U., "The Electroreceptive Ampullary Organ of *Urodeles*," *Cell Tissue Res.*, **299**:483-503, 1983.

[6] Scheich, H., Langer, G., Tedemann, C., Coles, R., & Guppy, A., "Electroreception and Electrolocation in Platypus," *Nature*, **319**:401-402, 1986.

[7] Gregory, J., "New results on Platypus," presented at the Electrosensory Systems Conference, Montreal, Canada, Aug. 1992.

[8] Andres, K.H., von Düring, M., Iggo, A., & Proske, U., "The Anatomy and Fine Structure of the Echidna *Tachyglossus aculeatus* Snout with Respect to its Different Trigeminal Sensory Receptors Including the Electroreceptors," *Anat. Embryol.*, **184**:371-393, 1991.

[9] Northcutt, R.G., "Anatomical Evidence of Electroreception in the Coelocanth (*Latimeria chalumnae*)," *Zentralbl. Vetrinaermed. Reihe*, **C 9**:289-295, 1980.

[10] Ronan, M., "Elecctroreception in Cyclostomes," in *Electroreception*, Bullock , T.H., & Heiligenberg, W. (Eds.), chap. 7, pp. 209-224, Wiley & Sons, 1986.

[11] Kalmijn, J., "Electro-perception in Sharks and Rays," *Nature*, **212**:1232-1233 , 1966.

[12] Hopkins, C.D., "Electric Communication in Fish," *Amer. Sci.*, **62**:426-437, 1974.

[13] Dahlgren, U., "The Life History of the Fish, *Astroscopus*," *Sci. Monthly*, **24**:348-365, 1927.

[14] Pickens, P.E., & McFarland, W.N., "Electric Discharge and Associated Behavior in the Stargazer," *Animal Behavior*, **12**:362-367, 1964.

[15] Keynes, R.D., & Martins-Ferreira, H., "Membrane Potentials in the Electroplates of the Electric Eel," *J. Physiol.*, **119**:315-351, 1953.

[16] Hagedorn, M., "The Ecology, Courtship, and Mating of Gymnotiform Electric Fish," in *Electroreception*, Bullock, T.H., & Heiligenberg, W. (Eds.), pp. 497-525, Wiley, 1986.

[17] Bennett, M.V.L., "Electric Organs," in *Fish Physiology*, Hoar, W.S., & H., R.D. (Eds.), pp. 347-491, Academic Press, 1971.

[18] Toerring, M.J., & Belbenoit, P., "Motor Programmes and Electroreception in Mormyrid Fish," *Behav. Ecol. Sociobiol.*, **4**:369-379, 1979.

[19] Carr, C.E., Maler, L., & Sas, E., "Peripheral Organization and Central Projections of the Electrosensory Nerves in Gymnotiform Fish," *J. Comp. Neurol.*, **211**:139-153, 1982.

[20] Nelson, M.E., Payne, J.R., & Xu, Z., "Modeling and Simulation of Primary Electrosensory Afferent Response Dynamics in the Weakly Electric Fish, *Apteronotus leptorhynchus*," *J. Comp. Physiol. A*, **173**:746, 1993.

[21] von der Emde, G., "Extreme Phase Sensitivity of Afferents Which Innervate Mormyromast Electroreceptors," *Naturwissenschaften*, **79**:131-133, 1992.

[22] Fessard, A., & Szabo, T., "Physiology of Receptors II. Perhpheral Mechanisms of Electroreceptors in Teleosts," in *Handbook of Sensory Physiology*, Fessard, A. (Ed.), pp. 64-95, Springer-Verlag, 1974.

[23] Hagiwara, S., Szabo, T., & Enger, P.S., "Electroreceptor Mechanisms in a High Frequency Weakly Electric Fish, *Sternarchus albifrons*," *J. Neurophys.*, **28**:784-799, 1965.

[24] Scheich, H., Bullock, T.H., & Hamstra, R.H., "Coding Properties of Two Classes of Afferent Nerve Fibers: High-Frequency Electroreceptors in the Electric Fish, *Eigenmannia*," *J. Neurophys.*, **36**:39-60, 1973.

[25] Viancour, T.A., "Electroreceptors of a Weakly Electric Fish. I. Characterization of Tuberous Receptor Organ Tuning," *J. Comp. Physiol.*, **133**:317-325, 1979.

[26] Viancour, T.A., "Electroreceptors of a Weakly Electric Fish. II. Individually Tuned Receptor Oscillations," *J. Comp. Physiol.*, **133**:327-338, 1979.

[27] Hopkins, C.D., "Stimulus Filtering and Electroreception: Tuberous Electroreceptors in Three Species of Gymnotid Fish," *J. Comp. Physiol.*, **111**:171-207, 1976.

[28] Szabo, T., "Anatomy of the Specialized Lateral Line Organs of Electroreception," in *Handbook of Sensory Physiology*, Fessard, A. (Ed.), pp. 13-58, Springer-Verlag, 1974.

[29] Bennett, M.V.L., Sandri, C., & Akert, K., "Fine Structure of the Tuberous Electroreceptor of the High-Frequency Electric Fish, *Sternarchus albifrons* (gymnotiformes)," *J. Neurocytology*, **18**:265-283, 1989.

[30] Northcutt, R.G., & Gans, C., "The Genesis of Neural Crest and Epidermal Placodes: A Reinterpretation of Vertebrate Origins," *Q. Rev. Biol.*, **58**:1-28, 1983.

[31] Shumway, C.A., "Multiple Electrosensory Maps in the Medulla of Weakly Electric Gymnotiform Fish. I. Physiological Differences," *J. Neurosci.*, **9(12)**:4388-4399, 1989.

[32] Shumway, C.A., "Multiple Electrosensory Maps in the Medulla of Weakly Electric Gymnotiform Fish. I. Anatomical Differences," *J. Neurosci.*, **9(12)**:4400-4415, 1989.

[33] Meek, J., "Why Run Parallel Fibers Parallel? Teleostean Purkinje Cells as Possible Coincidence Detectors, in a Timing Device Subserving Spatial Coding of Temporal Differences," *Neuroscience*, **48**:249-283, 1992.

[34] Nieuwenhuys, R., & Nicholson, C., "A Survey of the General Morphology, the Fiber Connections, and the Possible Functional Significance of the Gigantocerebellum of Mormyrid Fishes," in *Neurobiology of Cerebellar Evolution and Development*, Llinas, R. (Ed.), pp. 107-134, American Medical Assn., 1969.

[35] Hopkins, C.D., & Heiligenberg, W.F., "Evolutionary Designs for Electric Signals and Electroreceptors in Gymnotid Fishes of Surinam," *Behav. Ecol. Sociobiol.*, **3**:113-134, 1978.

[36] Bastian, J., "Electrolocation I. How the Electroreceptors of Apteronotus albifrons Code for Moving Objects and Other Electrical Stimuli," *J. Comp. Physiol.*, **144**:465-479, 1981.

[37] Knudsen, E.I., "Behavioral Thresholds to Electric Signals in High Frequency Electric Fish," *J. Comp. Physiol.*, **91**:333-353, 1974.

[38] Bastian, J., "The Range of Electrolocation: A Comparison of Electroreceptor Responses and the Responses of Cerebellar Neurons in a Gymnotid Fish," *J. Comp. Physiol.*, **108**:193-210, 1976.

[39] Bastian, J., "Gain Control in the Electrosensory System: A Role for the Decending Projections of the Electrosensory Lateral Line Lobe," *J. Comp. Physiol.*, **158**:505-515, 1986.

[40] Maler, L., "The Role of Feedback Pathways in the Modulation of Receptive Fields: An Example from the Electrosensory System," in *Neural Mechanisms of Behavior: Proceedings of the 2nd International Congress of Neuroethology,* Erber, J., Thieme, 1989, pp. 111-115.

[41] Franchina, C., Hopkins, C.D., & Schneiderman, A., "The Dorsal Filament of the Weakly Electric Apteronotids is Specialized for Electroreception," in *Soc. Neurosci. Abstr.,* 16:1990, pp. 1327.

[42] Hopkins, C.D., "Temporal Structure of Non-Porpagated Electric Communication Signals," *Brain Behav. Evol.*, **28**:43-59, 1986.

[43] Richards, D.G., & Wiley, R.H., "Reverberations and Amplitude Fluctuations in the Propagation of Sound in a Forest: Implications for Animal Communication," *Am. Nat.*, **115**:381-399, 1980.

[44] Embleton, T.F.W., "Sound Propagation in Homogeneous Deciduous and Evergreen Woods," *J. Acoust.Soc. Am.*, **35**:1119-1125, 1963.

[45] Hopkins, C.D., "Evolution of Electric Communication Channels in Mormyrids," *Behav. Ecol. Sociobiol.*, **7**:1-13, 1980.

[46] Brenowitz, E.A., "Environmental Influences on Acoustic and Electric Animal Communication," *Brain Behav. Evol.*, **28**:32-42, 1986.

[47] Hopkins, C.D., & Bass, A.H., "Temporal Coding of Species Recognition Signals in an Electric Fish," *Science*, **212**:85-87, 1981.

[48] Hopkins, C.D., & Max Westby, G.W., "Time Domain Processing of Electric Organ Discharge Waveforms by Pulse-Type Electric Fish," *Brain Behav. Evol.*, **29**:77-104, 1986.

[49] Kawasaki, M., Rose, G., & Heiligenberg, W., "Temporal Hyperacuity in Single Neurons of Electric Fish," *Nature*, **336**:173-176, 1988.

[50] Shumway, C.A., & Zelick, R.D., "Sex Recognition and Neural Coding of Electric Organ Discharge Waveform in the Pulse-Type Weakly Electric Fish, Hypopomus occidentalis," *J. Comp. Physiol.*, **163**:465-468, 1988.

[51] Heiligenberg, W., & Altes, R., "Phase Sensitivity in Electroreception," *Science*, **199**:1001-1004, 1978.

[52] Knudsen, E., "Spatial Aspects of the Electric Fields Generated by Weakly Electric Fish," *J. Comp. Physiol.*, **99**:103-118, 1975.

[53] Scheich, H., & Bullock, T.H., "The Detection of Electric Fields from Electric Organs," in *Handbook of Sensory Physiology*, Fessard, A. (Ed.), pp. 201-256, Springer-Verlag, 1974.

[54] Bullock, T.H., Hamstra, R.H., & Scheich, H., "The Jamming Avoidance Response of High Frequency Electric Fish," *J. Comp. Physiol. Psychol.*, **77**:1-48, 1972.

[55] Bennett, M.V.L., "Electroreception," in *Fish Physiology*, Hoar, W.S., & H., R.D. (Eds.), pp. 493-574, Academic Press, 1971.

[56] Cavallo, T., *A Complete Treatise on Electricity, In Theory and Practice*, 2: C. Dilly (London), 1786.

[57] Lissmann, H.W., "Continuous Electrical Signals from the Tail of a Fish, Gymnarchus niloticus Cuv.," *Nature*, **167**:201-202, 1951.

[58] Heiligenberg, W., "The Neural Basis of Behavior: A Neuroethological View," *Ann. Rev. Neurosci.*, **14**:247-268, 1991.

[59] Bullock, T.H., & Heiligenberg, W., *Electroreception*, John Wiley & Sons, Inc., 1986.

[60] Hoshimiya, N., Shogen, K., Matsuo, T., & Chichibu, S., "The Apteronotus EOD Field: Waveform and EOD Field Simulation," *J. Comp. Physiol.*, **135**:283-290, 1980.

[61] Lissmann, H.W., "On the Function and Evolution of Electric Organs in Fish," *J. Exp. Biol.*, **35**:156-191, 1958.

[62] Heiligenberg, W., *Principles of Electrolocation and Jamming Avoidance in Electric Fish*, Springer Verlag, 1977.

[63] Meyer, J.H., "Behavioral Responses of Weakly Electric Fish to Complex Impedances," *J. Comp. Physiol.*, **145**:459-470, 1982.

[64] von der Emde, G., & Ringer, T., "Electrolocation of Capacitive Objects in Four Species of Pulse-type Weakly Electric Fish," *Ethology*, .

[65] Heiligenberg, W., "Theoretical and Experimental Approaches to Spatial Aspects of Electrolocation," *J. Comp. Physiol.*, **103**:247-272, 1975.

[66] Bacher, M., "A New Method for the Simulation of Electric Fields, Generated by Electric Fish, and their Distorsions by Objects," *Biol. Cybern.*, **47**:51-58, 1983.

Chapter 2

Mapping Electric Fish Fields

2.1. Background

In this chapter I describe the apparatus I have constructed to measure and map the electric field and potential produced by weakly electric fish. I first measured a fish's electric organ discharge (EOD) with a couple of kitchen forks in the fish tank connected to my stereo. The clicks of *Gnathonemus*[1] were unmistakable, despite terrible 60 Hz interference. This simple living-room experiment showed that these fish generate a substantial field that, with more suitable electronics, could be measured with high fidelity. I also observed that the fish's behavior was correlated with its EOD pulse rate. I wondered how would the electric field correlate with behavior? *Gnathonemus* generates its field with a short electric organ (EO) in its tail, therefore tail bending would strongly affect the field geometry. The fish's position and orientation relative to objects could also have profound sensory consequences. To explore these issues, I needed to visualize the fish's electric field.

Measuring the potential around *Gnathonemus* proved difficult because the first notable effect of anesthetics and paralytic drugs was complete abolition of the EOD. There is one genus of weakly electric fish that can be paralyzed without affecting the EOD [1]. *Apteronotus* (Family Gymnotidae), have electric organs consisting of modified spinal nerve endings, thus curare, a paralytic drug that blocks neuromuscular synaptic transmission, has no effect on the EOD (the EO of all other weakly electric fish is

---

[1] *Gnathonemus petersii* or the elephant nose fish generates a 100 μsec biphasic pulse at 0.5 - 20 Hz.

derived from muscle tissue). Instead of generating brief pulses, *Apteronotus* generates a continuous electric discharge of constant frequency. The *Apteronotus* EO is the most stable and fastest known neural oscillator (the fundamental of some species is > 2 kHz) [2]. Instead of sampling its environment at discrete times as do pulse fish, *Apteronotus* samples at discrete frequencies.

My first measurements of immobilized *Apteronotus* confirmed that not only was the fundamental frequency highly stable, but so was every detail of the waveforms, even in regions of the fish's body that contained significant harmonics (Fig. 2.1). This stability permitted measuring the potential at different positions sequentially, and later combining the measurements into high resolution maps. I synchronized these measurements using a stationary electrode connected to an electronic comparator that triggered the analog-to-digital converter (ADC). It immediately became apparent that in the fish's near field, the EOD amplitude and phase was highly variable with position. Furthermore, some regions of the fish's body were dominated by harmonics, resulting in multiple peaks and complicated waveforms (see Chapter 3). I had stumbled upon a complex electric sensory world, rich in spatiotemporal structure, and virtually unexplored in these dimensions.

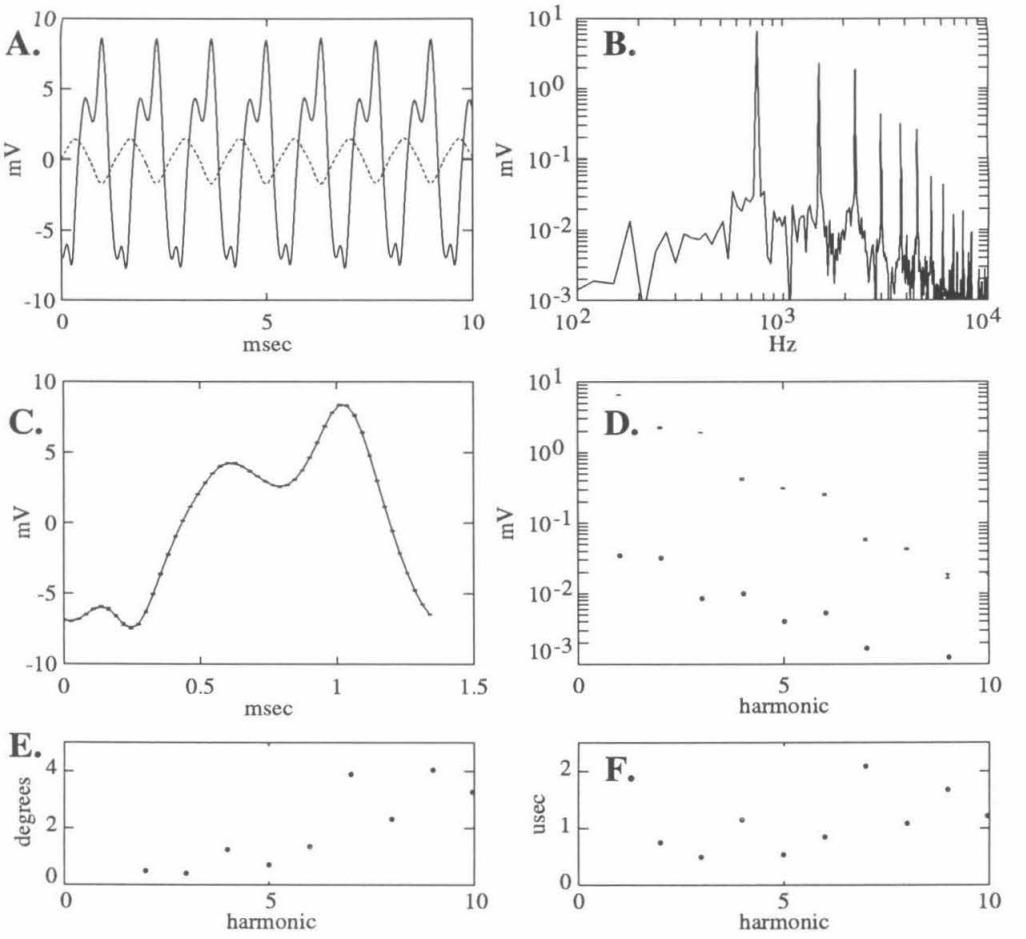

Figure 2.1. Stability of the EOD. A. EOD waveforms near a fish's tail (solid line) and head (dashed line). B. Amplitude spectra of the tail waveform in A. C. Mean and standard deviation (error bars) of the EOD waveform, sampled 20 times over a 40 minute period. (D.) Mean and standard deviation (error bars and lower points) of the amplitudes of the lowest 10 harmonics, for the same data. E, F. Standard deviation of the phase angles of the first 10 harmonics, expressed in degrees and microseconds.

2.2. Hardware

Architectural elements of most machines, man-made and natural, are often best understood after accounting for their history. The electric field mapping apparatus began with a Masscomp 5500 computer and data acquisition system connected to an electrophysiology amplifier. I mounted a mobile electrode on a broken pen plotter (constraining the electrode to a plane) and pushed the plotter by hand. I next obtained a working analog plotter and a GW Instruments MacAdios II multifunction I/O card for a Macintosh II computer. This board positioned the plotter arm with its two digital-to-analog converters (DACs), and sampled 8 channels sequentially at a cumulative data rate of 142 kHz. Experiments were controlled within Hypercard using external code modules. Chris Assad and I constructed eight channels of analog electronics using op-amps. Results from this machine are presented in Chapter 3. Subseqently, I designed a third machine, with quieter and more stable amplifiers and a much quieter and faster 16 bit data acquisition system. Control and data analysis were done in Matlab 3.5, with external code modules addressing the hardware. A block diagram of this apparatus is shown in Fig. 2.2.

2.2.1 Electrodes.

Some of the electrode arrays used in these experiments are shown in Fig. 2.3A. The electrode tips are approximately spherical 150-250 μm diameter silver balls, formed by melting a 75 μm diameter silver wire in a Bunsen burner flame. They are insulated either by being pushed through a 1 mm O.D. glass capillary tube that was tapered in a physiology electrode puller, or by a 20 μm thick teflon coating. The teflon coated electrodes were shaped into flexible arrays used for recording the potential on the fish's curved body. Rigid arrays permitted differential recordings between other electrodes in the array, from which the electric field components could be estimated. These electrodes

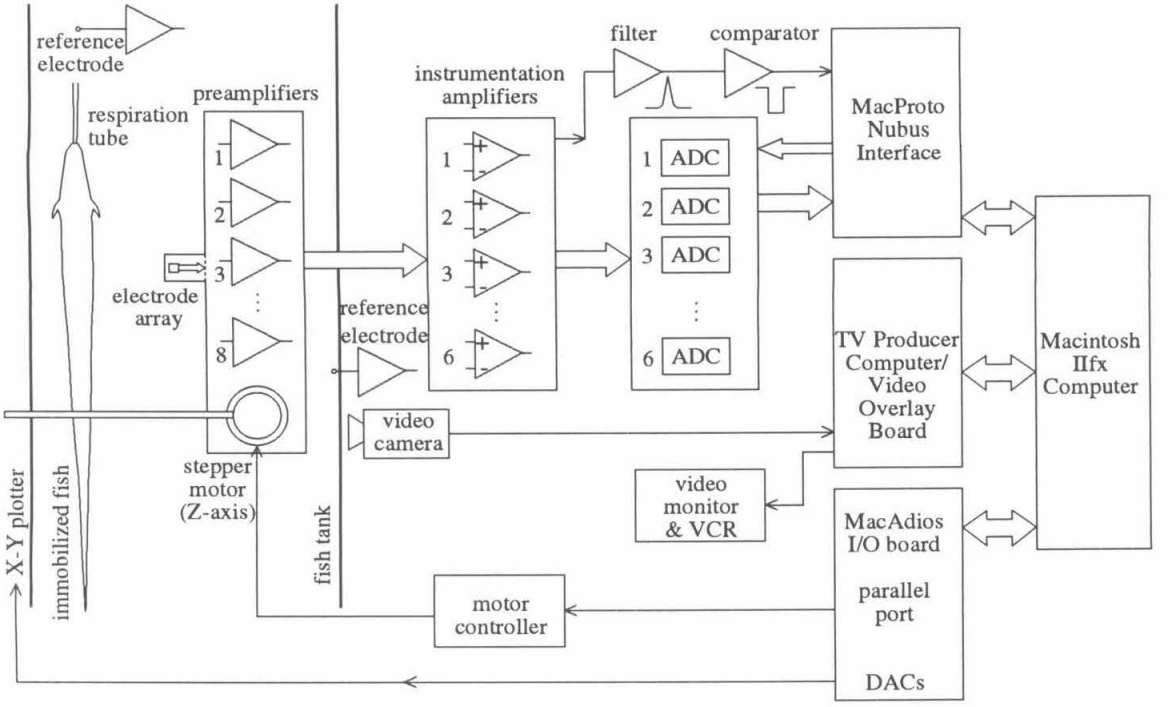

Figure 2.2. Block diagram of the electric field mapping apparatus. Potentials surrounding an immobilized fish were measured simultaneously with stationary reference electrodes and a mobile electrode array. A Macintosh IIfx computer with three Nubus boards controled the electrode positioning and sampled the amplified and digitized electric organ discharge of an immobilized fish.

had impedances of 10-20 kΩ in 2 kΩ-cm water, dominated by the spreading resistance of the water (see Appendix 1).

Additional stationary electrodes were used as references. An uninsulated #20 silver wire was folded over the lip of the glass respiration tube to record the EOD in the fish's mouth. On the side of the tank was a 1 mm diameter ball melted from #20 silver wire and insulated in a 1 mm O.D. pipette, tapered at the ball. These electrodes had

impedances of 3-5 kΩ. For some experiments, electrodes were placed inside the fish's gut. These were made from Grass #E2 platinum subdermal electrodes. These sharp and stiff wires were insulated by slowly pulling them through molten glass power on a Tungstun filament. The tank was grounded with a 0.25 x 4 inch carbon rod in a corner.

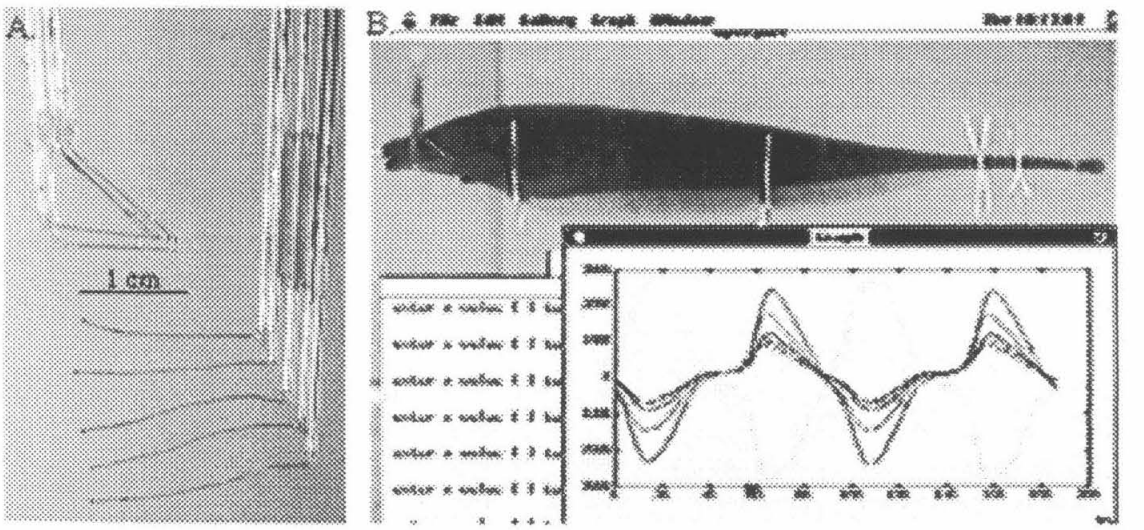

Figure 2.3. A. A rigid electrode array for measuring the electric field (left) and a flexible array for measuring potentials (right). B. A video frame from a mapping experiment. The field array is located near the fish's head. In the fish's mouth is a glass tube carrying a constant flow of water for respiration, and the fish is supported by insulated #22 wires. Waveforms from the array are also shown .

2.2.2 Electrode positioning.

The electrode array was mounted on a stepper-motor controlled microdrive that moved vertically over an 8 cm range. This structure, along with preamplifiers (see

below), was attached to a shaft extending from an H-P 7035B X-Y plotter, giving 13 by 16 inches of travel in the horizontal plane. The electrodes could thus be moved in three dimensions electronically and gently brought in contact with the fish's skin. The plotter was driven by a pair of digital-to-analog converters (DACs) on a GW Instruments MacAdios multifunction I/O board. Rather than relying on the DACs and the plotter's positioning accuracy, I used visual feedback of the electrode positions with a video camera (Sony TR-5) and a video overlay board (Computer Friends TV Producer). First, a real-time view of the fish and electrode array were put in the background of a window on the Macintosh computer. The fish's body was traced, and sequential electrode positions were marked by mouse on the computer screen (Fig. 2.3B). Resolution was one pixel, which generally corresponded to approximately 500 μm.

This method had the additional advantage of permitting flexible arrays for measurements on the fish's body, where the relative electrode positions changed with the curvature of the fish. The video coordinates were a 2-D projection of the fish, though the electrodes would sit on the 3-D body surface. Each experiment was recorded with a video cassette recorder (VCR).

2.2.3 Analog instrumentation.

Each electrode was connected to a high impedance follower mounted nearby on the stepper motor platform. The follower outputs were routed to instrumentation amplifiers (IA) with jumper-selectable gains of 10, 100, 200, or 500. Each follower output could be connected to any (and multiple) IA input. The IA outputs connected to the ADC boards (see below). System noise was approximately 30 nV/$\sqrt{\text{Hz}}$ or 3 μV RMS over 10 kHz bandwidth, slightly above the Johnson noise of the electrodes (see Appendix 1).

A phase reference signal was generated from the potential difference between two stationary electrodes (usually placed in the mouth and on the tank wall lateral of the

fish). This signal passed through a 60 Hz active twin-T notch filter and a 200 Hz bandpass filter tuned to the fish's fundamental frequency, to a comparator with variable DC bias, producing a digital pulse at the same phase of each EOD cycle. The potential before the bandpass filter was also recorded on an ADC channel.

2.2.4 Analog-to-digital conversion.

Since the EOD of electric fish have frequencies within the audio spectrum, only amplitude conversion is necessary to utilize inexpensive digital audio equipment, such as delta-sigma ADCs. These are very high speed (several MHz) 1-bit converters that have a relatively simple analog comparator followed by sophisticated digital filtering. Delta-sigma converters require simple (i.e., single pole) anti-aliasing filtering because their sample rate is many decades above the digital passband. The major drawbacks of delta-sigma converters are that their digital pipeline makes external triggering and input multiplexing impossible at high speeds. To solve the multiplexing problem, separate converters were used for each IA, and their tri-state digital outputs were multiplexed. For triggering, the phase reference channel synchronized data acquisition to within one period of the free-running converters, and phase adjustments to the digital data were made afterwards using software.

Another weakness of delta-sigma converters is gain error or passband ripple caused by the digital filter, which is as high as 6 bits for full-scale input in some common converters (e.g., the Crystal Semiconductor CS5336, used in the Sony DAT). I chose a delta-sigma ADC with maximum passband ripple of 2 LSB. This chip has larger dc offsets and temperature coefficient than typical for a research-grade ADC, but DC levels were subtracted with software, and the converters were housed in a closed box and allowed to reach thermal equilibrium before beginning experiments.

To avoid designing complex ground plane and shielding necessary to minimize digital noise contamination of the analog inputs, three Crystal Semiconductor CDB5326

stereo ADC prototyping boards were used. Each board has shielded anti-aliased inputs, power supply decoupling, clocks (48 kHz per channel sample rate), and serial and parallel output. Clock signals from one board were routed to the others, synchronizing all channels to within nanoseconds, and the tri-state 16-bit parallel outputs (left and right channels are multiplexed) were bussed. Additional signals were a left/right clock, data valid, and addresses for each card (output enables). The system is accurate to 14 bits without averaging, which conveniently accommodates the large dynamic range of the fish's signals (the 12 bit MacAdios ADC is only accurate to 9 bits without averaging).

2.2.5 Computer interface.

An Adex MacProto Nubus prototyping board interfaced the ADCs to a Macintosh II computer. This board provides separate 32 bit data and address busses (they are multiplexed on Nubus) and a simplified handshaking protocol. Although the Nubus runs at 10 MHz, it is asynchronous with the CPU. The MacProto board preceded the TI Nubus interface chipsets, and limits throughput to slightly over 1 MHz (4 Mbytes/sec). The cumulative sample rate over the 6 channels was 288 kHz.

Control signals from the ADCs and the phase comparator were combined in a status register. This register was polled to synchronize data acquisition with the EOD phase and left/right clock. Once synchronized, samples were read sequentially from the ADCs by handshaking between the Nubus interface and the ADCs, without polling.

2.3. Software

The software for these experiments was built on a two-level hierarchy. "Low level" routines control the hardware for electrode positioning and data acquisition. These are generally small programs written in C and 68000 assembly, and include any time-critical functions, such as synchronizing and reading time series from the ADCs. These routines were integrated within a flexible environment permitting rapid modifications of

experiment parameters and sequencing. Hypercard and Matlab were used for this "high level" environment. Matlab source code (`set in this font`) is included below because this language is sometimes very concise and clear in expressing mathematical algorithms. Additional details and examples are presented in the following sections.

2.3.1 Data acquisition and control.

The experiments were controlled by a Macintosh IIfx computer running System 6.0.5 and Multifinder. Time-critical operations such as data acquisition were executed by accessing the CPU directly, disabling all CPU interrupts, and polling the interface hardware, thus guaranteeing no data gaps. Three programs and drivers formed the backbone of the experiments. First, a window was created with uniform color fill using NCSA Image 1.29, a public domain image processing program. The video overlay driver of TV Producer made this color "transparent" to the live video of the fish tank coming from a Sony TR5 camera. Within Image, the fish body and any objects were outlined, and the sequential electrode positions during the mapping experiments were marked using video-opaque colors. The TV Producer output is NTSC video of the Macintosh screen with the Image window showing the fish tank (Fig. 2.3B). This was displayed on an NTSC monitor and recorded with a Sony 8mm VCR (EV-C3 or EVS-9000).

Matlab 3.5 (The Mathworks, Inc.) was responsible for the remaining experiment control and majority of the data processing. Matlab, which stands for *matrix laboratory*, is an interactive system whose basic element is a matrix that does not require explicit dimensioning. Matlab can be extended in three ways. First it supports scripts consisting of sequences of other Matlab functions and scripts. Second, it supports functions, which are essentially scripts with local variables. And as of version 3.5, functions can be compiled from C or other languages. Two compiled functions were required to communicate with the new hardware devices:

```
• setdacs(dac0, dac1)    set MacAdios DACs to position the array

• s = crystal(n,c,t)  read n ADC samples from c channels on
trigger t

• t = wait(n)         pause n seconds and return the current
time
```

The third function reads the Macintosh clock to facilitate real time operation.

The `crystal` function initially polls the phase reference signal so the first sample is always at approximately the same EOD phase. As described above, the ADCs ran continuously and asynchronously with the CPU and the fish's EOD. Therefore this triggering is temporally accurate only to the next sample, within 21 μsec. This jitter can be substantially reduced in software if the phase reference signal is sampled and saved, as described below.

2.3.2 Data analysis and visualization.

The waveform amplitudes were first corrected for different channel gains, and converted to spectral amplitudes and phases. This was done while the plotter was moving to the next sampling position and vibrations were damping. The result is a set of compressed vectors (complex spectral amplitudes) at various locations in the fish tank. The locations are not uniformly distributed, as the spatial frequency components of the potential vary with head-to-tail position and distance from the fish.

Mark Nelson and I had written software for finite element simulations of electric fish potentials [3], [4]. Since we wished to compare potential measurements with simulations, it made sense to treat the measurement points as finite element node points. Using the same interpolation scheme would eliminate a potential source of systematic error between the simulations and measurements. In the simulations, interpolation was done over the triangular finite elements using linear shape functions [5]. This is a biased interpolation scheme, but it is implied that the interpolation points or nodes are dense

enough that local changes are linear. To apply this to the measured data, we had to artificially group the measurement points into triangles, and sample at high enough density. A Delaunay-Veroni tessellation [6] was implemented in a program called p2elem. P2elem sometimes does not find the best set of triangles. In these cases, the element file can be edited graphically with a program called Vuelems, accessed by the "ve" command within Vu (see below and Appendix 2).

For visualization of the interpolated maps, I wrote a graphics application called Vu. Vu runs a command line interface and can read script files, that simplify the generation of complicated animation sequences and side-by-side comparisons. Vu must read several files to generate an image. First, it looks for a pair of binary files called *tag*.nodes and *tag*.elem, generated by p2elem, and containing lists of the node coordinates and triangles. The solution to be interpolated can be in either an ASCII or Matlab file, *tag*.matsol. Vu can also load polygon coordinates from ASCII files (this is how the fish's body is drawn), and it can write PICT and PICS graphics files. Vu is a complex program of approximately 5000 lines of C code. Appendix 2 contains the current command summary.

The following section is an example of how some of this code is used and integrated. Every time the electrode array is removed from its mounting, the interelectrode distances must be calibrated. This is done by mapping the electric field of a discrete dipole in the recording tank. The dipole maps differ from those of a fish in several ways. Most fundamentally, there is an analytic solution, so several equations can be inverted and solved for hardware-dependent calibration coefficients. Furthermore, the field geometry is much simpler due to symmetry, so the field can be mapped along a few straight lines. For speed, the DAC coordinates that drive the X-Y plotter are used without video feedback to measure the electrode positions. The function generator driving the dipole also causes a slight increase in 60 Hz noise and a high frequency line-locked spike. Both artifacts are removed with software.

2.4. Calibration with a Dipole

The goal of this experiment was to identify and correct systematic errors and verify the accuracy of the electric field mapping apparatus. The field generated by a dipole in a rectangular tank can be computed analytically, with corrections for the tank walls and water surfaces incorporated using the method of images [7]. The field is measured with an array of four electrodes approximately at the vertices of a 1.2 mm cube; a fixed reference electrode on the tank wall near the zero potential plane; and another fixed electrode as a phase reference. From potential measurements relative to the tank wall and their theoretical values, the most probable location of the poles is computed. The electrode distances are then optimized to best fit the measured potential differences with those computed from the electric field equations.

2.4.1 Gain calibration.

The gain of each channel was measured by placing the electrodes in a metal can connected to a Wavetek 20 function generator. A stiff voltage divider reduced the function generator potential on the can to compensate for the high gain while still permitting it to be measured accurately with a Fluke 87 multimeter (13 bit true RMS; the attenuators on the Wavetek are passive and only accurate for 600 Ω loads). Since the water inside the can is equipotential, all the electrodes measure the same voltage. The conversion factor between ADC units and mV should be approximately (3680 mV) / (2^{15} ADC) / (IA gain = 500) = 2.25 * 10^{-4}. A typical measured result for the six channels was:

```
vfluke = 2456 * 201 / (201 + 110.2e3); % mV across a V-divider
adc2mv = vfluke / mrms(crystal(800, 6, 1))
adc2mv =
    1.0e-03 *
    0.2407     0.2383     0.2287     0.2409     0.2371     0.2276
```

`mrms` *computes* the RMS average of the sampled waveforms after subtracting any DC offset. Eight hundred samples were averaged, which constitute 10.0 periods of the 600 Hz function generator waveform and exactly one period at 60 Hz. The relatively large deviations from the expected gain (up to 7 %) are primarily due to stationary errors in the 3.68 V voltage reference on the different ADC chips (channels 1 and 4, 2 and 5, 3 and 6, which are the "left and right channels" on the same chips, are closest to each other). Taken into account, these errors pose no problem to subsequent analysis.

2.4.2 Dipole construction.

A dipole was made from two 1/8 inch diameter stainless steel ball bearings soldered to insulated wire wrap wires held rigid on 1 mm O.D. glass tubes 4 cm apart. This structure was placed near the center of the 60 x 60 x 16 cm deep recording tank with axis parallel to the plotter X axis, and connected through a 200 Ω series resistor to the function generator. With amplitude approximately 300 mV at 600 Hz, the dipole moment is similar to *Apteronotus* [8].

2.4.3 Mapping.

The poles are located in DAC coordinates by positioning the array visually (for this, a more interactive Hypercard based plotter controller is quicker than Matlab). In dipole-centered coordinates with the poles at approximately (±2, 0, 0) cm, samples are taken along four lines: (x, 2, 0), (4, y, 0), (x, 0, 2), and (2, y, 2), where the x or y coordinate is varied from -8 to 8 cm in 1 cm or .25 cm steps. The following Matlab script executes this entire mapping:

```
poles = [1668 701; 2094 702];
origin = mean(poles);
dac2cm = 9.77e-3; cm2dac = 1/dac2cm;  % coordinate conversion
s = [-8:1:-5 -4:.25:4 5:8]';          % sample density (cm)
line1 = mmv([s zeros(s)+2] * cm2dac, -origin);
dip1 = map(line1, 'sampleftn');
line2 = mmv([zeros(s)-4 s] * cm2dac, -origin);
dip2 = map(line2,'sampleftn');
disp('move array up 2 cm');pause;
```

```
line3 = mmv([zeros(s)-2 s] * cm2dac, -origin);
dip3 = map(line3,'sampleftn');
line4 = mmv([s zeros(s)] * cm2dac, -origin);
dip4 = map(line4,'sampleftn');
save dipdata                          % save everything
```

Function `mmv(m,v)` subtracts vector `v` from each row of matrix `m`. In the above code, it converts the sample line from cm into DAC coordinates. Function `map(coords, sampleftn)` is mainly a bureaucrat that collects the data from each position. It repeatedly calls `sampleftn`, which reads the waveforms by calling `crystal`, moves the array to the next position, and processes the data as the plotter vibrations dampen. The sampling function for this experiment is simply:

```
function out = sampleftn(nextx, nexty, s)
% global Gcoefs
a = crystal(1600, 6, 1);
moveslow(nextx, nexty, 50);
plot(a([1501:1600 1:100],:));
xlabel(s);
out = ft(a,80, Gcoefs)';
wait(.2);
```

`moveslow` gently slews the plotter by calling `setdacs` repeatedly with small offsets. The the last 100 measurements are plotted followed by the first 100. Any amplitude difference between the first and last values, which can cause aliasing errors in a subsequent Fourier transform, will be apparent in the middle of the plot. Function `ft` computes the Fourier transform of the sampled waveform. Because the frequencies of interest are known (in this case only 600 Hz, with a period of 80 samples), the Fast Fourier Transform (FFT) is grossly inefficient, for it computes amplitudes of all frequencies. By computing coefficients in advance:

```
Gcoefs = exp(-sqrt(-1)*80 * 2 * pi * [0:1599] / 1600) / 1600 * 2;
global Gcoefs
```

the corresponding complex amplitude is computed by just a dot product:

```
f = Gcoefs * a;
```

This is what function `ft` does. The result is bandpass filtering, averaging over 20 periods, and data compression from 1600 samples to a single complex number per channel.

Mapping fish is less automated and more interactive. Positioning electrodes on the body is more difficult and must be carefully visually guided, and the electrode positions are recorded with the video overlay system. The fish's frequency is not always an integral multiple of 60 Hz, thus an integral number of EOD periods nearest to one or two periods of 60 Hz are sampled. This minimizes aliasing without windowing functions. With fish, the lowest 8-10 harmonics are computed and saved. The fish's frequency is constantly monitored with a Fluke 87 multimeter, and the coefficients and number of samples are adjusted accordingly. Depending on the fish and temperature stability, the EOD frequency is typically adjusted by one sample (out of 1600) every 10 min.

2.4.4 Phase alignment.

A phase reference signal from stationary electrodes is always sampled on one ADC channel (usually channel 6) to permit precise temporal alignment of successive measurements. The data along a measurement line consists of an m by 6 matrix (e.g., `dip1`), of complex amplitudes of the fundamental at each m points on the 6 parallel channels. In the case of a fish map, this would typically be an m by 48 matrix of complex amplitudes of the first 8 harmonics on each channel. The reference phase at the m positions is given by:

```
theta = angle(dip1(:,6)) + pi/2;          % 0 = + zero-crossing
plot(s, theta *180/pi);                   % see Fig. 2.4A
```

The other channels can be shifted by this amount:

```
shift = exp(sqrt(-1) * theta')';
sdip = mtv(dip1(:,1:4), -shift);
plot(s, abs(sdip) .* sign(angle(sdip)))  % see Fig. 2.4B
```

```
plot(s, angle(sdip) * 180 / pi)          % see Fig. 2.4C
```

The function, `mtv(m,v)`, multiplies the columns of matrix `m` by vector `v`, thereby shifting the phase of all channels by an amount equal to the negative of channel 6's phase. Had eight frequency amplitudes been measured at each point, each harmonic would have to be shifted by the same time, or by phases given by:

```
shift = exp(sqrt(-1) * theta' * [1:8])';
```

and this matrix multiplied by the eight amplitudes on each channel.

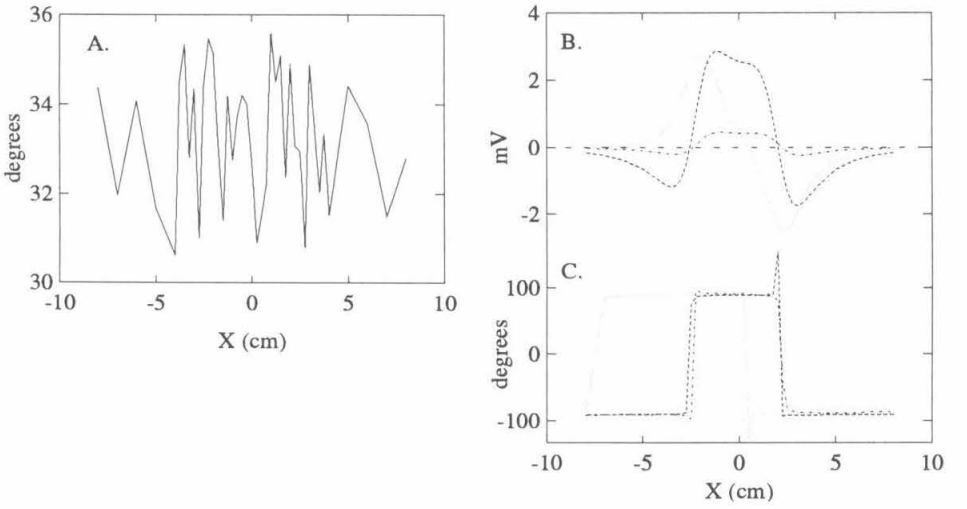

Figure 2.4. A. The phase of the reference channel varies randomly within approximately one ADC sample, or 21 μsec, corresponding to 4.5 degrees for the 600 Hz sinusoidal dipole signal. B, C. Amplitudes and phases of the differential signals recorded between electrodes in the array. The phase of dipole is ±90°. From a linear combination of these waveforms, the electric field components along the Cartesian axis will be determined.

2.4.5 Theoretical potential.

The wave number, k, of the electric field, in water of resistivity $\rho = 5$ kΩ-cm and dielectric constant $\varepsilon = 80\varepsilon_0$ is given by [7]:

$$k^2 = \mu\varepsilon\frac{\omega^2}{c^2}\left(1 + i\frac{4\pi}{\omega\varepsilon\rho}\right) \approx \mu\varepsilon\frac{\omega^2}{c^2}\left(1 + 10^5 i\right). \tag{2.1}$$

The conduction current greatly exceeds displacement current, thus the electrostatic current dominates and radiation is negligible. A current, I, injected at a point in an infinite tank will cause a radial current and field,

$$\mathbf{E} = \frac{\rho I}{4\pi r^2}\hat{\mathbf{r}}. \tag{2.2}$$

Thus by superposition, the field from a discrete dipole in an infinite tank, with poles at $\mathbf{x}_1$ and $\mathbf{x}_2$, is:

$$\mathbf{E}(\mathbf{x}) = \frac{\rho I}{4\pi}\left(\frac{\mathbf{x} - \mathbf{x}_1}{|\mathbf{x} - \mathbf{x}_1|^3} - \frac{\mathbf{x} - \mathbf{x}_2}{|\mathbf{x} - \mathbf{x}_2|^3}\right) \tag{2.3}$$

and the potential is:

$$\varphi(\mathbf{x}) = \frac{\rho I}{4\pi}\left(\frac{1}{|\mathbf{x} - \mathbf{x}_1|} - \frac{1}{|\mathbf{x} - \mathbf{x}_2|}\right). \tag{2.4}$$

The finite tank walls and water surface can be accounted for by placing image charges equidistant from these surfaces. The following Matlab function implements these equations, returning the electric field components and potential at locations `fieldpts` due to sources at `sourcepts`:

```
function [E, phi] = monopole(fieldpts, sourcepts, strengths)
phi = zeros(fieldpts(:,1));
E = zeros(fieldpts);
for j = 1:length(sourcepts(:,1)),
 rj = mmv(fieldpts, sourcepts(j,:));
 rjsquared = sum((rj.*rj)')';
 phi = phi + strengths(j) ./ sqrt(rjsquared); % 1 / |rj|
 E = E + strengths(j) * mtv(rj, rjsquared .^ (-1.5));
end;
```

The *image charges* can be appended to `sourcepts` and `strengths`. Their influence is small, thus only images for the vertical surfaces are used in computing potential. The computed and measured potential in the above experiment is shown in Fig. 2.5.

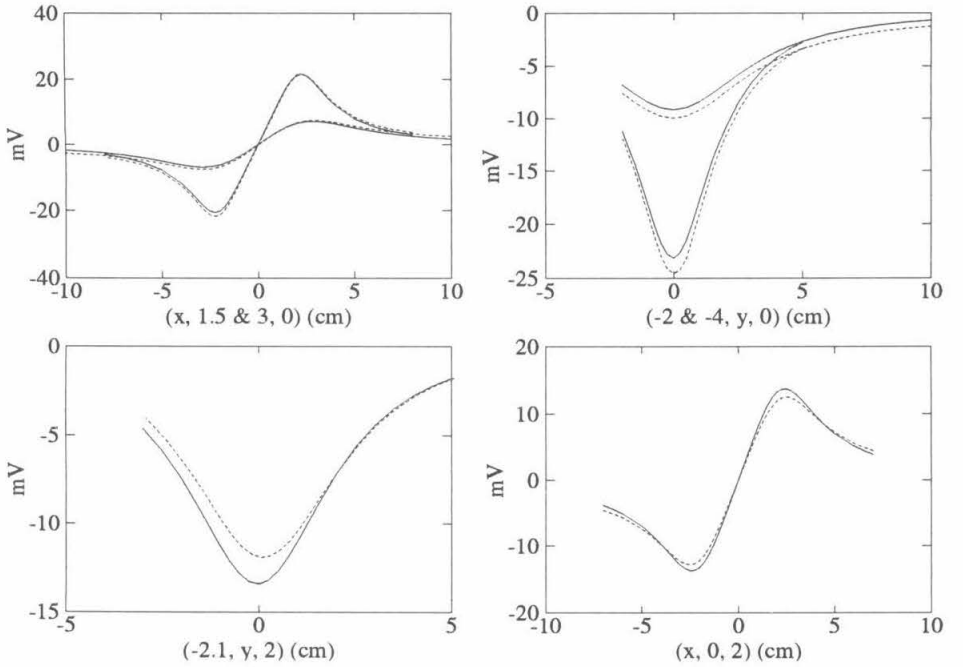

Figure 2.5. Potential relative to the tank wall of a dipole along 6 lines. Broken lines are measured and solid lines theoretical values, computed before any optimizations of parameters.

The dominant error can be eliminated by small corrections to the pole positions. Taking several points from each line in matrix `fieldPt`, with corresponding potentials, `vmeas`, the function `fmins` returns the matrix `bestpoles` that minimizes function `optimizep` below (`fmins` does a Nelder-Mead simplex optimization).

```
bestpoles = fmins('optimizep',poles,[],[],fieldPts,strength,vmeas);
bestpoles = reshape(bestpoles, 2, 3);

function err = optimizep(poles,fieldPts,strength,vmeas)
[e p] = monopole(fieldPts, reshape(poles,2,3), strength);
err = sum(abs(vmeas - p));
```

The results of this optimization are shown in Fig. 2.6, with (in cm):

```
bestpoles =
    -2.0851        0.1136       -0.1143
     2.2021        0.0257       -0.1433
```

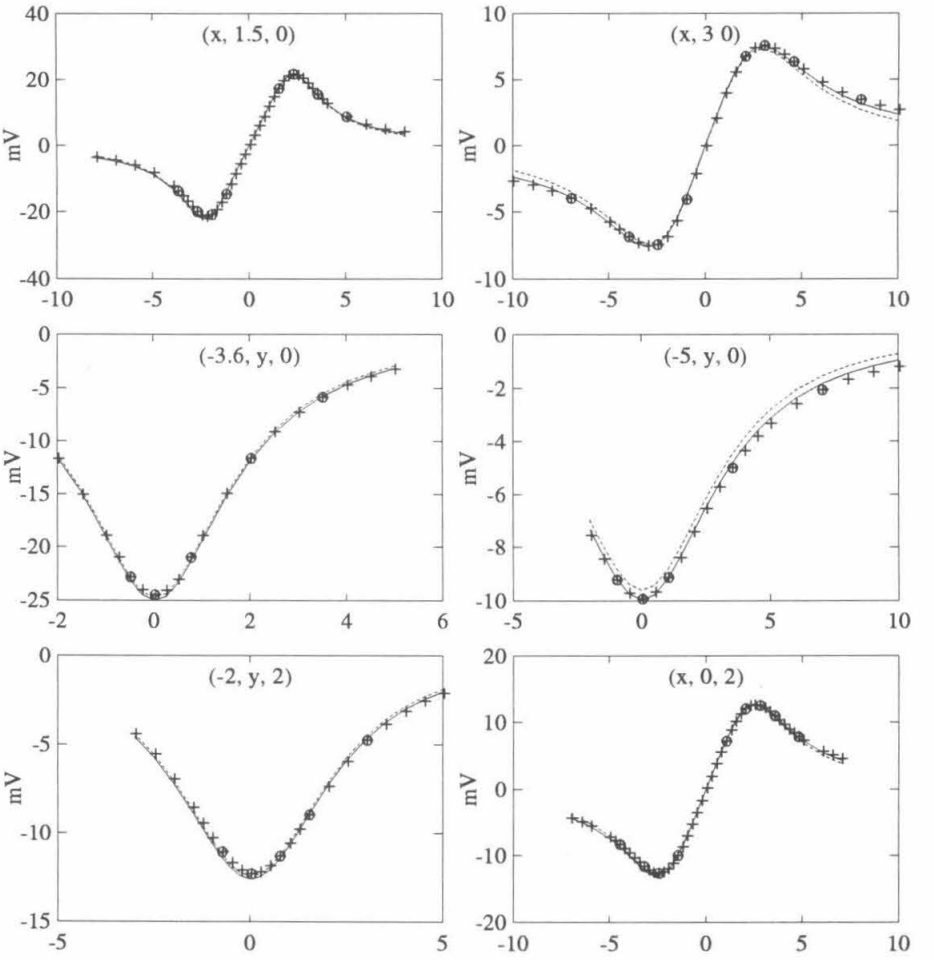

Figure 2.6. Measured and theoretical potential along the same six lines as Fig. 2.5. Measured values are denoted by '+', the values used in parameter optimization are denoted by 'o'. Lines are theoretical potentials using the optimized pole coordinates. The solid line includes image charges for the vertical water surfaces.

This is within the limits of visual accuracy (it is difficult to precisely locate the center of the dipole spheres in the plexiglass tank by pointing with an electrode array).

2.4.6 Electric field and electrode geometry.

If the array is in a uniform field $\mathbf{E} = (E_x, E_y, E_z)$, then the measured potential differences between electrodes are proportional to the field and the interelectrode distances:

$$\begin{bmatrix} \varphi_2 - \varphi_1 \\ \varphi_3 - \varphi_1 \\ \varphi_4 - \varphi_1 \end{bmatrix} = \begin{bmatrix} x_2 - x_1 & y_2 - y_1 & z_2 - z_1 \\ x_3 - x_1 & y_3 - y_1 & z_3 - z_1 \\ x_4 - x_1 & y_4 - y_1 & z_4 - z_1 \end{bmatrix} \begin{bmatrix} E_x \\ E_y \\ E_z \end{bmatrix} \tag{2.5}$$

where electrode k, at position (x_k, y_k, z_k) is at potential φ_k. The electric field components can be computed from the potential differences by inverting this equation. The inverse of the interelectrode distance matrix is estimated using a second optimization, this time minimizing the difference between the field components computed in this manner, and the theoretical field of a discrete dipole. Since the field decays faster than the potential, the vertical water surfaces had smaller effects, and were ignored. One of the arrays used in experiments presented here had interelectrode distances (in mm) of:

$$\begin{bmatrix} 2.203 \pm 0.014 & 0.264 \pm 0.003 & 0.177 \pm 0.022 \\ 0.452 \pm 0.006 & 1.315 \pm 0.000 & -0.038 \pm 0.002 \\ 0.290 \pm 0.015 & 0.053 \pm 0.068 & -1.231 \pm 0.034 \end{bmatrix} \tag{2.6}$$

where the uncertainty is the standard deviation from two calibrations (average standard deviation is 18 μm). The electric field components computed from the measured potential differences, and from theory based on measured water conductivity, current, and pole locations are shown in Fig. 2.7.

2.5. Calibration with a Fish

As a final consistency check of the array calibration, the differential field components computed using the interelectrode distance matrix are compared with the numerical

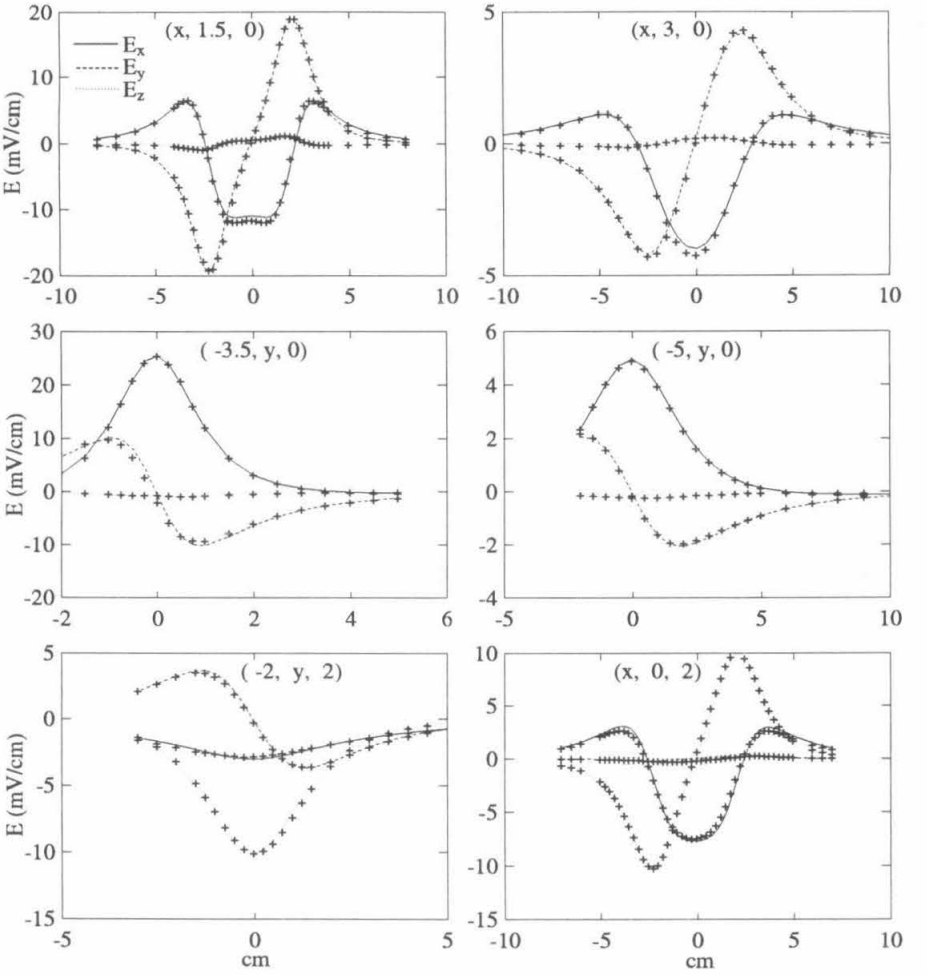

Figure 2.7. The three Cartesian electric field components, computed using differential potential measurements and the optimized interelectrode distance matrix ('+'), and computed by theory, based on water conductivity and dipole current (lines). Each figure shows the field along the a different line, denoted by inset. The poles are at approximately (±2, 0, 0) cm.

gradient of the potential measured relative to a distant reference (Fig. 2.8). Only the fundamental amplitude and phase are shown, but agreement between the two methods is similar for the other harmonics. The differential measurements are smoother, especially where the field is largest. The primary source of error is uncertainty in Δx. Measurements were taken at 1 mm steps within the nearest cm from the fish (Fig. 2.8A). However the plotter arm tends to stick under such small movements. Also, 1 mm corresponds to 10.5 DAC steps, so alternate measurements were slightly closer and further than 1 mm apart. Uncertainty in Δx, which is of order 100 μm, has significant effect on the numerical potential gradient, because Δx is of order 1 mm. In contrast, the

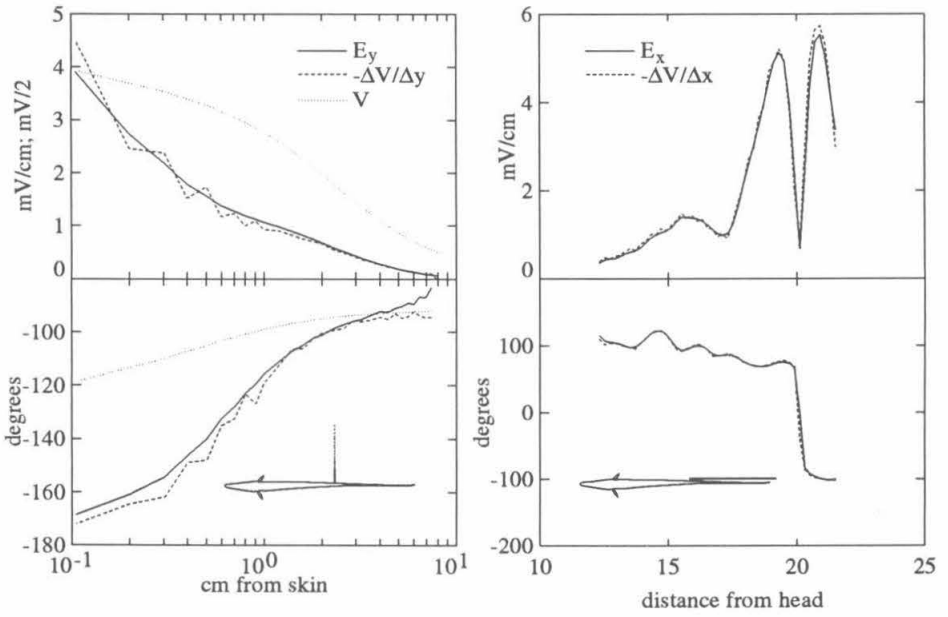

Figure 2.8. A. Amplitude and phase of the fundamental frequency electric field component, computed from the interelectrode distance matrix (solid line), and the numerical derivative of the potential (dashed line). The potential is also shown (dotted line). B. Same as A, along the tail, 6 mm from the fish's centerline.

differential measurements between electrodes in the rigid array have constant spacing, thus position errors just offset the point where the field is measured.

Beyond approximately one body length from the fish, the field magnitude has decreased substantially. Field amplitudes of 20 μV/cm, produce around 3 μV differential between the array electrodes. This is approaching the noise floor of the electronics. The harmonics, with lower amplitude, become dominated by noise, and the waveforms become unreliable. In this domain, the high spatial frequency components (or multipole moments) have already attenuated relative to the fish's dipole moment, and it becomes more accurate to compute the field from the gradient of potential measurements spaced 1-2 cm apart (or ideally, replace the array with a larger one).

The previous sections describe the design and calibration of an apparatus for mapping electric fish fields in three dimensions to within several percent absolute error. This accuracy was achieved by calibrating most electronic and geometrical parameters using analytic electric fields. The temporal stability and discrete spectra of wave-type electric fish (Fig. 2.1) were exploited to do efficient frequency domain filtering, alignment, and compression. A battery of software for data acquisition, analysis, and final display, has been assembled which has made mapping of electric fish fields to microsecond and millimeter resolution a relatively straightforward process. Potential and electric field maps of *Apteronotus* are presented in the subsequent chapters.

References

[1] Bennett, M.V.L., "Electric Organs," in *Fish Physiology*, Hoar, W.S., and H., R.D. (Eds.), pp. 347-491, Academic Press, 1971.

[2] Bullock, T.H., "The Reliability of Neurons," *J. Gen. Physiol.*, **55**:565-584, 1970.

[3] Rasnow, B., Assad, C., Nelson, M.E., and Bower, J.M., "Simulation and Measurement of the Electric Fields Generated by Weakly Electric Fish," in *Advances in Neural Information Processing Systems 1*, Touretzky, D.S. (Ed.), pp. 436-443, Morgan Kaufmann, 1989.

[4] Williams, R., Rasnow, B., and Assad, C., "Hypercube Simulations of Electric Fish Potentials," in *Proc. 5th Distributed Memorey Computing Conference,* Walker, D., 1990.

[5] Hughes, T.J.R., *The Finite Element Method. Linear Static and Dynamic Finite Element Analysis*, Prentice-Hall, 1987.

[6] Watson, D.F., "Computing the N-Dimensional Delaunay Tesselation with Application to Voroni Polytopes," *Computer J.*, **24**:167-172, 1981.

[7] Jackson, J.D., *Classical Electrodynamics*, Wiley & Sons, 1975.

[8] Knudsen, E., "Spatial Aspects of the Electric Fields Generated by Weakly Electric Fish," *J. Comp. Physiol.*, **99**:103-118, 1975.

Appendix 1. Electronics

A1.1. Electrodes

Metal electrodes in water do not always behave as ideal conductors due to chemical reactions occurring at their surface. Amplitude and phase distortions for a typical electrode used for recording electric fish potentials are shown in Fig. A.1.1. The impedance of the electrodes is dominated by their spreading resistance:

$$Z = \frac{\varphi}{I} = \frac{1}{I}\int \mathbf{E}\cdot\mathbf{dl} = \frac{1}{I}\int_{r_e}^{\infty} \frac{\rho I}{4\pi r^2} dr = \frac{\rho}{4\pi r_e} \approx 20\text{k}\Omega \qquad \text{(A1.1)}$$

with ρ = water resistivity = 2 kΩ-cm, and r_e = electrode radius ≈ 100 mm. The same value was measured by placing electrodes in the water-filled metal can connected in series with a resistor to a function generator.

The electrodes have a Johnson voltage noise density:

$$e_n = \sqrt{4\text{kTR}} \approx 18\text{nV} / \sqrt{\text{Hz}} \qquad \text{(A1.2)}$$

where k is Boltzman's constant, T is room temperature, and R is the electrode resistance of approximately 20 kΩ.

In a uniform electric field, each electrode of radius r_e causes a perturbation at distance r proportional to $(r_e/r)^3$. Since we want to measure the near field at a resolution of millimeters, it is not practical to make the electrodes within the array substantially larger without each electrode perturbing the potential of the others. Lowering the resistivity of the water would lower the electrode impedance, but this would create an unnatural environment for the fish (some electric fish live in extremely high resistivity water, approaching 100 kΩ-cm in the wet season).

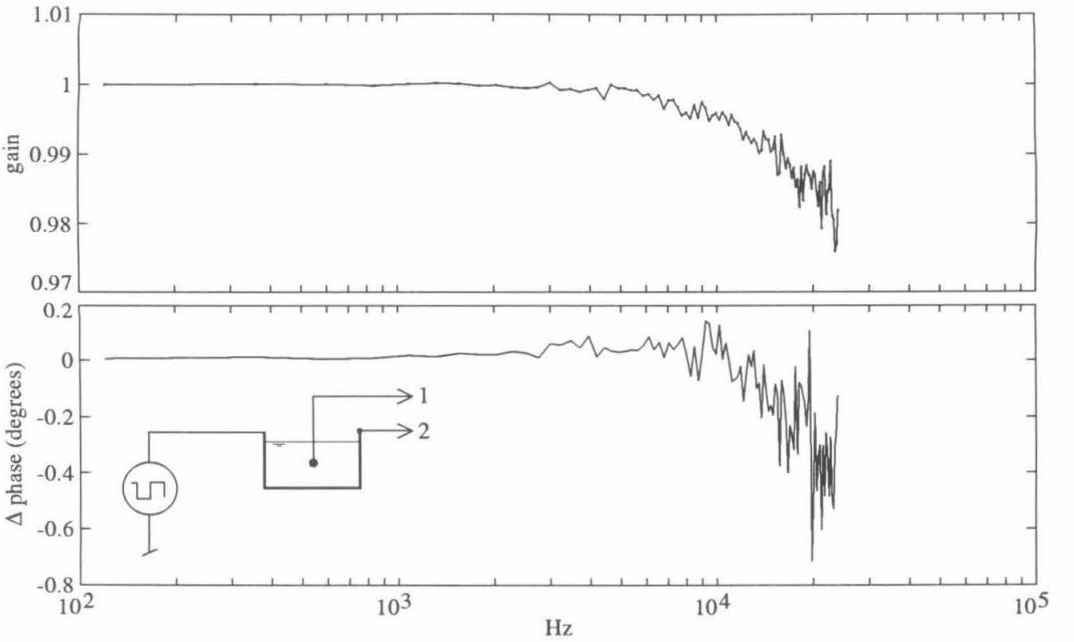

Figure A1.1. Bode plot of a typical electrode used to measure electric fish potentials. The electrode was placed in 2 kΩ-cm water within a metal can, which was connected to a 120 Hz square wave generator (inset). Electrode and function generator signals were simultaneously recorded on separate channels and Fourier analyzed. After normalizing the fundamental amplitudes, gain was computed as the amplitude ratio for the odd harmonics.

A1.2. Preamps

The preamps, LF356 op-amps wired as followers, have rated voltage noise density of 12 nV/√Hz and current noise of 0.01 pA/√Hz. The current noise through the electrode resistance makes a negligible contribution to overall noise. Thus coming out of the preamp, the noise should be:

$$e_n = \sqrt{18^2 + 12^2} \approx 20\text{nV} / \sqrt{\text{Hz}}. \qquad \text{(A1.3)}$$

Input impedance was measured with a pair of 100 MΩ resistors dividing a function generator voltage on the input. The LF356 has 2 GΩ input resistance at 100 Hz, dropping to 30 MΩ at 1 kHz, and above 1 kHz the impedance magnitude behaves as a 6 pF capacitor.

System bandwidth was limited by single pole low-pass and high-pass filters, with -3dB points at 1 Hz and 60 kHz (Fig. A1.2). The transfer function was measured by injecting a 120 Hz and 1 kHz square wave into the preamplifiers, and sampling the input and output. Amplitudes and phases of the harmonics were computed with the Fourier transform in Matlab. It is straightforward in Matlab to compensate for the resultant gain errors and phase shifts.

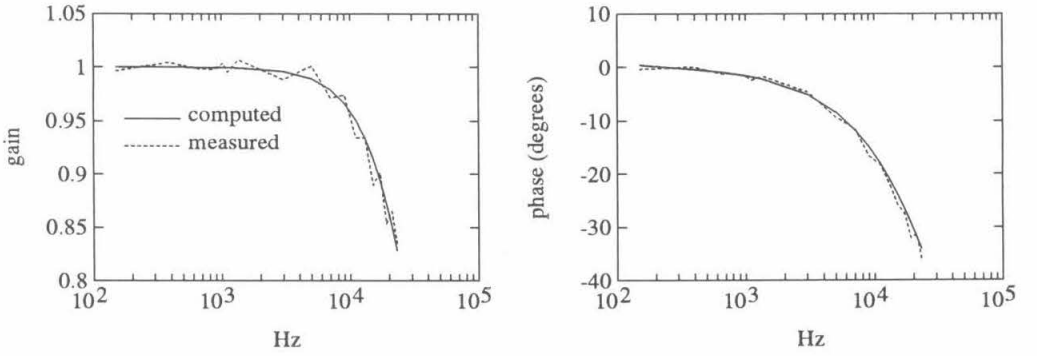

Figure A1.2. Bode plot of the electronics transfer function. The transfer function was computed based on component values (solid line) and measured by analyzing the harmonics of a square wave (dashed line).

A1.3. Instrumentation Amps

The instrumentation amplifier, Burr Brown INA110, has rated input voltage and current noise densities of 10 nV/√Hz and 1.8 fA/√Hz. The input impedance was shunted with a 1 MΩ resistor, thus the output noise density should be:

$$e_n = \sqrt{2(20\text{nV})^2 + (10\text{nV})^2 + (1.8\text{fA} * 10^6\,\Omega)^2} = 30\ \text{nV}/\sqrt{\text{Hz}}. \qquad \text{(A1.4)}$$

At a minimum gain of 10, this becomes 300 nV/√Hz on the output, which dominates the IA output noise density of 65 nV/√Hz.

With gain of 500, the output noise density is expected at 15 μV/√Hz or 1.5 mV over a 10 kHz bandwidth. The δ-Σ ADC, which has a sharp roll-off at 24 kHz, measured 2.7 mVRMS, close to the predicted value of 2.3 mVRMS (noise was computed with the Matlab fuction, `mrms`). Shorting the preamp inputs, which eliminates the electrode noise components, reduces the measured noise density to 11 μV/√Hz, and shorting the IA inputs reduces noise to 5 μV/√Hz at a gain of 500, consistent with the rated IA voltage noise density of 10 nV/√Hz. Fig. A1.3 shows spectra under these three conditions.

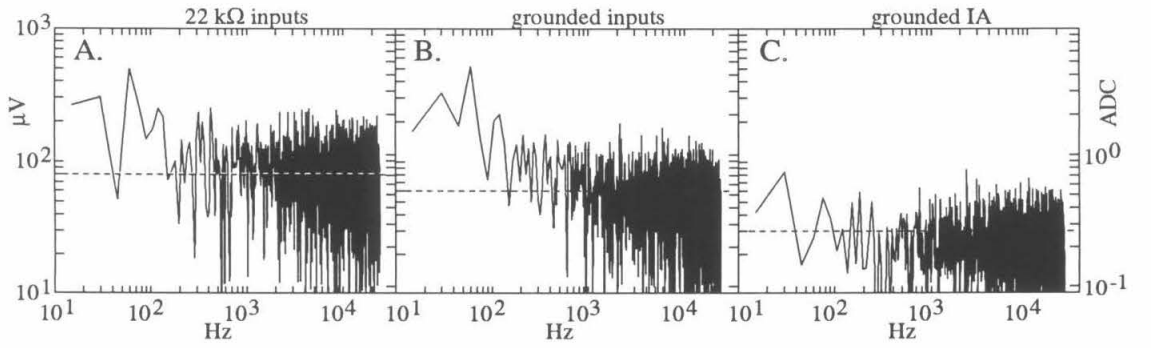

Figure A1.3. Noise spectra with a pair of 22 kΩ electrodes (A), grounded preamp inputs (B), and grounded instrumentation amp inputs (C). Each frequency bin has 30 Hz of bandwidth, thus the anticipated noise levels would be 80, 60, and 30 μV per bin for A, B, and C respectively (dashed lines). The axis on the right side is in ADC units.

A1.4. ADC

Two of a number of tests on the ADC's are shown in Fig. A1.4. With the ADC inputs grounded (at the IA outputs), the ADC output spreads over 4 adjacent values, or 2 bits (Fig. A1.4A). By grounding near the ADC, this is reduced to 2-3 values. To test linearity, a slow triangle wave was applied to the ADC (Fig. A1.4B). Assuming the function generator is producing a linear ramp, the difference between adjacent samples

should be constant (except at the peaks). Figure A1.4C and D show that the difference varies over three bits, with the vast majority of samples falling within 1-2 bits.

The ADC inputs (rated at ±3.8 V) were protected from overvoltage (the IA can swing to nearly ±15 V) with op-amp followers powered from ±5 V supplies. The LF 411, a low power op-amp, had the lowest harmonic distortion of several op-amps when operating near these low supply rails. Other approaches, such as Shottkey diodes, would require keeping the lines to the ADC's at higher impedance, reducing noise immunity. Clamping diodes in a feedback loop contribute larger errors from nonlinearities.

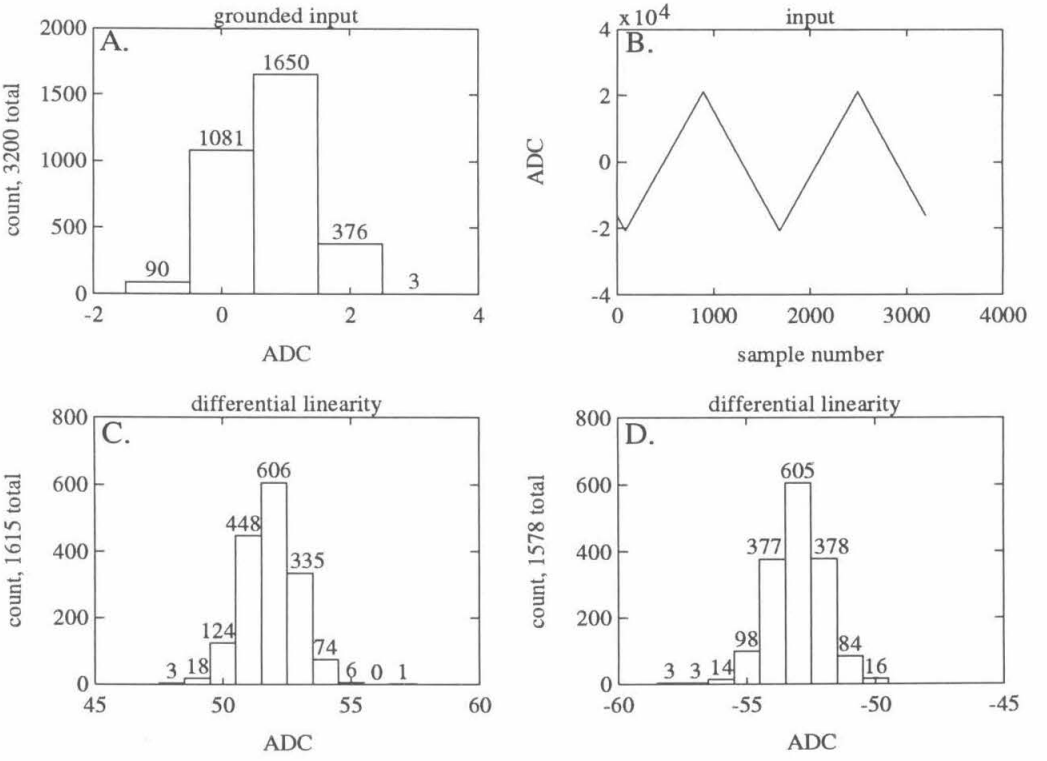

Figure A1.4. A. With inputs grounded, the ADC outputs are clustered within 4 counts. B. Differential linearity was measured with a slow triangle wave. The difference between successive samples on the positive (C) and negative (D) slope ramps was constant to within 8 counts.

Appendix 2
Vu Command Summary

Vu is Macintosh application that interpolates and displays in pseudocolor or grayscale data which was sampled at irregularly spaced positions. Although written for visualizing potential and field maps of electric fish, it can render other data sets. For example, it is being used to study salinity fluctuations in Florida Bay.

Command	Arguments	Description
a	<fname>	animate fname.PICS
A	<fname>	AverageInField(fname.field);
b		
	s	draw solid body
	r	draw rectangle
	w	draw waveform
	d	draw dots from file, no postfix sscanf(cmd + 1,"%s %d %d",file, &bodyColor, &dotsize) DrawDots(filename, &Viewer, dotsize);
	default	draw body outline*/ sscanf(cmd + 1,"%s %d",file, &bodyColor)
c		
	g	Viewer.ColorMode = BW;
	c	Viewer.ColorMode = COLOR;
	w	Viewer.wrapmode = LINEARWRAP;
	l	Viewer.wrapmode = HARDCLIP;
	t	Viewer.wrapmode = TANHWRAP;
	i	make bg black
	n	make bg white
d		
	v	DrawVectors(&ds);
	default	DrawField()
e		DrawElements(&ds);
f		ContourFromMemory(&ds, step);
F		toggle(macLineWidth)
g		DrawFieldFromMemory(ds.field, &Viewer);
j		DrawScale(&Viewer,whiteflag);
k		DrawHScale(&Viewer,whiteflag);
J		DrawScale(&Viewer,whiteflag);
N		system("clear");
P		system("gpdump");
l		set viewer p
n		EraseRect(&gwindow->portRect);
o		OutlineFishSkin(&Viewer,"skin1","skin2",cmd);
p		Probe(ds.field, &Viewer);

Command	**Arguments**	**Description**
T		saveWindow(gwindow, WIN_RESTORE, NULL);
q		done = 1;
r		LoadField(filename, ds.field, &Viewer);
R		set pictRect
s		set sensor size
t		WriteViewer(&Viewer,stdout);
u		ReadMatrixSolution(&ds);
U		read a new .nodes and .elem file
C		put current @ onto clipboard
	r	pictRect -> clipboard
	default	saveWindow(gwindow, WIN_TO_CLIP, &Viewer);
v		
	e	vuelems(&ds);
	default	set viewer
W		put it on the clipboard only
w		
	8	Save8BitField(filename, cmd + 1, ds.field, &Viewer);
	p	SavePICTField(filename, ds.field, &Viewer);
	P	SavePICTWindow(filename);
	a	SaveAsciiField(filename, ds.field, &Viewer);
	r	SavePICTRes(filename, &ds);
	default	SaveField(filename, ds.field, &Viewer);
y		DrawObject(filename, &Viewer, ds.field);
z		sscanf(cmd + 1, "%f", &(Viewer.poz));
-		SubtractField(filename, ds.field, &Viewer, scale);
@		n = sscanf(cmd + 1, "%d %d %d %d", &x1, &y1, &xnum, &ynum);
<		Executing script file %s\n", filename);
>		puts("Click mouse where text should be.");
#		printf("%s", cmd+1);
?		VU Command Summary
default		printf("%c??? type ? for help\n",cmd[0]);

VUELEMS Command Summary

Vuelems, accessed with vu with the "ve" command, facilitates analysis and modification of the element file used by vu to interpolate.

Command Arguments	Description
a	convert ascii nodes file to binary
c	convert ascii element file to binary
d n1 n2 ...	delete element n1 n2 ... if no arguments, deletes element at mouseClick
ef n	find elements containing node n
f	flip 2 elements
n/e n1	print node/element n1
n/e n1, n2	print nodes/elements n1 thru n2
n/e> fname	create ascii node/element file fname
n/e< fname	read ascii node/element file fname
n/ew tag	write binary node/element file tag.nodes/elem
n/ef x y	find node nearest (x,y) or element containing (x,y)
< filename	use text file for command input
p	Probe for nearest node & element
q	quit
r	reraw the elements
s	print Statistics on element & node files
#	comment
?	prints this help page

Chapter 3

The Electric Potential of *Apteronotus leptorhynchus*[1]

Summary

The electric organ discharge (EOD) potential was mapped on the skin and midplane of several *Apteronotus leptorhynchus*. The frequency components of the EOD on the surface of the fish have extremely stable amplitude and phase. However the waveform varies considerably with different positions on the body surface. Peaks and zero crossings of the potential propagate along the fish's body, and there is no point where the potential is always zero. The EOD differs significantly from a sinusoid over at least one third of the body and tail. A qualitative comparison between fish showed that each individual had a unique spatiotemporal pattern of the EOD potential on its body.

The potential waveforms have been assembled into high temporal and spatial resolution maps which show the dynamics of the EOD. Animation sequences and Macintosh software are available by anonymous ftp (mordor.bbb.caltech.edu; cd /pub/ElectricFish).

We interpret the EOD maps in terms of ramifications on electric organ control and electroreception. The electrocytes comprising the electric organ do not all fire in unison, indicating that the command pathway is not synchronized overall. The maps suggest that electroreceptors in different regions fulfill different computational roles in electroreception. Receptor mechanisms may exist to make use of the phase information or harmonic content

---

[1]Published as: Rasnow, B., Assad, C., and Bower, J., "Phase and Amplitude Maps of the Electric Organ Discharge of the Weakly Electric Fish, *Apteronotus leptorhynchus*", J. Comp. Physiol. **172**:481-491 (1993).

of the EOD, so that both spatial and temporal patterns could contribute information useful for electrolocation and communication.

3.1. Introduction

Two orders of freshwater fish possess a specialized electrosensory system that allows them to detect nearby objects in their environment [1], [2], [3]. These animals, referred to as weakly electric fish, generate high frequency electric fields (< 100 mV/cm, 0.1-10 kHz) which they sense with a few thousand electroreceptor organs distributed across their body surface. Some species emit short pulses with broad spectra, and other species generate a continuous wave-like discharge. The fish's electric organ (EO) which generates the field consists of hundreds or thousands of specialized current-generating cells stacked in series and parallel. The firing of these electrocytes is synchronized so that their currents add to produce a macroscopic electric field, referred to as the electric organ discharge (EOD). The electroreceptors are sensitive to local transepidermal potential and current. Electrolocation, the sensing of the environment via this electric field, is possible because objects such as other fish, food, and plants differ in their conductivity and dielectric properties from the surrounding water, and therefore can be detected as perturbations in the sensed field.

In this paper we describe the three-dimensional structure of the EOD potential generated by the South American gymnotiform fish *Apteronotus leptorhynchus* (brown ghost). The results reveal that the EOD creates a complex temporal and spatial potential surrounding the fish. The particular structure of this potential suggests several hypotheses concerning the neural control and regulation of the electric organ (EO), and provides information concerning the neural processing and behavioral relevance of the EOD. Whereas previous studies (e.g., [4], [5], [6]) have measured elements of the EOD in the midplane of electric fish (such as the RMS amplitude), we have focused on the

complicated waveforms on the fish's skin, and have combined these waveforms into maps that show the EOD dynamics.

3.2. Materials and Methods

Subjects.

These experiments were conducted on six *A. leptorhynchus* 18 to 30 cm long. We identified two of these as males, based on the shape of their heads [7]. Before recording, each fish was paralyzed with 30 to 50 μg Flaxedil (gallamine triethiodide) given intramuscularly. Since the electric organ of Apteronotids is neurogenic, this paralysis has no effect on the EOD [8]. Once paralyzed, the fish could be oriented for mapping in any desired body configuration.

Recording arrangements.

Each fish was placed in the center of a 60x60x18 cm tank upon three 'Y' shaped supports made from 3 millimeter diameter Plexiglass posts and #24 insulated wire that held the fish firmly above the post. A glass tube connected to a water recirculation system was placed in the fish's mouth to respire the fish while paralyzed. All structures near the fish were kept small to minimize field distortions. Though the tank was not large enough to eliminate edge effects, we observed little effect on potentials when moving the fish closer and farther from the walls. Water was maintained at 23° C, pH 6.8, and resistivity of 2 kΩ-cm.

Electrode construction.

The electrodes used in these experiments were kept relatively small to minimize their perturbations of the fish's electric field. Two different construction techniques were used depending on whether recording was on or away from the fish's skin. For recordings directly on the skin surface, we constructed flexible electrodes from insulated

25 μm diameter silver wire, the tip of which we melted into a 150-250 μm diameter ball. These wires were held in glass pipettes for rigidity, with the electrode tip extended approximately 2 cm from the pipette after a 90 degree bend.

For recordings away from the fish's skin, we constructed rigid electrodes by pulling 1 mm O.D. glass pipettes to slender and slowly tapering tips. Each electrode tip was broken at 25 μm I.D. A silver wire was pushed through the pipette and its end was melted to a 150-250 μm sphere that was then pulled flush with the glass. These pipettes were glued together far from the electrode tips so the support structure would minimally alter the electric field at the recording sites (Fig. 1B). The electrodes had impedances of approximately 15 kΩ, dominated by spreading resistance of the water [9]: $R_S = \rho/4\pi r_e$, where ρ = water resistivity = 2 kΩ-cm, and r_e = electrode radius ≈ 100 μm).

Electrode positioning.

The electrodes were mounted on a stepper-motor controlled microdrive that moved vertically over an 8 cm range. This structure was attached to a shaft extending from an H-P 7035B X-Y plotter, giving 16 inches x 13 inches of travel in the X-Y plane. The electrodes could thus be moved in three dimensions electronically (Fig. 1A) and gently brought in contact with the fish's skin. The exact recording location of the electrodes for each sampling position was determined optically using a video camera (Sony TR-5) and a video overlay board (Computer Friends TV Producer). First, a real-time view of the fish and electrode array were put in the background of a window on a Macintosh II computer. The fish's body was then visually traced, and sequential electrode positions were marked on the computer screen. Resolution was one pixel, which corresponded to less than 500 μm.

Electrical instrumentation.

Each electrode was connected to a high impedance (100 MΩ) follower amplifier mounted nearby on the stepper motor platform. The follower outputs were differentially

amplified with respect to a fixed electrode located on the tank wall at the zero-potential plane of the fish (as in [6]). The system bandwidth was extremely wide, 10 Hz to 50 kHz (-3 dB), to maintain constant gain and phase responses to the EOD fundamental and all

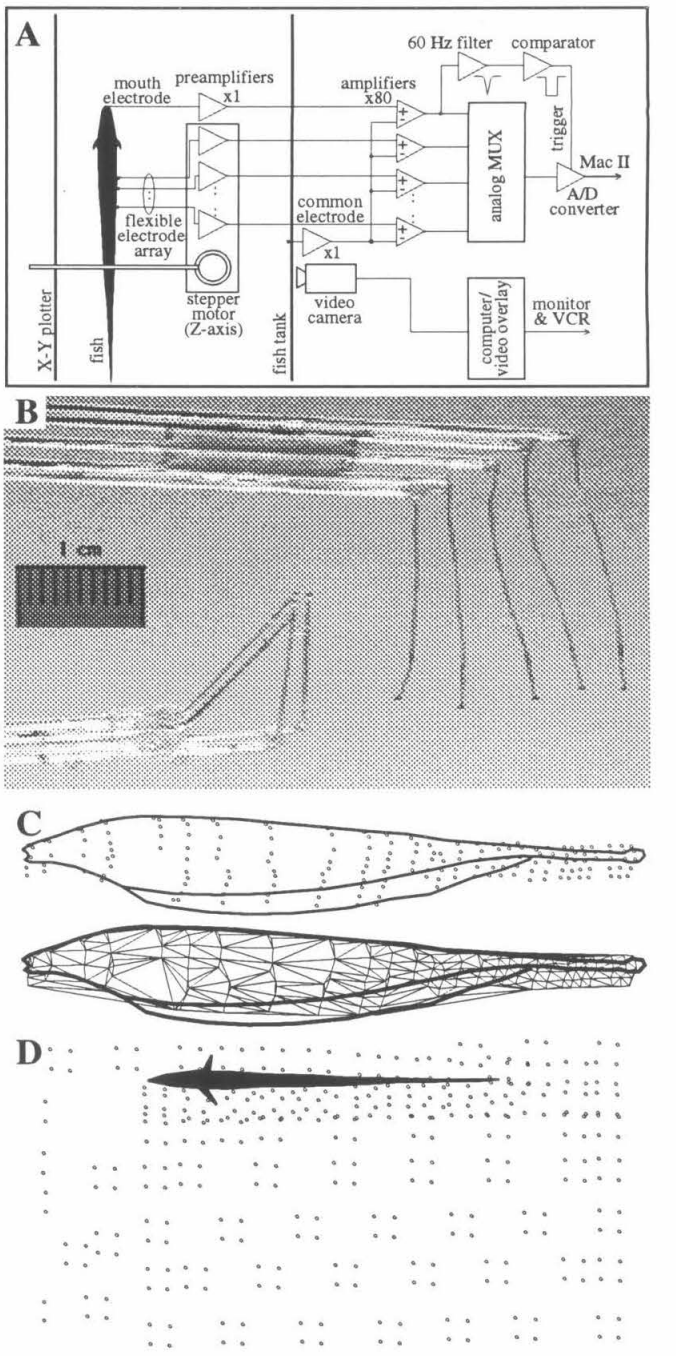

Figure 1. A. Diagram of the apparatus used to map electric potentials. B. Flexible (top) and rigid (bottom) electrode arrays used for mapping the EOD. Holes within the glue and gaps between the glass tubes reduce the field distortions from the support structures. C. Side view projection of a fish's surface with typical sampling positions from a five electrode flexible array. Interpolation elements corresponding to the sample points for creating the grayscale potential maps. D. Sample positions for a midplane map using a 4 electrode square array.

harmonics with measurable amplitude.

Since an experimental objective was to measure the EOD waveform rather than a time average, such as peak-to-peak or RMS amplitude, it was necessary to generate a phase reference signal to align waveforms recorded at different times and locations. This was accomplished using a second fixed electrode located in the respiration tube in the fish's mouth. The potential from this electrode was amplified and heavily filtered to generate a periodic digital pulse at the same phase of each EOD cycle (measured jitter was approximately 6 μsec). This pulse triggered the analog-to-digital conversions of the EOD waveforms. Three to five successive periods were recorded on each channel at 50,000 samples/sec with 16 bit resolution. Noise was approximately 5 μV RMS over a 15 kHz bandwidth, on the order of the Johnson noise of the electrodes [10].

Stability measurements.

The mapping procedure depends upon EOD constancy at each position from one cycle to the next. This criterion was tested by holding an electrode array stationary and sampling 5 to 15 EOD periods from each electrode every few minutes over the time course of an hour. Each record was sampled with a 125 kHz 12 bit ADC triggered at the same phase of the EOD. In all experiments, the reference channel was simultaneously sampled with every measurement to ensure stability. Average EOD frequency (over a 400 msec gating period) was also constantly monitored with a Fluke 87 multimeter (±0.2 Hz accuracy) and a loudspeaker.

Calibration.

Gains were measured and normalized for all channels by placing the electrode array in a metal can connected to a function generator. The potential was constant within the can. We performed many other system calibrations, including mapping dipole fields from a function generator connected to a pair of stainless steel ball bearings, with dipole moment similar to *Apteronotus*. The geometry permits an exact analytical solution (in the

form of a rapidly converging series based on the method of images). The analytic and measured potentials nowhere differed by more than 5%. The majority of the difference was systematic, attributable to an uncertainty in the relative position of the electrodes and the dipole of < 500 μm. The random error was an order of magnitude smaller.

Sampling procedure.

The spatiotemporal EOD pattern was measured by moving the electrode array to a series of recording positions and sampling the waveforms from each electrode. For mapping the potential on the fish's body, the array was moved towards the fish until all electrodes were touching the skin. The position of each electrode was then recorded using the video overlay system while the waveforms were recorded. Measurements were taken at variable spatial densities (as in Fig. 1C) because the EOD waveform changes substantially over millimeter distances near the tail and is similar over centimeter distances on parts of the trunk.

The video camera was located above the fish tank for the potential measurements in horizontal planes. The sampling density varied inversely with distance from the fish (Fig. 1D). A typical map of potential on the fish's side, consisting of approximately 40 positions of a flexible 5 electrode array, or 90 points in a plane with a rigid array, required 30 minutes.

Data analysis.

The raw data from these experiments consisted of digitized time series containing several periods of the EOD waveform at many positions, and with each time series beginning at the same phase of the EOD recorded in the mouth. These records were trimmed to an integral number of periods of the EOD fundamental and FFT-bandpass filtered with cutoff frequencies of 180 Hz and 5 to 20 kHz (depending on the spectra of the signal). The digital filtering further reduced noise without phase distortions inherent in analog filters.

Though single electrode recordings reveal the temporal structure of the EOD, the overall spatiotemporal structure is more difficult to discern. To visualize the potential on the fish's surface and midplane as it changes in time, we have represented the potential in grayscale at several consecutive phases of the EOD. For consistency, all waveforms and sequences in this paper begin in phase with the negative-to-positive zero crossing of the EOD recorded in the fish's mouth.

Because the EOD measurements were not at regular spatial intervals, smooth maps were constructed by interpolation. We used a Delaunay triangulation which groups triplets of adjacent points to form a set of triangles that completely cover the measured domain (Fig. 1C) [11], [12]. Within each triangle, the potential is interpolated to lie on the plane defined by the potentials at the vertices. In this manner, the five-dimensional data is visualized by rendering surfaces (typically the fish's skin or the midplane) with potential represented in gray levels at each particular time or phase of the EOD. A nonlinear grayscale was used (intensity proportional to the hyperbolic tangent of potential) because of the large dynamic range of potential around the fish. We have also animated the image sequences presented here in pseudocolor, and made available the data and programs for a color Macintosh on the Internet computer network by anonymous ftp (mordor@bbb.caltech.edu or 131.215.135.69; cd /pub/ElectricFish).

3.3. Results

EOD potential.

In this study, six A. leptorhynchus were mapped a total of nine times. Their fundamental frequencies varied from 549 Hz to 813 Hz, with males having the highest frequencies. The peak-to-peak potential was 3-5 mV on the anterior body surface, measured relative to the lateral tank wall (near electrical infinity). The potential was slightly larger at the operculum and remained relatively uniform over much of the trunk,

then rose to a peak-to-peak value of 30-50 mV near the tip of the tail. The trunk potential also decreased slightly with dorsal and ventral distance from the midline. In the water around the fish, the potential fell steeply with distance from the body. The higher order multipole moments seen in the caudal half of the fish decay most steeply with distance leaving a dipolar far field oscillating at the fundamental frequency of the EOD (see Discussion). The dominant asymmetry from a dipole extends on the order of the size of each pole, of order 1 cm on the tail and 10 cm on the trunk.

Temporal stability of the EOD waveform.

Figure 2 shows the stability of the EOD waveform at two different locations on a fish's skin. The coefficient of variation (CV = standard deviation/mean) of the peak amplitude was 0.01 in each case, while the CV of the frequency was 0.001 over the 50 minute sample period. Over shorter time scales (16 msec, or 11 periods), the amplitude CV was 0.003. Generally, amplitude CV was least at the peaks and increased in

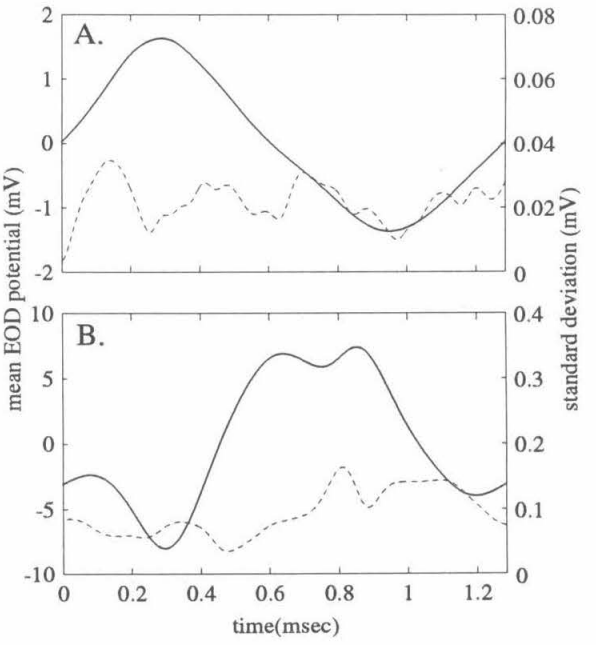

Figure 2. Mean and standard deviation (dashed) of 19 EOD periods sampled at approximately 2 minute intervals for 50 minutes. The scale for the standard deviation is 1/50th the scale of the mean. A. The EOD at the reference electrode in the fish's mouth, and B., at an electrode on the skin of the caudal trunk. Coefficient of variation at the peaks is approximately 0.01 in both cases.

proportion to the slope. As discussed below, this is probably a consequence of small frequency shifts in the EOD.

The EOD stability was similar at all positions, except near the operculum at the end of the experiments. As the fish eventually recovered from the curare and began to respire, the EOD potential amplitude at the operculum was modulated by as much as 8 percent, correlated with the opercular opening, at the respiration rate of a few Hz [13].

Spatial variation of the EOD waveforms.

In contrast to the temporal stability of the EOD at any specific location, the potential waveform varied considerably with position, both on and near the fish. Each fish appeared to have a unique potential pattern, and we were able to recognize individuals based on their EOD maps, although our sample size was too small for rigorous statistical analysis. Here we present in detail the EOD of a 19 cm female. Fig. 3A shows the RMS amplitude of the EOD and its first five spectral harmonics along the fish's midline. Over much of the trunk, the second harmonic (twice the fundamental) was roughly one eighth the amplitude of the fundamental. However near the middle of the fish the second harmonic increased and surpassed by nearly a factor of two the amplitude of the fundamental, before falling to half the fundamental amplitude along the tail.

The higher harmonics also contribute significantly to the relative timing of peaks and zeros along the body. The phase of the fundamental alone is compared to the timing of the zero crossing of the EOD in Fig. 3B. In this fish, harmonics shifted the timing of the positive slope zero crossing with respect to the fundamental, so that this zero crossing remained nearly synchronous over 80% of the body. The negative slope zero crossing of the EOD (corresponding to the beginning of inward current flow) is much less synchronous, but varies more smoothly along the body. Behind the midpoint, the "triphasic" region had two zero crossings of each slope per period, up to the last 15% of the body, where the positive slope zero crossing is delayed by approximately 220 degrees

relative to the mouth. In other fish examined, the zero crossings were not as well synchronized along the trunk, and could be more appropriately described as sweeping along the entire body (see below).

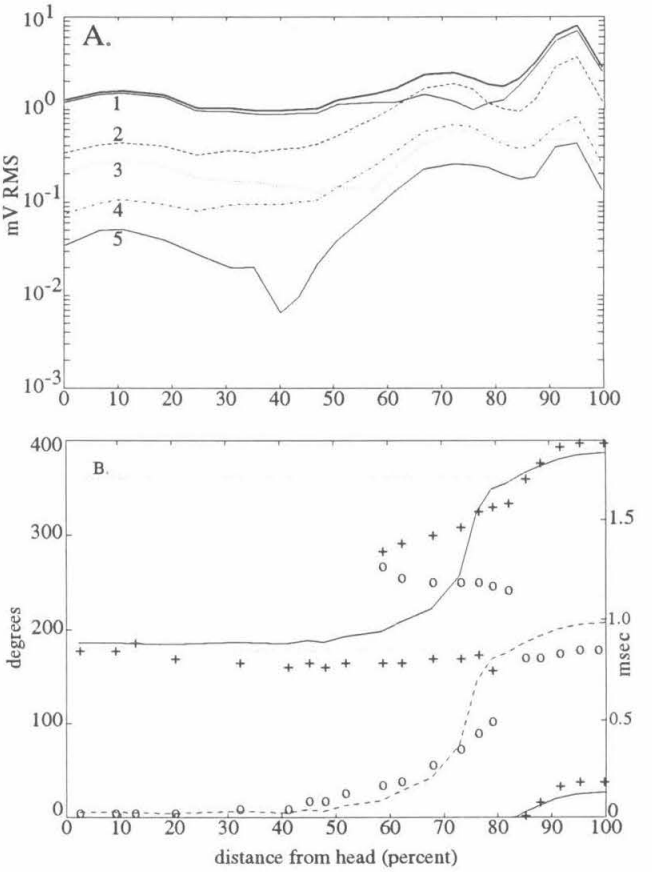

Figure 3. A. RMS potential of the EOD along the midline of a 19 cm female *A. leptorhynchus*. Bold curve is the RMS amplitude of the full-spectrum EOD and the traces labeled 1-5 are amplitudes of the fundamental and successive harmonics extracted from the EOD by Fourier analysis. Note there is no point at which the potential is always zero. B. Phase and latencies of the zero crossings of the EOD fundamental and the full spectrum EOD, relative to the negative slope zero crossing in the mouth. The negative and positive slope zero crossings of the fundamental are shown with dashed and solid lines respectively, and those of the full spectrum EOD are shown with 'o' and '+' respectively. Horizontal dotted lines are at 180 and 360 degrees. The EOD is multiphasic between approximately 55%-85% from the head, where both zero crossings are plotted.

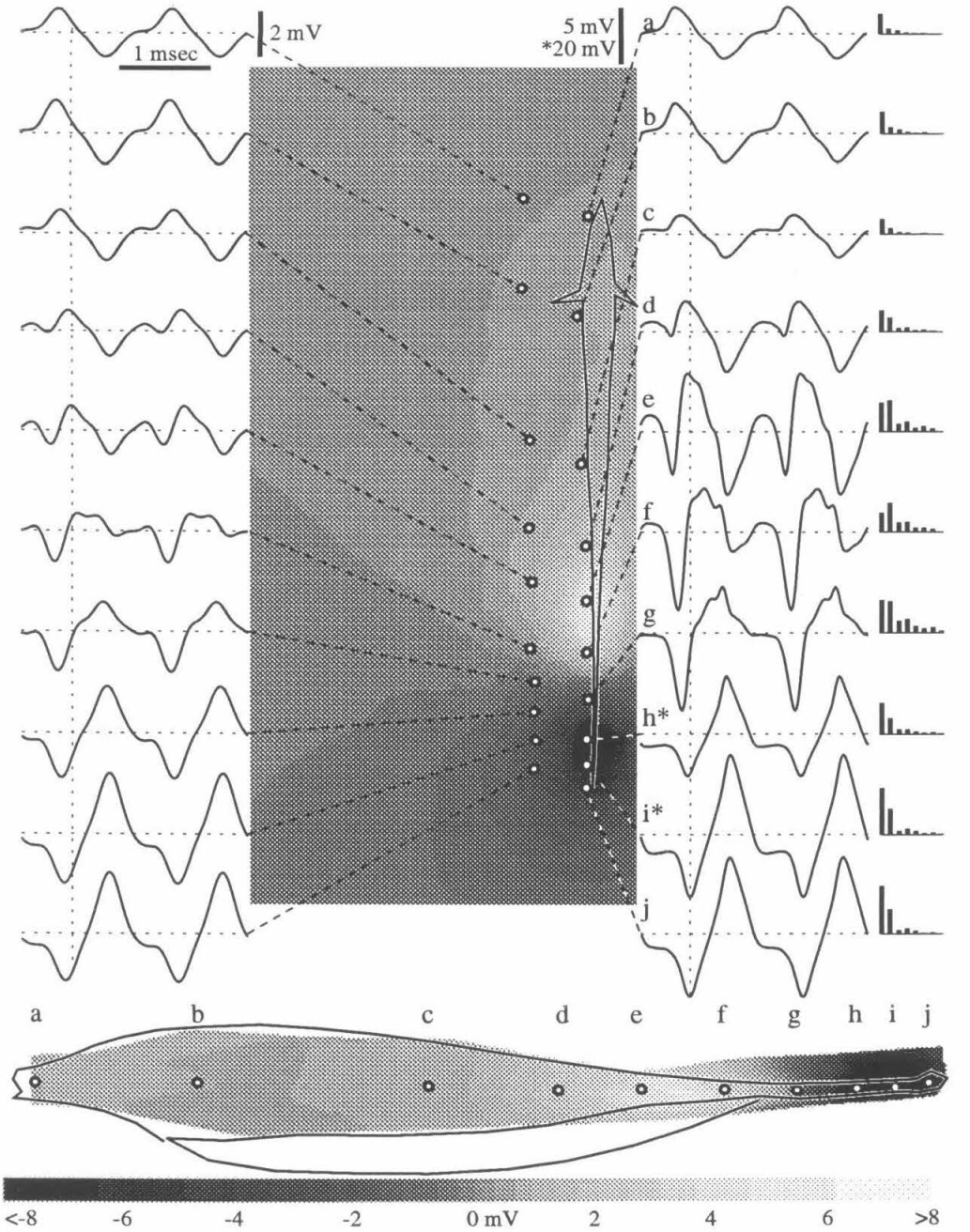

Figure 4. An illustration of how the EOD waveforms measured at different locations were used to construct the grayscale images. The waveforms shown (two EOD periods) were measured at points indicated by the black circles. The beginning of each waveform is in phase with the positive slope zero crossing of the EOD recorded in the fish's mouth. On the right side

are amplitude spectra of the fundamental and the next seven harmonics, with the same vertical scale as the corresponding waveforms. The grayscale frames correspond to the phase marked on the waveforms by the vertical dotted lines. The letters above the skin view indicate the corresponding locations of the waveforms measured on the fish's midline.

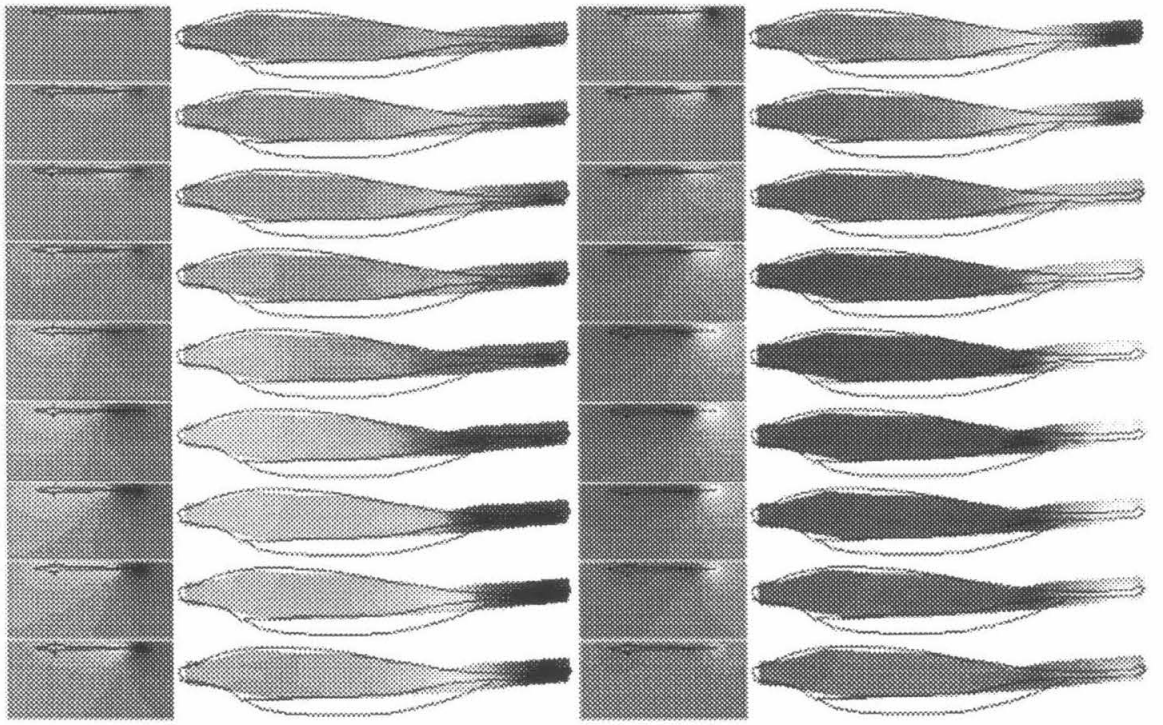

Figure 5. Grayscale images of one period of the EOD potential in the midplane and on the skin of the same fish as Fig. 4. Successive frames are 90 μsec apart with the first frame corresponding to the positive slope zero-crossing of the EOD in the mouth. Grayscale is the same as in Fig. 4.

The relative motion of the peaks and zero crossings is evident in the time domain. Fig. 4 shows a set of phase-locked waveforms along the midline of the same fish as in Fig. 3. The EOD differs significantly from a sinusoid over at least one third of the body and tail, and there is no point where the potential is always zero. Although single electrode recordings illustrate these complex waveforms, the overall spatiotemporal structure of the EOD potential across a fish's entire body is more readily apparent in the grayscale representation.

The grayscale maps reveal that the potential peaks (positive and negative) of the EOD move along the body, spontaneously growing and shrinking, and exactly repeating their pattern every period. For example, the potential of the same fish is shown in Fig. 5 at approximately 90 μsec intervals, covering one full period of 1.6 msec. Beginning with the first frame, the EOD is weak over most of the body, except for two negative peaks on the tail separated by a small positive region. The head is slightly negative and the caudal end of the body slightly positive. In the next frame, the tail potential becomes more negative, overriding the small positive peak. The potential at the caudal end of the trunk and head gradually increases over the subsequent two frames. From the fifth through seventh frame, the head and trunk rapidly become positive while simultaneously the negative peak at the tail spreads rostrally. The head potential subsequently decreases and a positive region propagates caudally, finally wiping out the negative peak at the tail in frame 13. Over the second half of the EOD cycle the head and most of the trunk are negative. The positive region of the tail shrinks monotonically until the beginning of the next EOD period.

In several fish the peaks and zeros of the EOD appeared to propagate from head to tail. For example, column A of Fig. 6 shows a pronounced propagation of EOD peaks, especially along the tail. Phase velocities in the tail region were calculated between 5 and 10 cm/msec. The peaks at the head and tail are also approximately 90° out of phase with each other, with an additional 90° phase shift occurring over several centimeters behind the

tail. The EOD's of the other two fish (Fig. 6 C and D) show a less pronounced propagation, with some peaks appearing to grow and decay without substantial movement.

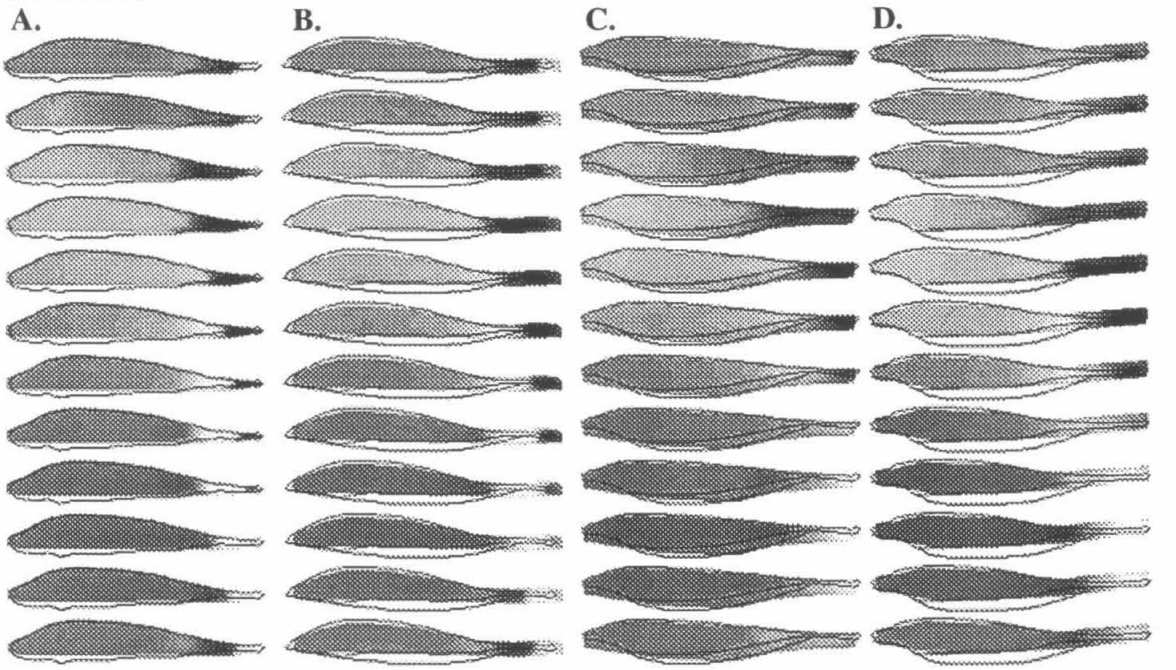

Figure 6. Twelve equally spaced phases corresponding to one EOD period on the skin of three *A. leptorhynchus*. Body lengths are normalized to aid comparison. A, B. A 21.2 cm male (A), and the same fish 9 months later (B), now 26 cm in length. C, D. Two other fish for comparison. Grayscale is the same as in Fig. 4.

3.4. Discussion

Stability

The detection of small field perturbations induced by objects presumably requires electric fish to maintain a stable EOD over short periods of time. Bullock [14] proposed the electric organ of *Apteronotus* is the most stable biological oscillator known, after reporting

a frequency coefficient of variation of 0.00012 over several seconds (similar to an electronic function generator). Our results show that over 50 minutes the variation in frequency is of order 0.001, and furthermore the EOD amplitude and waveform are stable and conserved at all locations in space and over time scales up to at least an hour in curarized fish.

The measurements of EOD amplitude variance likely represent upper limits. We measured frequency drifts of up to 5 Hz per hour (which could be a consequence of small temperature changes [15]) and occasional frequency steps. These could constitute a major component of the amplitude variance, since waveforms of different frequencies cannot be averaged by time-shifting alone. The variance in amplitude measurement due to frequency shifts is proportional to the slope of the waveform and the distance in samples (time) from the phase-locking trigger (positive slope zero-crossing). Both these trends are visible in Fig. 2.

In addition to amplitude and frequency stability, the spatiotemporal pattern of the EOD waveform also appeared stable for the fish that were mapped on multiple occasions. We measured one large male 8 months after its initial mapping, during which time the fish grew from 21.2 cm to 26 cm in length. The EOD pattern remained similar over this extended time scale when normalized for frequency and the change in body length (Fig. 6, columns A and B). This long term stability seems particularly surprising when one considers the changes in physical and electrical properties that must accompany aging and growth. For example, changes in axon diameter and length almost certainly affect the EOD. In this fish, body length increased 20% in the eight months between recordings, yet the high spatial and temporal frequency components of the EOD were conserved.

The variation between the EOD patterns for the same fish on different days (Fig. 6 A and B) was qualitatively less than between different fish. In fact, the shape of the EOD potential appeared to be unique to each individual (in the few cases that we have studied). If the EOD waveform were to serve as a "fingerprint" that conspecifics use to identify each

other at short range, such stability would be advantageous, as would the ability to modulate the EOD pattern as an individual's role in its community changes. The EOD frequency and waveform is modulated over long time scales by steroids [16], [17]. Of course, for individual recognition to occur, the fish must have means of interpreting the complicated interference patterns resulting from interacting fields (see below).

Command pathway and electric organ.

The potential maps may also provide clues about the composition and timing of the electric organ activity and its command pathway, which has been the subject of numerous studies (e.g., [8], [18]). EOD stability has been mainly attributed to the medullary pacemaker nucleus in the brainstem which controls the activity of the electric organ. The pacemaker in *Apteronotus* is much larger and contains many more neurons than other gymnotiforms [19]. Because these cells are tightly coupled electrotonically, the temporal jitter in the command signals could be reduced in proportion to the square root of the number of cells (by the law of large numbers). However, the extreme stability of the EOD waveform, with stable harmonics exceeding 5 kHz, implies all components of the electromotor system must be functioning at high fidelity. Even with a stable signal from the pacemaker nucleus, this signal must still propagate through several other components.

The EO in *Apteronotus* extends along the entire trunk to the tip of the tail, lying ventral to the spinal cord [8]. Axons from the relay cells in the pacemaker project down the spinal cord to innervate electromotor neurons. At regular intervals along the spinal cord, the electromotor neuron axons descend in nerve branches into the EO, where the specialized axon terminals function as electrocytes [20]. Neurotransmission is electrotonic at every stage of this command pathway.

Our data suggest that a distinction must be drawn between local synchronized discharge to generate large stable fields, and overall synchronization of the entire electric organ, particularly in wave fish like *Apteronotus*, with long electric organs. Bennett, in

his 1971 review, showed that synchronization plays an important role in generating large stable output because the currents of individual electrocytes are channeled and summed to produce the overall EOD. He also proposed mechanisms for achieving simultaneous activation along the electric organ, using conduction delays to equalize effective command path lengths. But synchrony of electrocyte discharge has been hypothesized to be more crucial for pulse species, while regularity of discharge frequency is paramount for wave fish [18]. Our phase-locked recordings from *A. leptorhynchus* show that, while local groups of electrocytes might be tightly synchronized, the discharge of the EO as a whole is not in unison.

Most of the potential maps of *A. leptorhynchus* displayed a rostro-caudal propagation of the EOD peaks and zeros. This was especially apparent in the tail, where the EO is nearer to the skin and not surrounded by high conductivity body tissue. These potential peaks could be caused by part of the locally generated current exiting the electric organ along its length instead of being channeled to its endpoints. While the peaks of the potential are not necessarily centered over the most active segments of the EO, the observed propagation does suggest sequential activation of electrocytes along the electric organ. Consistent with this interpretation, it has been demonstrated in the related species, *A. albifrons*, that axons from the pacemaker relay cells run the length of the spinal cord and contact electromotor neurons at all spinal levels [19]. The apparent propagation of EOD peaks could therefore result from uncompensated propagation delays down the spinal cord of the pacemaker command signal. The particularly long electric organs of these fish, coupled with their high firing frequencies, may make it more difficult or even impractical to achieve global synchronization.

For comparison, the pulse gymnotid *Gymnotus carapo* also has a long EO extending over most of its body length, and a complex discharge that indicates "leaky insulation" around the organ [21]. However in order to generate effective pulses, this species possesses a mechanism to compensate for different conduction path lengths.

Pacemaker relay axons terminate in specific segments of the spinal cord [19], and fibers in the electromotor bulbospinal tract have a wide range of conduction velocities distributed according to path length, from 1 to 9.1 cm/msec [22]. Therefore command signals simultaneously traveling to widely separated EO segments can remain synchronized upon reaching their respective destinations. If command signal conduction velocities in *A. leptorhynchus* are of the same order of magnitude, but there is no compensatory mechanism, then one might expect the EO segments to be activated sequentially. The phase velocities of potential peaks we measured along the tail of *A. leptorhynchus*, from 5 to 10 cm/msec, are consistent with these hypotheses.

The steep decay of the higher temporal frequency components with distance from the EO is another indication that electrocyte activation is farther out of phase over more distantly separated sections of the EO. On the skin near the thin part of the tail, stable frequency components of up to several kHz are observed, whereas far from the fish the fundamental frequency dominates the EOD. This can be explained as follows. The potential at any point outside the fish is due to the superposition of the discharges from the entire electric organ; however, at locations near the EO, for example on the tail, the potential is dominated by only the few nearest segments. Temporal shifts in waveforms of individual electrocytes or EO segments cause phase shifts proportional to the frequency, so a given time shift will cause greater interference of the higher harmonics compared to the fundamental. Thus, far from the fish where many segments contribute to the EOD, the high frequency components of the segments will destructively superpose if their phases differ, but the lower frequency components can still constructively add to produce a large amplitude. This mechanism could also explain why EOD propagation is much less apparent on the trunk. The high conductivity of the internal body tissue increases the effective electrical distance between the EO and the skin. This tends to average the EOD from distant EO segments within the trunk.

Finally, the fact that the far field of all electric fish is dipolar [6] is the consequence of an analogous phenomenon. Just as the waveform at a particular point can be described as a superposition of sine waves of different frequencies and phases (its Fourier series), the electric potential and field in the space surrounding a distribution of sources can be decomposed as a superposition of multipole moments (e.g., [23]). Each successive multipole moment contains higher spatial frequency information about the field, but decays more steeply with distance from the sources than the lower order multipole. Thus, far from the fish the lowest multipole moment, the dipole, will dominate the field.

Electroreceptors and electrolocation.

It is still an open question how much of the phase and harmonic components of the EOD we have described here are transduced by the electroreceptors. Whereas certain EOD components may be just artifacts of controlling a large fast EO, others might have evolved to facilitate electrolocation and communication. Although electric sense inherently has relatively low spatial resolution (e.g., compared to vision), since there is no mechanism for focusing electric fields, time domain cues in electric fields are not corrupted by dispersion, as are most other sensory signals. This fact led Hopkins [24] to propose that temporal characteristics of electric fish fields might be even more important for electrolocation than temporal characteristics are in the acoustic modality where, for example, they are the basis for object location in bats and owls. Thus we would expect electroreceptors to respond to the stable phase and harmonic components of the transepidermal EOD waveforms.

Weakly electric fish detect their EOD with an array of several thousand tuberous electroreceptor organs in their skin. In the well-studied case of *Eigenmannia* (EOD fundamental around 300 Hz), tuberous electroreceptors have been classified into two general groups: T units which respond phase-locked to the zero crossing of the EOD, and P units whose response is less dependent on phase and whose probability of firing

encodes EOD amplitude [25], [26]. However, different species of fish appear to differ in the types and proportions of these electroreceptors. There has even been a proposal that there may be a continuum of receptor responses between P and T units in *Eigenmannia* [27].

In the case of *A. albifrons,* which is more closely related to the fish studied here, most tuberous receptors on the body have been reported to correspond to P-type probability encoders rather than the T-type phase detectors [28], [29]. Scheich and Bullock [30] pointed out an inverse correlation between the number of phase encoders and the fundamental EOD frequency in different species. They concluded that the higher frequency EOD discharge of *Apteronotus* (600-1000 Hz) limits the dynamic range of phase coders, therefore making T units less useful than in lower frequency fish like *Eigenmannia.* A number of studies suggest that P units convey some phase information into the CNS (e.g., [31, Fig. 4], [28], [26].).

However, Franchina et al. [32] have recently found evidence that the dorsal filament of Apteronotids contains a population of tuberous receptors resembling phase encoders. The dorsal filament is a thin structure lying in a groove along the center of the back, originating near the middle of the body and extending posteriorly over the EOD triphasic region (see Fig. 42 in [8]). It appears to be contiguous with the body only at the anterior end, where upwards of 200 afferent axons join the lateral line nerves bilaterally (in *A. albifrons*; C. Franchina, personal communication). Much of the filament is situated in the large caudal field, which led Franchina et al. to conclude it could serve as a phase reference for the endogenous EOD. This would make it useful for phase comparisons such as needed in the jamming avoidance response. However, the large caudal field is also quite complicated, especially in the triphasic region where there are high frequency components and multiple zero crossings per period. If the dorsal filament is covered with phase encoders, then the response of the population as a whole will reflect the complex phase relationships seen in the maps, such as the propagation of zero crossings down the

filament. It is also possible that these receptors are sensitive to phase deviations caused by strong external sources. In particular, it would be interesting to determine if the dorsal filament is involved in the identification of nearby conspecifics based on their EOD.

In addition to raising questions about the information encoded by the receptors, the details of these potential maps also highlight likely spatial differences in receptor properties. For example, the substantial rostro-caudal differences we have found in EOD amplitude suggest that electroreceptor thresholds and/or spontaneous activity levels should vary with location on the body surface. The large second harmonic in the caudal trunk could also provide significant stimulus to receptors in that region. Hopkins [28] showed tuning curves for receptors in *A. albifrons* that have two sensitivity peaks, near the EOD fundamental and its second harmonic. More complicated spatial variations in receptor tuning have been found in *G. carapo* [33], [34].

We emphasize that the potentials presented here are recorded with respect to electrical infinity, and are not the potentials across the active membranes of the electroreceptors. We have also measured the EOD potential with respect to an electrode inside a fish's gut. While this more closely approximates the transepidermal potential near the gut electrode, the fish interior was not equipotential. In a 30 cm male, the potential waveform in the gut of the trunk was nearly identical to the potential in the mouth except for amplitude differences; however, towards the tail the waveforms differed as well. The gut potential was 2.7 times larger than in the mouth at a point 3 cm caudal of the operculum, but was only 2.0 times larger 3 cm further caudal.

Another method of estimating the electroreceptor stimulus is from the potential gradient on the skin using differential electrode pairs. This requires consideration of the fish's curvature, and a model of how non-perpendicular current might be channeled to the sensory cells by the high resistance receptor pore walls [30]. Unfortunately, electroreceptor responses to complicated current perturbations are not well understood, even though electroreceptors have played an important role in the elucidation of different

neural codes [2]. We are currently modifying our apparatus to map the electric field vector surrounding the fish, and our preliminary data suggest a strong likeness between the instantaneous potential pattern and the perpendicular electric field when both are measured directly on the fish's skin.

Behavioral significance.

If receptor mechanisms do exist to make use of phase information or harmonic content, the spatial pattern of these differences could contribute to the acquisition of information about local objects and influence the fish's exploratory behavior. Electrolocation is based on the principle that the fish's electric field polarizes an object, inducing a perturbation proportional to the field strength at the object. For example, a small sphere (small compared to the spatial variation in the field) will create a dipolar perturbation. The fish subsequently detects this perturbation field superimposed with the unperturbed EOD on its skin. Near the tail, the potential changes significantly in amplitude and spectral composition over millimeter distances. Therefore the perturbation due to a nearby object is not a linear function of the normally detected EOD field. For this reason, an object near the tail will not simply multiply the field on nearby receptors by some constant amount, but will superimpose a field with waveform like that at the object. Having different regions of the electric organ active at different times, the fish could accumulate spatial information about objects from the relative timing of the field perturbations

Regional variations in the potential and its spatial derivatives may allow electroreceptors in different regions of the body to fulfill different computational roles in electroreception. In particular, because the caudal electric field decreases with distance more steeply than at the head, we speculate that caudal receptors might preferentially encode object distance, and the rostral receptors that are in a weaker, more uniform field might convey higher resolution information about object structure. The electric "image" of

a small object decreases with distance like the field. Thus as the body-to-object distance is modulated (e.g., by tail wagging, a common exploratory behavior), the change in the perturbation field will be larger for an object near the tail versus near the trunk. Furthermore, the spatial nonuniformities of the caudal field could confound an object's spatial structure. In contrast, the more uniform trunk field, with its lower sensitivity to changes in object-body distance and location, would be more suited to extracting object structure. The spatial distribution of tuberous electroreceptors is compatible with this idea, with a higher density in rostral regions, especially around the head, compared to caudal regions (15/mm^2 vs. about 3/mm^2 in *A. albifrons*; [35]).

We have sought to quantify the temporal and spatial structure of the EOD potential as an initial step in our efforts to understand electroreception from a computational point of view. The results of these experiments have suggested a number of new conjectures regarding the interaction of the fish, its fields, and objects in its environment. We are currently pursuing these ideas by mapping the electric field vector on and around the fish, as well as quantifying perturbations due to nearby objects. This work is intended to facilitate the quantification of electrosensory input as it enters the central nervous system, as well as to provide a more solid basis for interpreting the sensory consequences of the behavioral strategies used by electric fish to locate and identify objects in their environment.

Acknowledgements

We thank Mark Nelson and Caroly Shumway for their ideas and technical assistance, Mike Walsh for advice on electronics, and Dave Bilitch for advice on C programming. We are grateful to the electric fish research community in general, and especially to Lenny Maler, Walter Heiligenberg, and Joe Bastian for their encouragement and advice in getting started. This work was funded in part by NRSA Fellowship Grant #GMO7737, an ONR Graduate Fellowship, and NIH BRSG #RR007003.

Note added in proof

McGreggor and Westby [36] have reported the EOD of *G.carapo* is used for identification of individual conspecifics.

References

[1] Carr, C.E., "Neuroethology of Electric Fish," *BioScience*, **40**:259-267, 1990.

[2] Bullock, T.H. and Heiligenberg, W., *Electroreception*, John Wiley & Sons, Inc., 1986.

[3] Lissmann, H.W., "Electric Location By Fishes," *Sci. Am.*, **208**:50-59, 1963.

[4] Hoshimiya, N., Shogen, K., Matsuo, T., and Chichibu, S., "The *Apteronotus* EOD Field: Waveform and EOD Field Simulation," *J. Comp. Physiol.*, **135**:283-290, 1980.

[5] Heiligenberg, W., "Electrolocation of Objects in the Electric Fish, Eigenmannia (Rhamphichthyidae, Gymnotoidei)," *J. Comp. Phys.*, **87**:137-164, 1973.

[6] Knudsen, E., "Spatial Aspects of the Electric Fields Generated by Weakly Electric Fish," *J. Comp. Physiol.*, **99**:103-118, 1975.

[7] Hagedorn, M., "The Ecology, Courtship, and Mating of Gymnotiform Electric Fish," in *Electroreception*, Bullock, T.H. and Heiligenberg, W. (Eds.), pp. 497-525, Wiley, 1986.

[8] Bennett, M.V.L., "Electric Organs," in *Fish Physiology*, Hoar, W.S. and H., R.D. (Eds.), pp. 347-491, Academic Press, 1971.

[9] Robinson, D.A., "The Electrical Properties of Metal Microelectrodes," *Proc. IEEE*, **56**:1065-1071, 1968.

[10] Horowitz, P. and Hill, W., *The Art of Electronics*, 2nd Edition, Cambridge University Press, 1989.

[11] Rasnow, B., Assad, C., Nelson, M.E., and Bower, J.M., "Simulation and Measurement of the Electric Fields Generated by Weakly Electric Fish," in *Advances in Neural Information Processing Systems 1*, Touretzky, D.S. (Ed.), pp. 436-443, Morgan Kaufmann, 1989.

[12] Watson, D.F., "Computing the N-Dimensional Delaunay Tesselation with Application to Voroni Polytopes," *Computer J.*, **24**:no. 2, 167-172, 1981.

[13] Montgomery, J.C., "Noise Cancellation in the Electrosensory System of the Thornback Ray: Common Mode Rejection of Input Produced by the Animal's own Ventilatory Movement," *J. Comp. Physiol.*, **155**:103-111, 1984.

[14] Bullock, T.H., "The Reliability of Neurons," *J. Gen. Physiol.*, **55**:565-584, 1970.

[15] Enger, P.S. and Szabo, T., "Effect of Temperature on the Discharge Rates of the Electric Organ of some Gymnotids," *Comp. Biochem. Physiol.*, **27**:625-626, 1968.

[16] Bass, A.H. and Volman, S.F., "From Behavoir to Membranes: Testosterone-Induced Changes in Action Potential Duration in Electric Organs," *Proc. Natl. Acad. Sci. USA*, **84**:9295-9298, 1987.

[17] Zakon, H.H., "Hormone-Mediated Plasticity in the Electrosensory System of Weakly Electric Fish," *Trends Neurosci.*, **10**:412-421, 1987.

[18] Dye, J.C. and Meyer, J.H., "Central Control of the Electric Organ Discharge in Weakly Electric Fish," in *Electroreception*, Bullock, T.H. and Heiligenberg, W. (Eds.), pp. 71-102, Wiley, 1986.

[19] Ellis, D.B. and Szabo, T., "Identification of Different Cell Types in the Command (Pacemaker) Nucleus of Several Gymnotiform Species by Retrograde Transport of Horseradish Peroxidase," *Neuroscience*, **5**:1917-1929, 1980.

[20] Waxman, S.G., Pappas, G.D., and Bennett, M.V.L., "Morphological Correlates of Functional Differentiation of Nodes of Ranvier along Single Fibers in the Neurogenic Electric Organ of the Knife Fish *Sternarchus*," *J. Cell. Biol.*, **53**:210-224, 1972.

[21] Caputi, A., Macadar, O., and Trujillo-Cenóz, O., "Waveform Generation of the Electric Organ Discharge in *Gymnotus carapo*," *J. Comp. Physiol.*, **165**:361-370, 1989.

[22] Lorenzo, D., Sierra, F., Silva, A., and Macadar, O., "Spinal Mechanisms of Electric Organ Synchronization in Gymnotus carapo," *J. Comp. Physiol.*, **167**:447-452, 1990.

[23] Jackson, J.D., *Classical Electrodynamics*, Wiley & Sons, 1975.

[24] Hopkins, C.D., "Temporal Structure of Non-Porpagated Electric Communication Signals," *Brain Behav. Evol.*, **28**:43-59, 1986.

[25] Heiligenberg, W., "Electrosensory Maps Form a Substrate for the Distributed and Parallel Control of Behavioral Responses in Weakly Electric Fish," *Brain Behav. Evol.*, **31**:6-16, 1988.

[26] Scheich, H., Bullock, T.H., and Hamstra, R.H., "Coding Properties of Two Classes of Afferent Nerve Fibers: High-Frequency Electroreceptors in the Electric Fish, Eigenmannia," *J. Neurophys.*, **36**:39-60, 1973.

[27] Viancour, T.A., "Electroreceptors of a Weakly Electric Fish. I. Characterization of Tuberous Receptor Organ Tuning," *J. Comp. Physiol.*, **133**:317-325, 1979.

[28] Hopkins, C.D., "Stimulus Filtering and Electroreception: Tuberous Electroreceptors in Three Species of Gymnotid Fish," *J. Comp. Physiol.*, **111**:171-207, 1976.

[29] Zakon, H.H., "Variation in the Mode of Receptor Cell Addition in the Electrosensory System of Gymnotiform Fish," *J. Comp. Physiol.*, **262**:195-214, 1987.

[30] Scheich, H. and Bullock, T.H., "The Detection of Electric Fields from Electric Organs," in *Handbook of Sensory Physiology*, Fessard, A. (Ed.), pp. 201-256, Springer-Verlag, 1974.

[31] Bastian, J., "Electrolocation I. How the Electroreceptors of Apteronotus albifrons Code for Moving Objects and Other Electrical Stimuli," *J. Comp. Physiol.*, **144**:465-479, 1981.

[32] Franchina, C., Hopkins, C.D., and Schneiderman, A., "The Dorsal Filament of the Weakly Electric Apteronotids is Specialized for Electroreception," in *Soc. Neurosci. Abstr.,* 16:1327, 1990.

[33] Watson, D. and Bastian, J., "Frequency Response Characteristics of Electroreceptors in the Weakly Electric Fish, *Gymnotus carapo*," *J. Comp. Physiol.*, **134**:192-202, 1979.

[34] Bastian, J., "Variations in the Frequency Response of Electroreceptors Dependent on Receptor Location in Weakly Electric Fish (Gymnotoidei) with a Pulse Discharge," *J. Comp. Physiol.*, **121**:53-64, 1977.

[35] Carr, C.E., Maler, L., and Sas, E., "Peripheral Organization and Central Projections of the Electrosensory Nerves in Gymnotiform Fish," *J. Comp. Neurol.*, **211**:139-153, 1982.

[36] McGreggor, P.K. and Max Westby, G.W., "Discrimination of Individually Characteristic Electric Organ Discharges by a Weakly Electric Fish," *Anim. Behav.*, **43**:977-986, 1992.

Chapter 4

The Electric Field of *Apteronotus*

4.1. Introduction

Weakly electric fish of the genus *Apteronotus* generate a weak, high frequency electric field (<100 mV/cm, 0.5-10 kHz) which permeates their local environment. These fish are acutely sensitive to perturbations in the electric field from nearby objects whose impedance is different from the surrounding water [1]. To understand the operating principles of electric sense, we have been studying by measurement and simulation the fish's self-generated electric potential and field [2]. In a previous study [3], we mapped the electric potential on the fish's skin and midplane, and showed it is a complicated and highly stable function of space and time. In this paper, we present the electric field vector, measured in 3-dimensions near a fish.

The electric field is more fundamental to electrolocation than is the corresponding electric potential. A small spherical object near the fish becomes polarized or develops a surface charge, resulting in a dipolar modulation that is directly proportional to the electric field. Larger objects generate more complicated modulations, that are also proportional to the average electric field at the object. The fish detects these modulations, attenuated by distance between the object and the fish's electroreceptors. Therefore the electric field away from the fish is a better indicator of electrolocation sensitivity than the corresponding potential.

The electric field vector, $\mathbf{E}$, is related to the current density vector, $\mathbf{J}$, by Ohm's law: $\mathbf{E} = \rho\mathbf{J}$, where ρ is the local resistivity. In the water around the fish, the resistivity is constant (ρ = 5 kΩ-cm), thus the electric field and current are directly proportional and in

phase with each other. Inside the fish and dielectrics, ρ could be a complex function of frequency and other parameters.

Because the electric field is a 3-dimensional vector function of three spatial dimensions and time, it is complicated to visualize. The time dependence can be eliminated by replacing the EOD waveforms at each point in space with amplitude and phase functions, $V_h(\mathbf{x})$ and $\varphi_h(\mathbf{x})$, of harmonics h at location $\mathbf{x}$. These functions are related to EOD waveforms by the Fourier transform:

$$V(\mathbf{x},t) = \sum_{h=1}^{\infty} V_h(\mathbf{x}) e^{i(\omega h t + \varphi_h(\mathbf{x}))} = \sum_{h=1}^{\infty} V_h(\mathbf{x}) e^{i\omega h t} e^{i\varphi_h(\mathbf{x})}. \tag{4.1}$$

The fish's fundamental frequency is ω (in radians/sec), and $i = \sqrt{-1}$. The higher order harmonic amplitudes, $V_h(\mathbf{x})$, decrease rapidly as $h \to \infty$, so the entire waveform at any point can be accurately reconstructed from fewer than 10 complex numbers (Fig. 4.1). The electric field components can similarly be described by Fourier amplitudes, $E_{k,h}(\mathbf{x})$ and phases $\varphi_{k,h}(\mathbf{x})$, for each directional component, k.

The electric field is mathematically equivalent to the negative gradient of the potential. Thus the component of the field in direction x_k is:

$$E_k(\mathbf{x},t) = -\frac{\partial V}{\partial x_k} = -\sum_{h=1}^{\infty} \left(\frac{\partial V_h}{\partial x_k} + iV_h \frac{\partial \varphi_h}{\partial x_k} \right) e^{i(\omega h t + \varphi_h(\mathbf{x}))} \equiv \sum_{h=1}^{\infty} E_{k,h}. \tag{4.2}$$

Changes in phase as well as amplitude of the potential contribute to the electric field. Although the electric field can in principle be estimated from potential maps by Eqn. 4.2, this amplifies noise and measurement errors. In this study, we directly measured the potential gradient differentially between pairs of four electrodes arranged in a small, rigid array.

4.2. Materials and Methods

The experimental materials and methods are similar to those described in [3]. We present here just the differences.

Subjects

We studied the electric field of three *A. leptorhynchus* and two *A. albifrons*. Before recording, each fish was paralyzed with intramuscular injections of 10 to 25 µl Flaxedil (gallamine triethiodide), and occasional supplemental injections (e.g., 5 µl after 3 hours). The fish were mapped in a 60 x 60 x 18 cm tank, oriented with the mapping plane parallel to the water surface. All the data presented here is from one 21 cm female *A. leptorhynchus*, taken during a contiguous 6 hour period. Comparisons with the other fish are discussed.

Electrodes

We used an array of four electrodes to measure the electric field components around each fish. Each electrode was made from a 25 µm diameter silver wire whose tip was melted into a 150-250 µm diameter ball. The wire was insulated and held rigid in a 1 mm OD glass pipette with a long slender tip created in an electrophysiology electrode puller. Four such electrodes were glued together so their tips defined three Cartesian axes. Rather than attempting to construct the array to extreme precision, the actual electrode positions deviated significantly from this plan, and were calibrated before the experiments (see below). The electrodes had impedances of approximately 40 kΩ, dominated by spreading resistance of the water [4] ($R_s = \rho/4\pi r_e$, where ρ = water resistivity = 5 kΩ-cm, and r_e = electrode radius ≈ 100 µm).

Three larger (and lower impedance) stationary electrodes were mounted on the tank walls. Lateral of the fish, an electrode served as the distant potential reference. A pair of electrodes on opposite walls along the fish's rostrocaudal axis was used for a phase reference. All EODs were aligned to begin in phase with the positive slope zero crossing of the fundamental frequency component recorded between this pair (head–tail).

Electrical instrumentation

Each electrode was connected to a high impedance (>100 MΩ) follower amplifier mounted nearby the array. The follower outputs were differentially amplified and simultaneously sampled with six 16-bit delta-sigma analog-to-digital converters (ADCs) at 48,000 samples/second/channel. By sharing a clock signal, the converters were synchronized to within a few nanoseconds of each other. The analog bandwidth was extremely wide, 10 Hz to 60 kHz (–3 dB), to maintain constant gain and phase responses to the EOD fundamental and harmonics. Noise was approximately 1.6 μV RMS over a 10 kHz bandwidth, on the order of the Johnson noise of the electrodes [5].

Computing electric field vectors

The electric field vector can be computed from the set of interelectrode potential differences. When the array is in a field, $\mathbf{E} = (E_x, E_y, E_z)$, averaged over the volume of the array, the measured potential differences between electrodes are proportional to the field and the interelectrode distances:

$$\begin{bmatrix} \varphi_2 - \varphi_1 \\ \varphi_3 - \varphi_1 \\ \varphi_4 - \varphi_1 \end{bmatrix} = \begin{bmatrix} x_2 - x_1 & y_2 - y_1 & z_2 - z_1 \\ x_3 - x_1 & y_3 - y_1 & z_3 - z_1 \\ x_4 - x_1 & y_4 - y_1 & z_4 - z_1 \end{bmatrix} \begin{bmatrix} E_x \\ E_y \\ E_z \end{bmatrix} \tag{4.3}$$

where electrode k, at position (x_k, y_k, z_k) is at potential φ_k. The electric field components are computed from the potential differences by inverting this equation. The accuracy of the field components is directly related to the accuracy with which the interelectrode spacings, of order 1-2 mm, can be determined. If the array was constructed perfectly orthogonal, then the matrix in Eqn. 4.3 would be diagonal, and each electric field component would be proportional to the potential difference between a single electrode pair. However, the array was only approximately orthogonal. Thus the pairwise measured potential differences consisted of linear combinations of the electric field components, which had to be resolved.

Calibrating interelectrode distances

The array geometry was determined by measuring a known electric field. The difference between measured and theoretical data was minimized by varying the electrode positions using two successive Nelder-Meade simplex optimizations [6]. A dipole made of two ball bearings connected to a function generator was placed in the recording tank. The potential, measured relative to an electrode on the tank wall near the dipole zero-potential plane, and the potential differences between pairs of electrodes in the array, were measured as the array moved along several paths, lateral, perpendicular, and above the dipole. The theoretical potential at a point $\mathbf{x}$ (in an infinite tank) is:

$$V(\mathbf{x}) = \frac{\rho I}{4\pi}\left(\frac{1}{|\mathbf{x}-\mathbf{x}_1|} - \frac{1}{|\mathbf{x}-\mathbf{x}_2|}\right) \tag{4.4}$$

where I is the current supplied by a function generator, ρ is the water resistivity, and $\mathbf{x}_1$, $\mathbf{x}_2$ are the position vectors of the two poles. Because of the large tank size (60x60x18 cm) relative to the dipole separation (approximately 4 cm), the side walls had negligible effect near the poles, however the tank floor and water surface confined the field. These surfaces were accounted for analytically using the method of images [7].

The first optimization made small adjustments to the visually estimated pole positions $\mathbf{x}_1$ and $\mathbf{x}_2$ by minimizing the difference between measured and computed potential (relative to the wall). The second optimization computed the inverse of the interelectrode distance matrix, by minimizing the difference between the field components computed from the differential measurements, and the theoretical electric field of a discrete dipole:

$$\mathbf{E}(\mathbf{x}) = \frac{\rho I}{4\pi}\left(\frac{\mathbf{x}-\mathbf{x}_1}{|\mathbf{x}-\mathbf{x}_1|^3} - \frac{\mathbf{x}-\mathbf{x}_2}{|\mathbf{x}-\mathbf{x}_2|^3}\right). \tag{4.5}$$

Since the field decays with distance faster than the potential, the vertical water surfaces had smaller effects, and were ignored. The array used in the experiments presented here had interelectrode spacings matrix (Eqn. 4.3, in mm) of:

$$\begin{bmatrix} 2.203 \pm 0.014 & 0.264 \pm 0.003 & 0.177 \pm 0.022 \\ 0.452 \pm 0.006 & 1.315 \pm 0.000 & -0.038 \pm 0.002 \\ 0.290 \pm 0.015 & 0.053 \pm 0.068 & -1.231 \pm 0.034 \end{bmatrix} \quad (4.6)$$

where the uncertainty is the standard deviation from two independent calibrations (average standard deviation is 18 μm).

Data analysis

From the digitized time series, an integral number of EOD periods nearest to one or two periods of 60 Hz was Fourier transformed. Transforming an integral number of periods minimizes aliasing errors and the need for windowing the data [8]. Because *Apteronotus* has an extremely stable and band-limited EOD (Fig. 4.1 and [3]) the waveform can be accurately reconstructed from the complex amplitudes (or real amplitudes and phases) of its fundamental and lowest several harmonics. The amplitudes of the first 10 harmonics were computed by convolving the time series with precomputed sine and cosine series for each harmonic (the classical Fourier transform). This calculation is considerably faster than the Fast Fourier Transform, which computes amplitudes of all frequencies.

The ADCs sampled continuously and asynchronously with respect to the EOD, therefore the phases of successive records were only aligned within one sample, or 21 μsec of each other. Additional synchronization was achieved computationally by shifting phases of the Fourier data so that the fundamental on the phase reference channel were exactly aligned. We define zero phase as the positive-slope zero crossing of the EOD fundamental recorded between the reference electrodes. All the data shown below are aligned with this phase of the EOD.

4.3. Results

EOD Stability

The stability of the EOD waveform is extraordinary, and fundamental to our method of measuring the field maps. Figure 4.1 shows statistics of the phase reference signal recorded between two stationary electrodes placed along the fish's rostro-caudal axis. The mean and standard deviation of each phase of this reference signal, measured 755 times every 3–4 seconds over 25 minutes (the time it took to map the field in a plane), is shown in Fig. 4.1A. The errorbars of most phases are indistinguishable, on the order of 0.005 times the peak amplitude. The Fourier amplitudes of this data are shown in Fig. 4.1B, with the standard deviation shown by errorbars and the lower set of points. The coefficient of variation (standard deviation/mean) of the fundamental, second harmonic (twice the fundamental), and third harmonic amplitudes are 0.0051, 0.0052, and 0.0090. The higher harmonics have lower amplitude and amplitude variance, and the variance is ultimately limited by measurement noise.

The standard deviation of the harmonic phases is shown in Fig. 4.1C. Individual waveform measurements were aligned by equating the phases of the fundamental. Therefore the standard deviation of the fundamental is, by construction, zero. The phases of the second through fourth harmonics, relative to the fundamental, varied within 0.2, 0.3, and 0.7 degrees (standard deviation) over the 25 minute period. These harmonics have frequencies of approximately 1.6, 2.4, and 3.2 kHz respectively. Changing units from frequency to time, these phase variations correspond to temporal jitter of 340, 360, and 620 nanoseconds respectively. We observed similar stability in the fish's near field, using a wire inside the respiration tube in the fish's mouth as a phase reference signal. All the fish we studied had ≤ 1 μsec of phase jitter in their lowest harmonics.

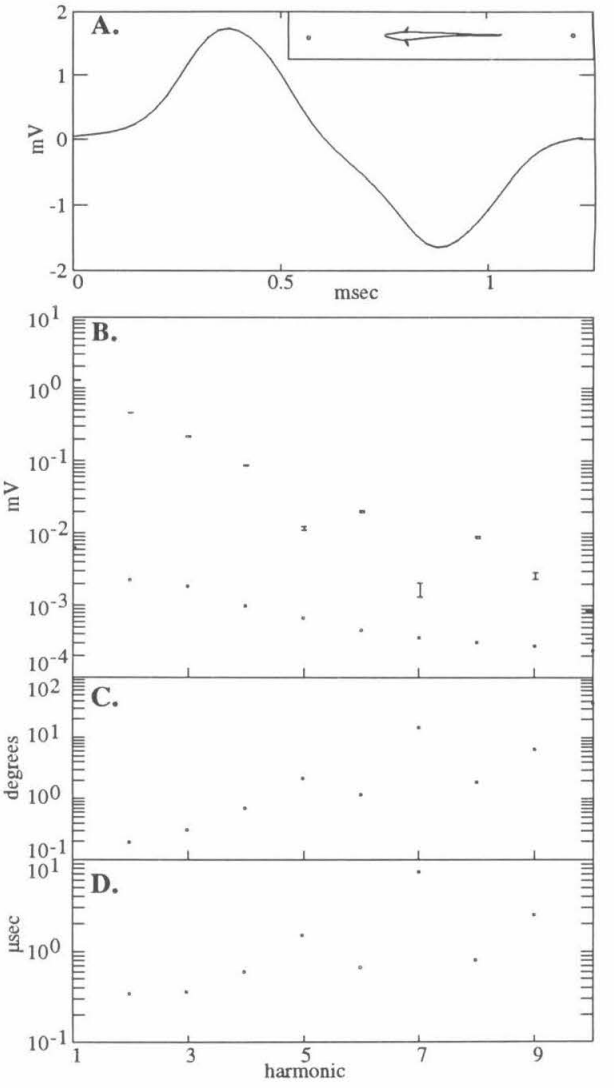

Figure 4.1. A. The phase reference waveform was recorded between two electrodes at opposite ends of the fish (inset). The waveform is the average of 750 measurements over 25 minutes. The standard deviation at 50 phases are shown by vertical errorbars, that are generally less than the line width of the EOD waveform. B. Mean (upper) and standard deviation (errorbars and lower dots) of the harmonic amplitudes. C, D. Standard deviation of the relative phase of each harmonic for the same measurements. Instrumentation noise may dominate the variance of the fifth and higher harmonics.

Electric Field Components

We have decomposed the electric field vector into three components in directions rostral (E_r), lateral (E_l), and dorsal (E_d), relative to the fish. Figure 4.2 shows two periods of the EOD potential and electric field components measured next to the fish's skin, in approximately the midplane. Because of the large dynamic range (e.g., peak voltage and lateral field amplitude at the tail are 15 and 80 times larger than at the mouth), each waveform is normalized, with their relative amplitudes shown by the bars on the right.

Over most of the trunk, the lateral field component is largest, and has similar waveform as the potential. At the fish's head, all electric field components have similar waveforms and phase as the potential. Likewise, at the tip of the fish's tail and in front and behind the fish, the field and potential waveforms have similar shape, except for opposite signs of some field components. For example, behind the fish's tail, at times when the potential is strongly negative, the field is directed headward ($E_r > 0$) and towards the fish ($E_l < 0$).

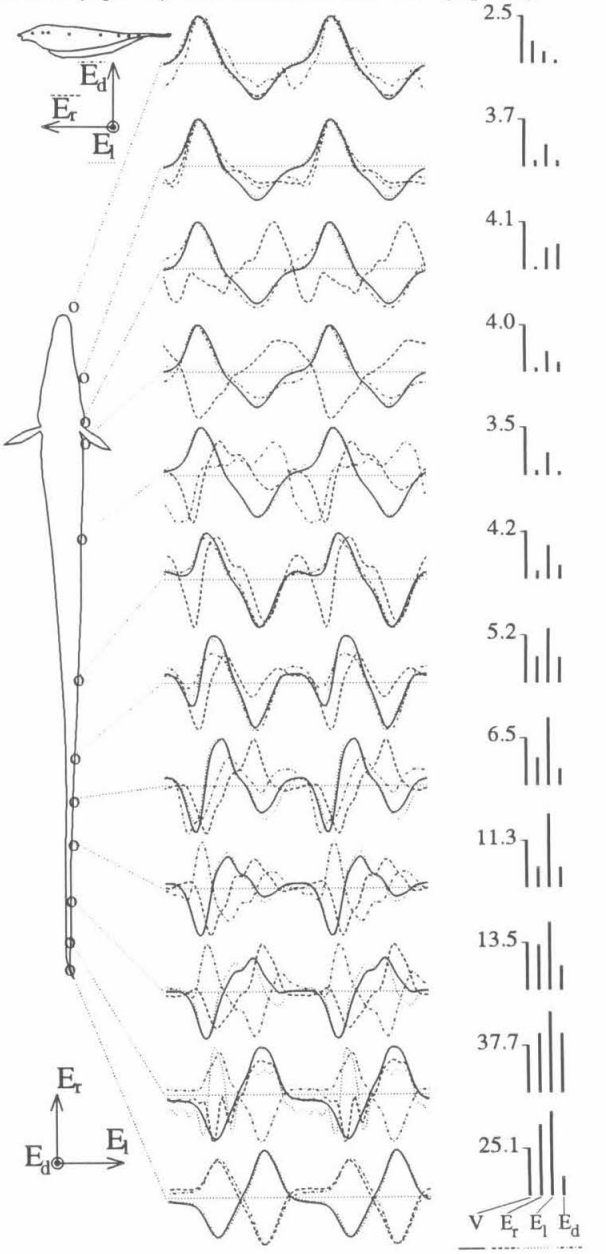

Figure 4.2. Waveforms of the electric potential (solid lines) and three electric field components (broken lines) at points on the surface of *A. leptorhynchus* along the fish's approximate midline. The amplitudes vary considerably with position along the fish, so the waveforms have all been normalized to the same amplitudes. Their relative amplitudes are shown by bars on the right. Units of potential are mV, and the field is in mV/cm.

The EOD slope or slew rate is largest in the narrow part of the fish's tail. Also at the tail and behind it, the plateau near zero amplitude is of longer duration than at the head. This is the result of superposition of the EOD harmonics. In addition to slope, the harmonics affect the number of peaks in the EOD waveforms. Over much of the caudal body, the potential and electric field have large harmonic components. Spectral analysis of the EOD is discussed further below.

We can visualize the dynamics of the field in two spatial dimensions by representing the instantaneous EOD amplitudes in grayscale. In Figure 4.3, the instantaneous potential and field components are shown in the midplane at 13 successive 100 μsec intervals constituting one EOD period. The lateral field is largest and most spatially similar to the potential. A rostral-to-caudal propagation of peaks is evident in the caudal half of the fish. The rostral trunk, in contrast, is more uniform at any particular time, and only near the zero-crossings does E_l have different signs at different locations along the trunk. The locations of the minima of the lateral electric field component (E_l) coincide with minima in the potential map, and peaks in the rostral field (E_r). This is consistent with current flowing from sources at the E_l peaks to sinks at E_l minima. The sign of E_r changes near the operculum, where the rostral component of the normal vector to the fish's body also changes sign. The dorsal field component in the midplane is small, as expected by symmetry.

The potential and field in the dorsoventral plane are shown in Fig. 4.4. Due to symmetry, the lateral component is small, except where measured on the surface of the fish, off the symmetry plane. The dorsal component has opposite signs above and below the fish, consistent with the sign of this component of the vector normal to the fish's body. The head, and in particular, the mouth, is a relatively strong field source (this is less apparent, but also visible in the midplane, Fig. 4.3). Generally, the rostral field component is similar in the two planes. The dorsal component is similar to the midplane lateral component, suggesting the field is approximately radially symmetric.

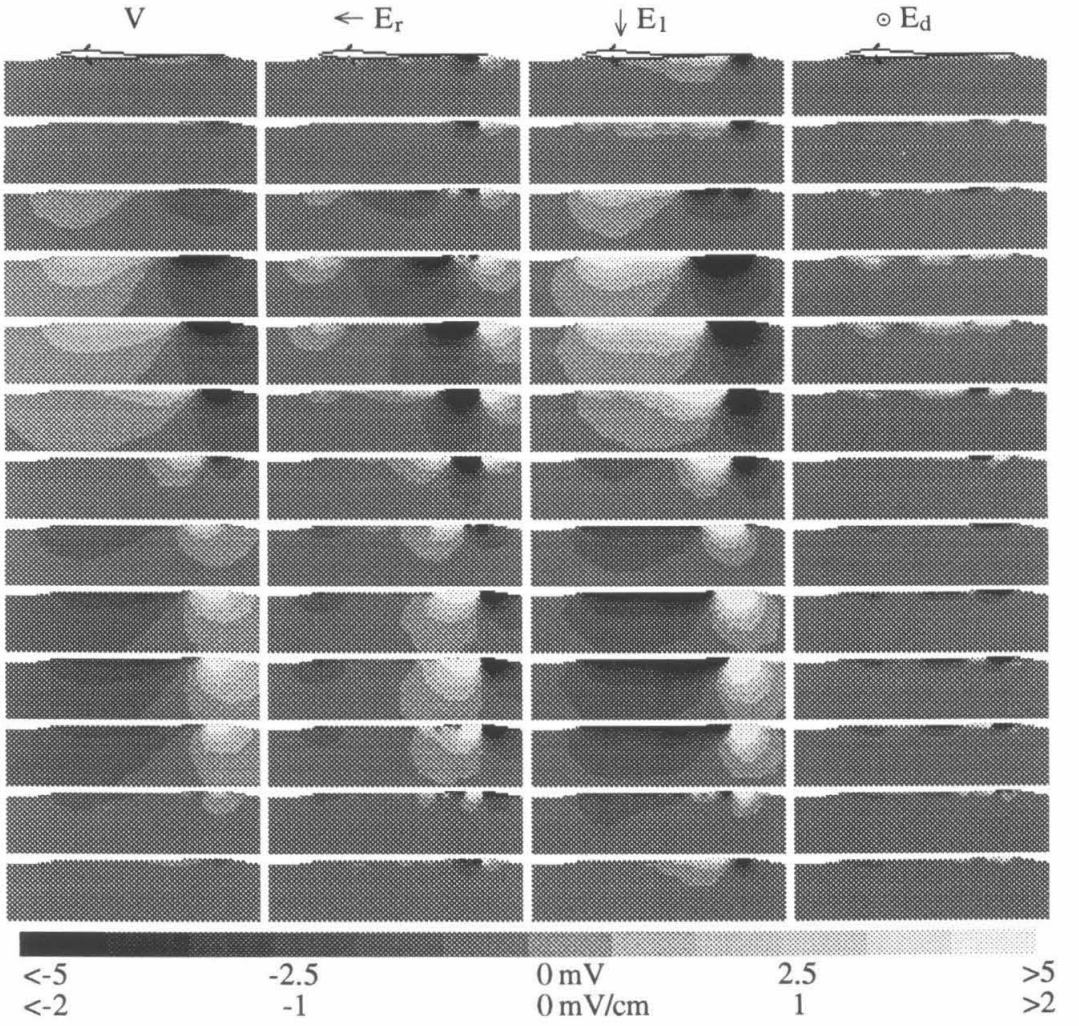

Figure 4.3. Grayscale representation of the potential and field waveforms at 100 μsec intervals over one EOD cycle. Black and white represent potentials and fields less than –5mV and –2 mV/cm, and 5 mV and 2 mV/cm respectively. The top frames are synchronous with the positive slope zero crossing of the potential fundamental, measured in the far field from head to tail.

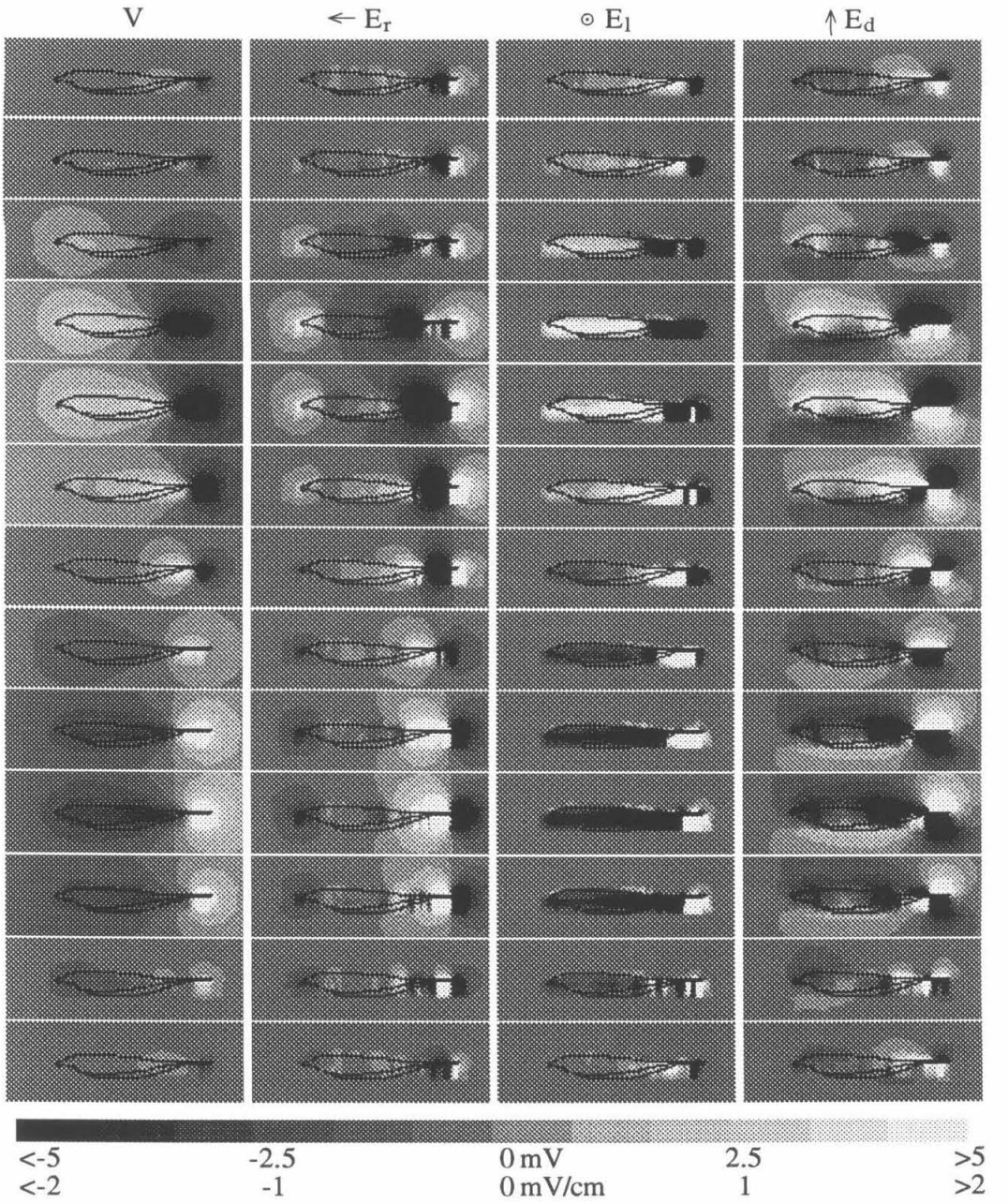

Figure 4.4. Same as Fig. 4.3 in the dorsoventral plane. The potential and field were not measured immediately under the fish's chin or tail, resulting in some interpolation artifacts in these regions.

Spectral Analysis

Figure 4.5 shows the fundamental and lowest frequency harmonic components of the EOD along three lines lateral (in the midplane), dorsal, and ventral of the fish (columns A, B, and C). The 4 rows show amplitudes and phases of the potential and the three perpendicular field components. The potential amplitude (row 1) is largest at the tail, and near the operculum, where the body is thickest and thus closest to the measurement line. The amplitude of the fundamental is relatively uniform over the trunk, and dips at approximately 15 cm from the head. In this region, the second harmonic, which gradually increases amplitude from head to the tail, dominates the EOD, maintaining a more uniform overall (or RMS) amplitude. At the fundamental minimum, the third harmonic exceeds the fundamental, but is still less than half the amplitude of the second harmonic. The amplitude of the third harmonic has a spatial pattern similar to the fundamental, and the second and fourth harmonics are similar to each other. The fifth and higher harmonics (not shown), with frequencies above 4 kHz, have much lower amplitude than the fourth harmonic.

Figure 4.5. (Next page) Spectral analysis of the EOD in the midplane (column 1), above the fish's back (column 2), and below the ventral fin (column 3). The recording sites are shown in two views at the top of each column. The rows show the amplitudes and phase angles of the fundamental and lowest three harmonics of the potential (row 1), and the rostral, lateral, and dorsal electric field components (rows 2-4). Phases for amplitudes less than approximately 5 μV/cm are uncertain and are not shown.

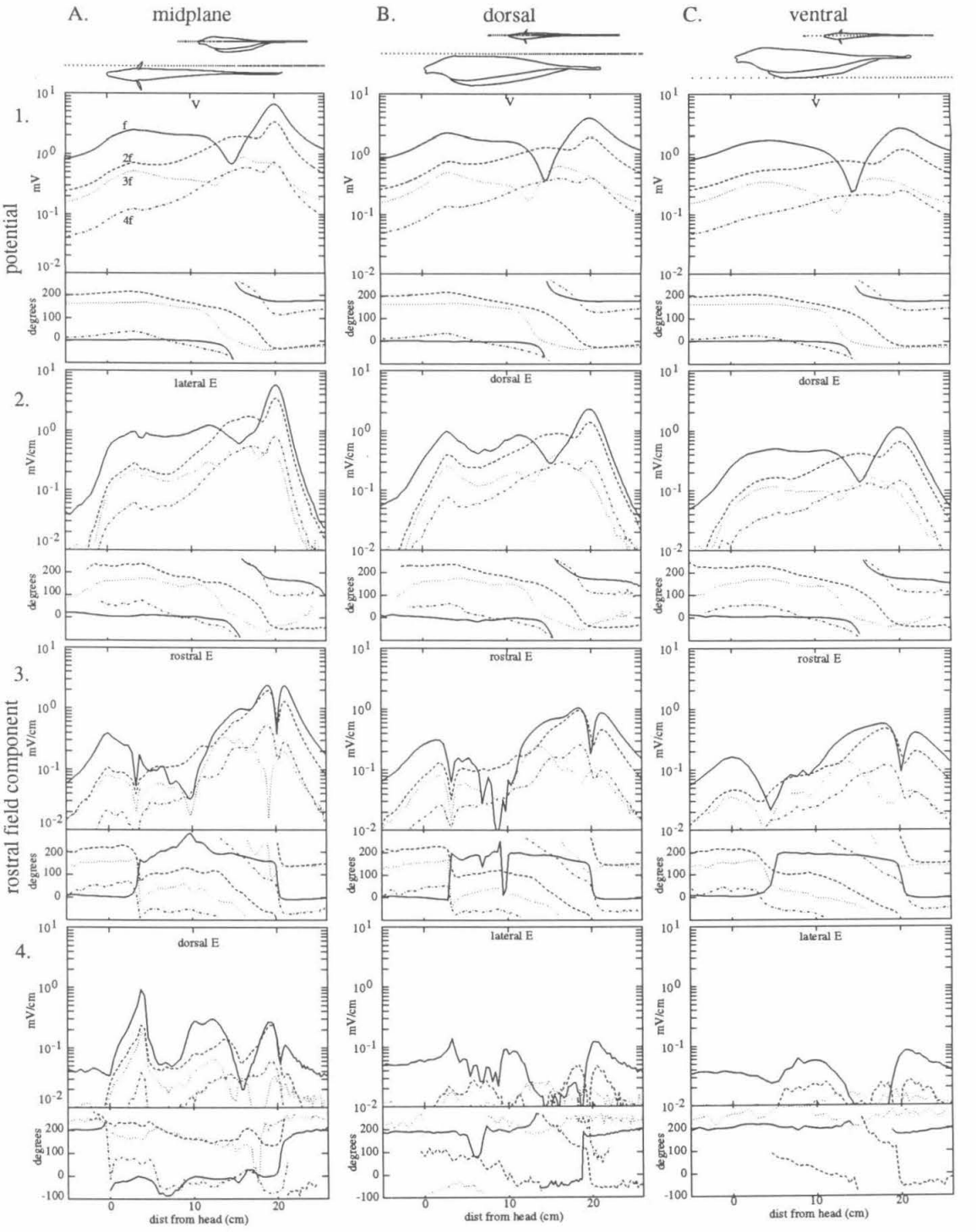
A. midplane
B. dorsal
C. ventral
1.
potential
V
f
2f
3f
4f
mV
degrees
2.
3.
4.
rostral field component
lateral E
dorsal E
rostral E
mV/cm
dist from head (cm)

The phase of the fundamental is nearly constant over the body, and changes abruptly at the amplitude null from approximately 0° to 180°, where it again stays relatively constant beyond the tail. The second and third harmonics are approximately 180° out of phase with the fundamental by the head and tail. This attenuates the initial and final phases of the EOD causing the plateau (Fig. 4.2), and it also steepens and makes more uniform the slope between peaks. The phases of the harmonics change more gradually and over a larger region of the tail than does the fundamental. This results in the rostro-to-caudal temporal propagation of the EOD peaks, which is most apparent caudally, where the harmonics are largest.

The lateral electric field component in the fish's midplane, and dorsal electric field component measured in the dorsal and ventral planes are shown in row 2 of Figure 4.5. Adjacent to the fish's body, this is approximately the radial or normal component of the electric field. The harmonic amplitudes and phases show a pattern similar to the potential over the rostral half of the body. The fundamental is five times larger than the second harmonic, and its phase is nearly constant. At the tail, however, the second harmonic is only slightly weaker than the fundamental. In front of and behind the fish, these electric field components attenuate much more rapidly with distance from the fish than does the potential. In these areas, the fish's normal vector is oriented more rostrally.

The rostral component (row 3) dominates the electric field in front of and behind the fish. It, and thus the electric field vector, decays with distance faster than the potential. Near the middle of the trunk, the fundamental amplitude of E_T drops, and the electric field is directed laterally. Caudal of this area, the second harmonic remains strong, within a factor of two of the fundamental amplitude, to behind the tail. The phase of the fundamental is relatively constant, abruptly changing sign at the operculum and a point at tail. At this caudal point, the amplitude of E_T drops, and E_l is maximum. This is consistent with a point-like current source. In the caudal half of the fish, the phases of the harmonics

of E_r also change more gradually than the fundamental (which has an abrupt transition), causing the propagation seen in Figs. 4.3 and 4.4.

By symmetry, we expect the dorsal electric field component (row 4) in the fish's midplane and the lateral field component in the dorsal and ventral planes to be small. The only deviation is the midplane dorsal component, which has a large peak at the location of the pectoral fin. This peak is colocalized with dips in the lateral and rostral electric field. This suggests that the pectoral fin is directing current to flow dorsally, and parallel with the fin surface.

The Electric Field Vector

Neglecting the small dorsal electric field component in the midplane, we can combine the other field components (E_r, E_l) into 2-dimensional vectors. Figure 4.6A shows the electric field vectors at the same 13 phases as in Figs. 3 and 4, and along the same line as in Fig. 4.5A. There are two stationary peaks, one at the gill area and the other 0.5-1.0 cm from the tip of the tail. Where the second harmonic is larger than the fundamental, the field vector changes sign twice per EOD cycle. For example, around 9 cm from the head, the field vector oscillates rostral and caudal twice per cycle. Further caudal, around 15 cm from the head, E_l changes sign twice per cycle.

Figure 4.6.(Next page) One cycle of the EOD measured along a line (top row) near the fish. At each of these points, the rostral and lateral field components form a 2-dimensional vector, shown at the same 13 phases of the EOD cycle as Fig. 4.3. The vectors have been scaled by 0.2 and 0.05 on the body and tail regions (vertical dotted lines) to accommodate the large dynamic range.

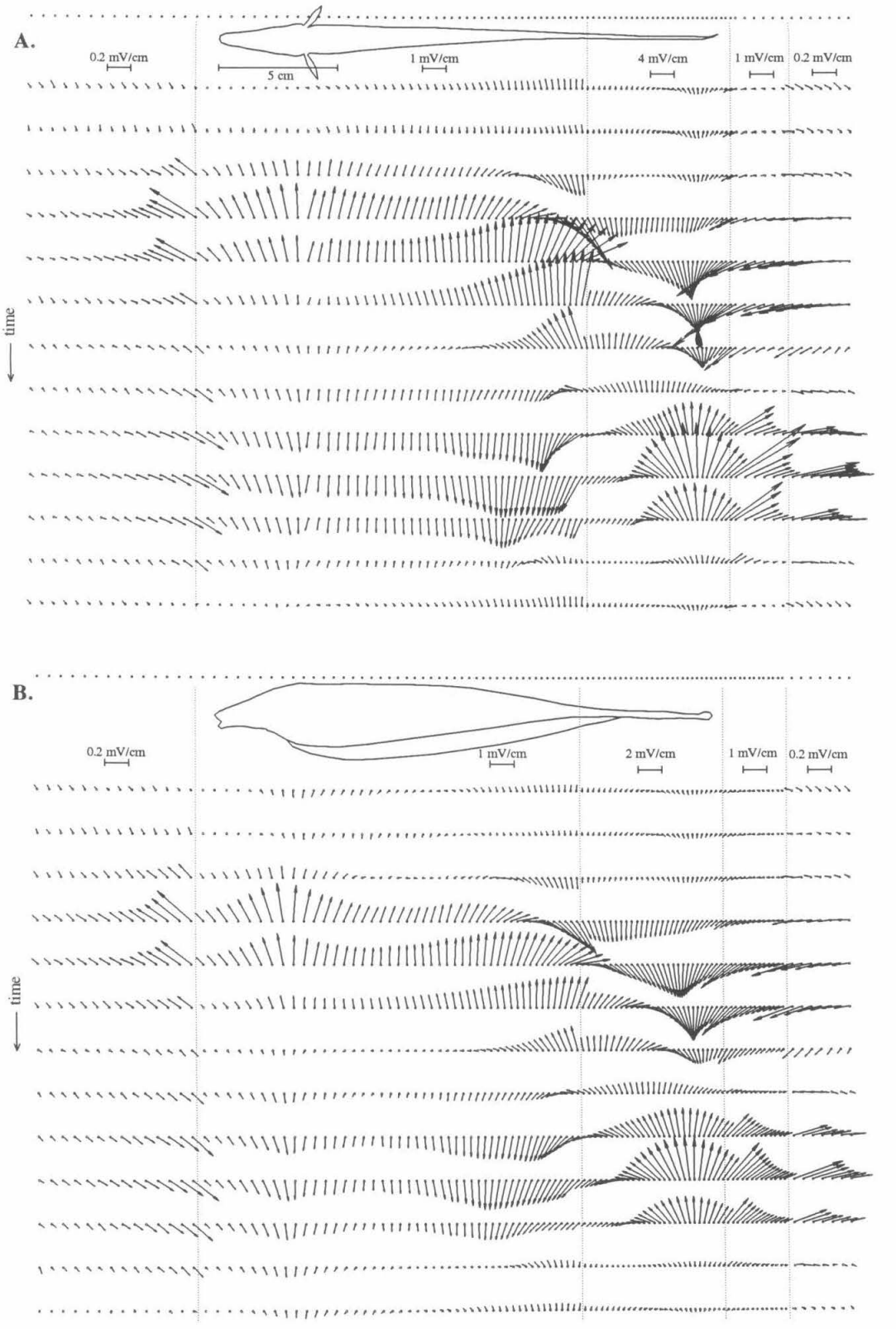
A.
0.2 mV/cm
5 cm
1 mV/cm
4 mV/cm
1 mV/cm
0.2 mV/cm
time
B.
0.2 mV/cm
1 mV/cm
2 mV/cm
1 mV/cm
0.2 mV/cm
time

A notable feature of Fig. 4.6 is that the field vectors in the caudal part of the body change magnitude and direction whereas rostral of the operculum, only the magnitudes and sign, but not the direction, change during the EOD cycle. This is also true away from the fish's body. In Fig. 4.7, we have drawn just the tips of the field vectors as they evolve through the EOD cycle. The figures are left open by omitting the last phases to provide a phase reference, and the entire zero-phase field vector is drawn from the measurement point for orientation. The figures are also normalized to have the same maximum size at each measurement point. In front of the pectoral fin, the field components have the same phase throughout the EOD cycle, but elsewhere, due to harmonics, they are in phase with each other only during part of the cycle. During the first half of the EOD, the field vectors above the middle third of the fish's body sweep counter-clockwise and outward. For the following half of the EOD, the field is directed approximately normal to the fish, and oscillates in amplitude without significant rotation.

Variation Between Fish

All the data presented above are from a single fish. Similar measurements were made on two other *A. leptorhynchus*, and two *A. albifrons*. The major features of the EOD shown here were seen in all fish. Specifically, when normalized for frequency shifts, the EOD waveform was extraordinarily stable for hours. Higher slew rates were observed caudally, and the EOD showed a rostral-to-caudal propagation at the tail. The EOD amplitude peaked slightly at the gill, and strongly near the tip of the tail. The second harmonic always exceeds the fundamental where the phase of the fundamental abruptly shifts. Caudal of this point, the second harmonic remains larger relative to the fundamental. The rotation of the field vector in the caudal body and tail (Fig. 4.7) was strikingly similar in all the *Apteronotus* that we mapped.

The major differences between individual fish were EOD frequency, global amplitude, and the precise locations and detailed pattern of propagation of field peaks

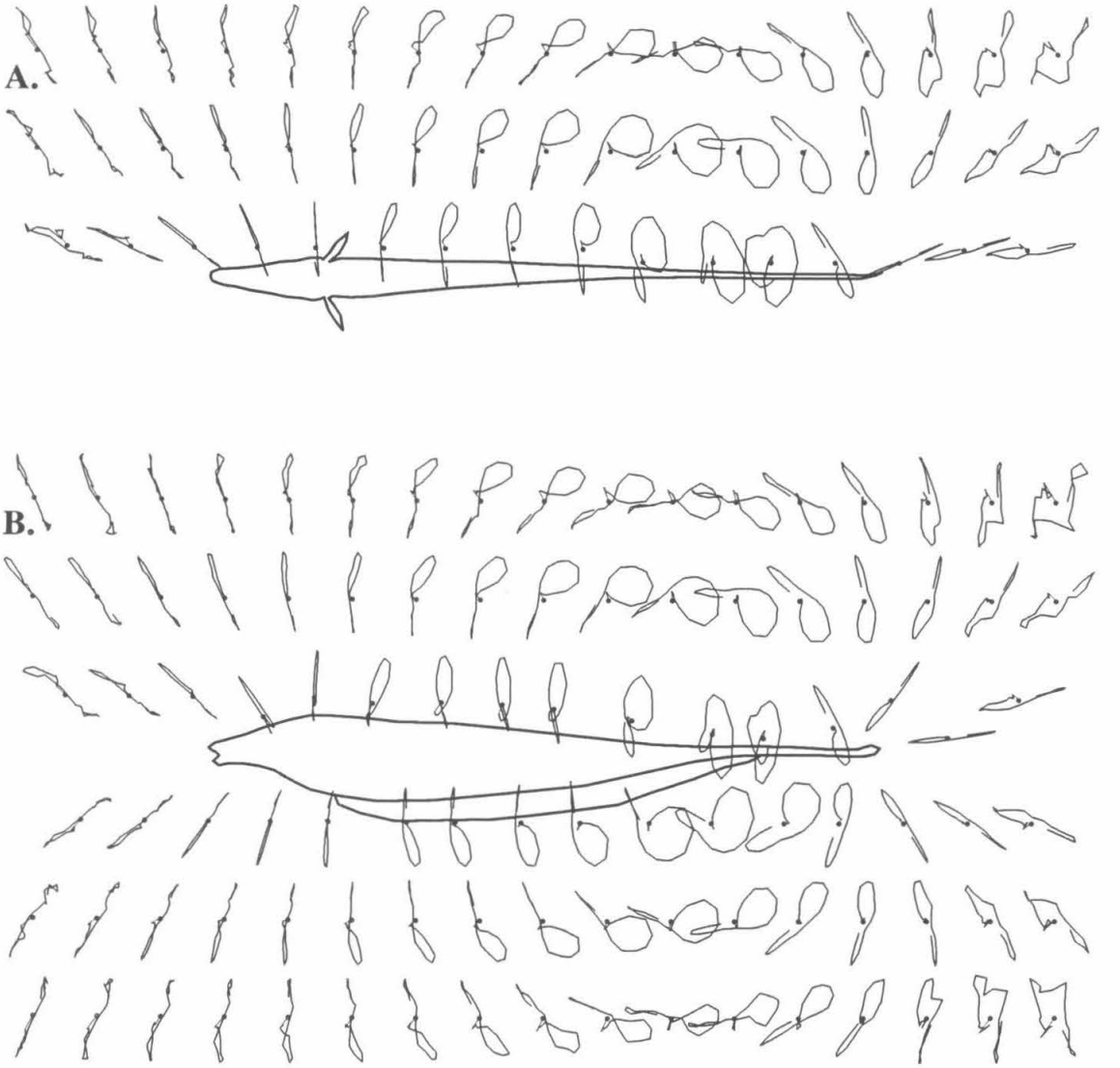

Figure 4.7. Another time domain representation of the EOD cycle, showing the relative rostral and lateral components of the field at several points in the fish's midplane. At each measurement point, the initial EOD phase is drawn as a vector, and for subsequent times, just the tip of the vector is traced. The peak magnitude has been normalized at each point. Over the middle third of the body, the field angle rotates counterclockwise.

[3]. For example, in one *A. albifrons*, the electric field did not significantly rotate over the rostral half of the body, but in most of the fish, the rotation was significant caudal of the pectoral fin. Some other fish had two peaks of the fundamental at the the tail. The more rostral fundamental peak, at the base of the tail, was in phase with the head and most of the trunk. This peak was several times smaller than the more caudal one, which had opposite phase. In spite of the differences in body plan between *A. leptorhynchus* and *A. albifrons*, we did not note any major differences in their respective EOD patterns.

4.4. Discussion

This study is a continuation of our work to thoroughly describe the electric organ discharge of *Apteronotus*. Previously, we presented detailed maps of the electric potential, recorded relative to a distant reference electrode [3]. We refer the reader to that paper for a general discussion. Although the electric potential and electric field are not independent quantities (Eqn. 4.2), studying the electric field reveals new insights into how electric fish may control and use their electric sensory-motor systems.

The electric field vector on the surface and near *Apteronotus* can be measured at high resolution using small electrode arrays. The results near the fish are much more accurate than computing the numerical gradient from a group of potential measurements relative to infinity, or from differential measurements between large electrodes with large separations. The near field of *Apteronotus* is a complicated function of time and space. Over the EOD cycle, the electric field vector varies its magnitude and direction. EOD magnitude varies over several orders of magnitude around the fish. Phase and harmonic composition are also highly dependent on position. Therefore, the electric field is also a challenge to visualize.

Although highly variable with position, the electric field of *Apteronotus* is extremely stable over time scales of at least several hours, and perhaps even months or longer [3]. The data presented here gives only an upper limit of the actual EOD stability

that *Apteronotus* can achieve. Because we measure the EOD in terms of Fourier coefficients, small frequency drifts affect the measured amplitudes. The fish's frequency is extremely sensitive to temperature ($\Delta f \approx 40$ Hz/°C, computed from [9]), and we have also observed a sensitivity to the flow rate of respiration water. We do not know how stable *Apteronotus* may maintain its discharge under natural conditions.

Because the electric field of *Apteronotus* is a complicated function of position, we have described the field in terms of many parameters, e.g., spectral composition, field direction, and decay exponents. It is difficult to quantitatively compare many of these parameters in different fish because of their strong dependence on position around each fish. For example, even comparing the spectral composition of different regions of the fish, as in Fig. 4.5, is complicated by variability in distances between the recording sites and the fish's body. Fig. 4.2 also shows how waveforms change significantly over small regions of the fish's body. For these reasons, we found visual examination of 2-dimensional maps (Figs. 4.3 and 4.4) a more useful approach for comparisons between fish. We have also assembled this data as pseudocolor animations. The data and software to view these animations on color Macintosh computers are available on the internet computer network, by anonymous ftp at mordor.bbb.caltech.edu; cd pub/ElectricFish.

We believe it is significant that the basic properties of the electric field presented here were seen in all the fish that we have studied. Furthermore, the general similarities we have seen in the electric field among our small sample of *A. albifrons* and *A. leptorhynchus* suggests these two species have similar electric organ systems. Since this is a descriptive study, it cannot by itself distinguish functional roles for the various EOD components and parameters. For example, some EOD components may be just incidental artifacts of controlling a long and fast electric organ, and serve no role in facilitating electric sense. However, it is likely that if a parameter is stable and contains useful information about the environment, then there could be a selective advantage for the fish to attend to it. Furthermore, it is well established that electric fish possess the necessary

receptors and elements of the neural circuitry to encode and process amplitude, harmonics, timing and phase, and direction of electric fields.

The electric organ and fish interior

The electric organ and its control circuitry have been the subjects of numerous studies (see [10] and [11] for reviews). Knowing the electric field outside the fish cannot uniquely determine the internal distribution of sources and sinks. However, there are constraints on the continuity of the electric field, and estimates of the impedance of the fish that permit some conclusions about current flow to and from the electric organ (EO). In the water, the electric field and current are proportional, therefore the maps of the field are equivalent to maps of the current vector. These maps support our earlier conclusions that the EO is not globally synchronous. In addition to showing a clear rostro-to-caudal propagation of the peaks and nulls of the electric field components, the electric field maps show that the direction of current flow changes over the EOD cycle in a complicated manner.

Bennett [12] proposed that the skin over the tail channels current to the body and tail tips, thereby increasing the fish's dipole moment. However, Heiligenberg [13] and Hoshimiya [14] found by simulations that the skin impedance at the tail must be low relative to the rest of the body, in order to balance the impedances of the small tail and the much larger body. Our data suggests both these principles operate to some extent. In contrast to the mouth and gills, which act as approximately radial current sources and sinks (consistent with these areas being lower impedance paths to the body interior and EO), current emanates radially from different segments of the tail during different phases of the EOD cycle. It is unlikely that this is due to low impedance pathways selectively channeling current through the skin, for these would somehow have to change with EOD phase. More likely, this pattern reflects sequential activity of the underlying segments of

the EO. This implies that the skin at the tail does not severely impede the current from the underlying EO segments, as proposed by Bennett.

In some of the fish that we studied, the EOD amplitude had two peaks at the base and end of the tail. This suggests that some current channeling is occurring. Based only on our data outside the fish, it cannot be determined whether this is due to the fish's skin and/or other internal structures, such as the membranes surrounding the electric organ [12]. Additional leakage current through the skin between these peaks was always evident in all fish.

Boundary conditions require that the tangential component of the electric field is continuous at the interface between the fish's skin and the water. Caudal of the gill, the tangential electric field is nonzero during certain phases of the EOD. Therefore there must be tangential currents within the skin. Although physically thin, the relatively high impedance of the fish's skin confers it a large effect on the current flow from the EO. We have measured the impedance of bulk patches of excised skin on the trunk of another *Apteronotus* to be approximately 3 $k\Omega\text{-}cm^2$, and primarily ohmic (unpublished measurements). It is therefore unlikely that the fish's interior could be equipotential, which implies a normal electric field on the inside boundary of the skin, that is subsequently redirected within the skin. More likely, the body is not equipotential, and contains tangential currents as well. In support of this, we measured a bulk body impedance of 300 Ω-cm in the rostrocaudal direction. We also measured in live fish potential differences of 0.5 mV RMS between electrodes inside the fish's body within approximately 3 cm of each other. The transdermal potential nearby was 0.7 mV RMS. Internal potential drops may therefore complicate direct measurement of transdermal potentials. However, since one is often interested in changes in transdermal potentials (e.g., due to nearby objects), this effect should be much smaller.

Electroreceptors

Like other weakly electric fish, *Apteronotus* has two types of electroreceptors that detect its own EOD [15]. Amplitude and phase are encoded by P and T receptors respectively, although P units also encode phase [16], [17], and there is evidence that this rigid classification may be oversimplified [18]. Although P-receptors in *Apteronotus* are primarily tuned to the EOD fundamental, they show a second tuning peak at the second harmonic [19]. Behavioral thresholds to external fields also show higher sensitivity to the second harmonic [20]. In the caudal part of the fish, the second harmonic of the field is closer in amplitude to the fundamental than the corresponding spectral components of the potential. Therefore, the second harmonic may have even larger sensory significance than is suggested by the potential spectra.

The second and higher harmonics are generally of the appropriate phase to increase the slope or slew rate of the EOD. This could improve the temporal acuity of the T-receptors, which encode the timing of zero-crossings [17]. The positive and negative slope zero crossings are not symmetrical, and in much of the fish, have significantly different slope (Fig. 4.2). The negative slope zero crossing on the body, which corresponds to the beginning of inward current flow, is the steepest phase of the EOD over most of the body, and would be most immune to noise.

Fleishman [21] claims that T-units in *Sternopygus* encode the positive slope zero crossing of the EOD. However, we suggest that this result may be erroneous due to their stimulus geometry. For these experiments, the fish's own EOD was silenced and an electric field was supplied with external electrodes. This reverses the direction of current flow through the skin, because the fish's interior is now of lower potential than the outside, for it is further from the current sources. T-units have not been adequately studied in *Apteronotus*, in part because they are relatively rare, constituting approximately 10 percent of the electroreceptors [19].

Yager and Hopkins [22] recently showed that electroreceptors in *Hypopomus* are selective to the electric field direction. Behavioral studies had previously demonstrated that electric fish follow the direction of applied electric fields [23], [24]. The electric field direction is therefore another parameter that, in addition to phase and amplitude, contains useful sensory information, which the fish attends to. Because the direction of the field changes with position and EOD phase (Fig. 4.7), it could conceivably help in resolving electric images that, based on amplitude information alone, might be ambiguous between different sets of positional and conductivity parameters. It is notable that many of the receptors in *Hypopomus* preferred field directions that were not normal to the fish's skin. It is not known whether electroreceptors in *Apteronotus* have similar directional sensitivity, or polarity preferences [25].

Signals from electroreceptors near the gill are contaminated with a large modulation associated with the fish's respiration [3]. Our data suggests there is another self-modulation of the electric field in this body region due to the fish's pectoral fin (Fig. 4.5A4). Electric fish apparently cope with this, for they have numerous electroreceptors in this region [27], [28]. Montgomery and Bodznick [26] have elaborated much of the neural circuitry involved in the suppression of ventilatory signals in the skate.

Electrolocation

The rate of decay of the electric field with distance from the fish is a major determinant of the range of electrolocation (Fig. 4.8). The attenuation does not follow a simple power law, which is not surprising given the complex and dynamic distribution of current sources and multipoles within the fish. Near the fish, the field decays slowly because the body acts as a 2-dimensional surface of current sources, and therefore the current only slightly diverges. Further away, the body and tail act approximately as linear or 1-dimensional sources. Figure 4.5 provides an estimate of the length of these sources: 15 cm for the body and a few cm for the tail. At distances of the order of their length, the

decay rate increases towards that of a point source. At distances comparable to the fish's length, the field is dipolar, and already too weak for small objects to be detectable [29]. The near field decays faster at the tail than at the head for a given distance from the fish because the tail is smaller than the trunk. The potential attenuates fastest between the trunk and tail poles, where dipole effects first appear.

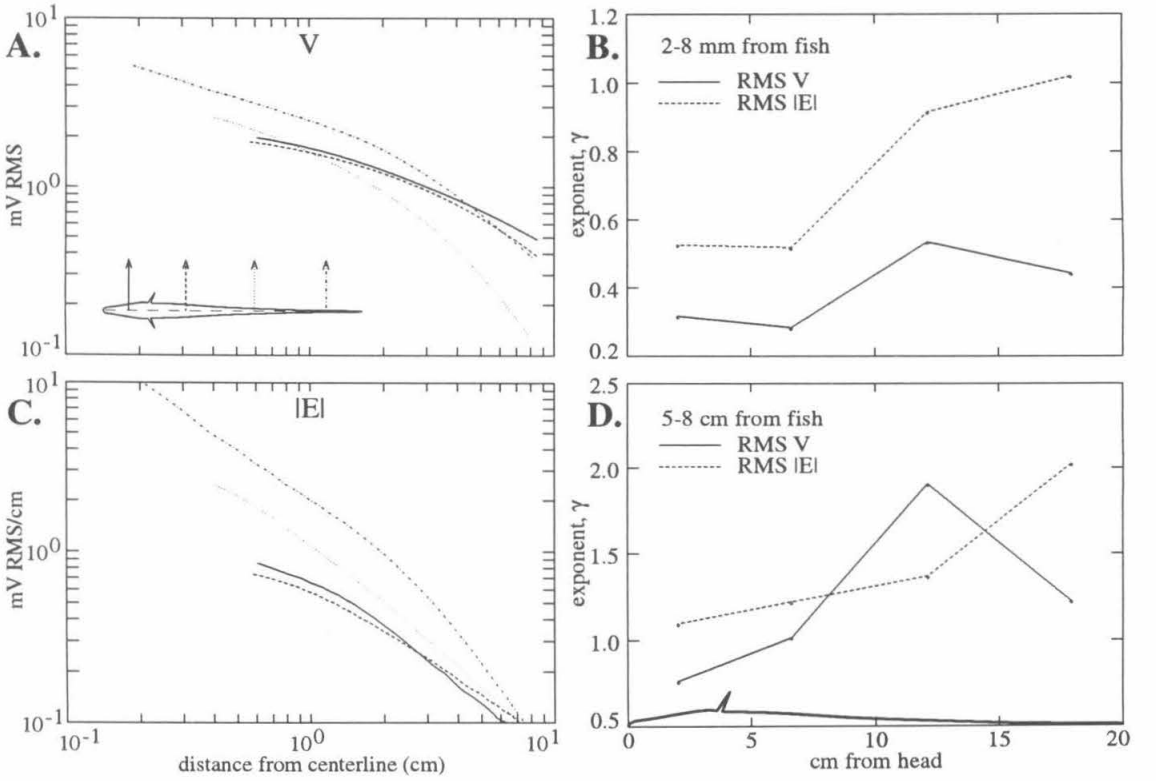

Figure 4.8. The RMS potential (A) and electric field magnitudes (C) are shown as a function of distance from the fish's centerline (the rostrocaudal axis in the midplane). Fitting sections of these graphs to a power law: $y \propto x^{-\gamma}$, for distances between 2 and 8 mm (B) and 5–8 cm (D) from the fish's skin, the power γ increases from head to tail. The potential attenuates fastest near the null of the dipole.

In our previous study of the *Apteronotus* potential, we proposed that there may be differences in the fish's perception of objects along its rostrocaudal axis. At the fish's head, the electric field is most uniform in amplitude, phase, harmonic composition, and direction. Thus any inhomogeneous electrical structure of an object near the head would not be confounded with inhomogeneity in the fish's field. Also the electric images would be more stable to relative motion between the object and fish. In addition, because the electric field is perpendicular to the skin, the electric images may have higher spatial resolution (see Chapter 5). In the caudal part of the fish, the field is stronger near the fish, more spatially variable, and attenuates more rapidly with distance. Therefore the electric image of an object would be strongly modulated by changes in distance and position, as would occur for example, as the fish moves its tail.

The rotating caudal field would almost certainly add spatiotemporal features to the electric images of objects. An object's induced dipole moment is proportional to the electric field vector, and will thus rotate at the same rate. However, nonspherical objects could have different dipole moments in different field orientations, qualitatively analogous to them casting different shadows in different orientations relative to the illumination angle. Therefore, the fish may attain multiple perspectives of an object by its rotating electric field.

There are yet additional factors that would tend to increase the complexity and spatiotemporal information content of images of caudal objects. A dielectric object's image could also be phase shifted, and therefore the instantaneous dipole moment of the perturbation would have different orientation than the field. We have shown that harmonics make a significant contribution to the caudal field (Fig. 4.5). For dielectrics, both the magnitude and phase of the perturbation field will be different for each harmonic, which could result in complex changes in the EOD waveform and its timing. The larger spatial gradient of the caudal electric field could also generate stronger multipole moments.

Which of the features of the fish's electric field described here may be used by electric fish to identify object characteristics, and which may even confound object images, is still unknown. The rostrocaudal differences in the electric field suggest that there should also be rostrocaudal differences in the activity of electroreceptors and higher order neurons. Such differences, if indeed they are found, could provide clues about the functional roles of these electric field properties. It is especially difficult to infer additional significance to the rotating field without a better understanding of electroreceptor transfer functions, which have their own directional asymmetries [25]. We hope this description of the electric field will stimulate additional research in these directions.

Detection by other electric fish

Electric fish use their electric fields for communication and identification of other electric fish in addition to passive object detection. We next explore some ramifications of the electric field's structure on these tasks.

The dorsoventral and midplane fields are highly similar suggesting approximate radial symmetry of the *Apteronotus* field. In Fig. 4.5, the largest variations between the midplane, dorsal, and ventral maps are probably due to the measurements being different distances from the fish's skin. For example, the potential and field at the tail is largest in the midplane map and smallest in the ventral map, inversely related to the distance between the fish and measurement points. Although the fish's body is laterally flattened, this does not seem to strongly affect the electric field. In other species, such as *Eigenmannia* and *Gymnotus*, we do see larger differences in the field on the dorsal and ventral body. However, these asymmetries strongly correlate with the location of the electric organ, which in these species, is not on the fish's midline. In contrast, the EO of *Apteronotus* lies close to the fish's midline.

A radially symmetric field may benefit *Apteronotus* because of this fish's propensity to swim on its side and rotate about its rostrocaudal axis. Whereas a lack of

radial symmetry would have little effect on electrolocation, since the electroreceptors would also rotate with the field, it could have profound consequences on the field detected by nearby fish. It has been demonstrated that some species of weakly electric fish can recognize individual conspecifics solely on the spectral and spatial characteristics of their EODs [30], [31]. In our previous study of the potential, we suggested that *Apteronotus* may also possess this ability. A radially symmetric field could facilitate the identification of conspecifics from electric field cues.

Both genera of weakly electric pulse fish have been shown to approach other electric sources by swimming parallel to the electric field lines [24], [23]. The fish rely primarily on the direction of the field, and not its amplitude, to find the source. The tangential components of a fish's field are significant in these encounters, for these components may impinge on another fish along the preferred orientation of the fish's electroreceptors. In the wild, many of the interactions between electric fish are of a predatory nature or in defense of territory [32]. It is interesting to speculate if the rotating field vector in the caudal body might benefit *Apteronotus* by confusing an electroreceptive predator attempting to follow its field lines. It is possible that upon entering the complex near field, a predator might pause or makes an abrupt correction to its trajectory. Such movements could be detected by the lateral line sense, and trigger an escape response. These results suggest a number of behavioral experiments, which we hope will be pursued.

References

[1] Bullock, T.H. and Heiligenberg, W., *Electroreception*, John Wiley & Sons, Inc., 1986.

[2] Rasnow, B., Assad, C., Nelson, M.E., and Bower, J.M., "Simulation and Measurement of the Electric Fields Generated by Weakly Electric Fish," in *Advances in Neural Information Processing Systems 1*, Touretzky, D.S. (Ed.), pp. 436-443, Morgan Kaufmann, 1989.

[3] Rasnow, B., Assad, C., and Bower, J.M., "Phase and Amplitude Maps of the Electric Organ Discharge of the Weakly Electric Fish, Apteronotus leptorhynchus," *J. Comp. Physiol.*, **172**:481-491, 1993.

[4] Robinson, D.A., "The Electrical Properties of Metal Microelectrodes," *Proc. IEEE*, **56**:1065-1071, 1968.

[5] Horowitz, P. and Hill, W., *The Art of Electronics*, 2nd Edition, Cambridge University Press, 1989.

[6] Dennis, J.E.J. and Woods, D.J., *New Computing Environments: Microcomputers in Large-Scale Computing*. SIAM, 1987, pp. 116-122.

[7] Jackson, J.D., *Classical Electrodynamics*, Wiley & Sons, 1975.

[8] Bloomfield, P., *Fourier Analysis of Time Series: An Introduction*, John Wiley & Sons, 1976.

[9] Enger, P.S. and Szabo, T., "Effect of Temperature on the Discharge Rates of the Electric Organ of some Gymnotids," *Comp. Biochem. Physiol.*, **27**:625-626, 1968.

[10] Bass, A.H., "Electric Organs Revisited: Evolution of a Vertebrate Communication and Orientation Organ," in *Electroreception*, Bullock, T.H. and Heiligenberg, W. (Eds.), pp. 13-70, Wiley, 1986.

[11] Dye, J.C. and Meyer, J.H., "Central Control of the Electric Organ Discharge in Weakly Electric Fish," in *Electroreception*, Bullock, T.H. and Heiligenberg, W. (Eds.), pp. 71-102, Wiley, 1986.

[12] Bennett, M.V.L., "Electric Organs," in *Fish Physiology*, Hoar, W.S. and H., R.D. (Eds.), pp. 347-491, Academic Press, 1971.

[13] Heiligenberg, W., "Theoretical and Experimental Approaches to Spatial Aspects of Electrolocation," *J. Comp. Physiol.*, **103**:247-272, 1975.

[14] Hoshimiya, N., Shogen, K., Matsuo, T., and Chichibu, S., "The *Apteronotus* EOD Field: Waveform and EOD Field Simulation," *J. Comp. Physiol.*, **135**:283-290, 1980.

[15] Scheich, H. and Bullock, T.H., "The Detection of Electric Fields from Electric Organs," in *Handbook of Sensory Physiology*, Fessard, A. (Ed.), pp. 201-256, Springer-Verlag, 1974.

[16] Bastian, J., "Electrolocation I. How the Electroreceptors of *Apteronotus albifrons* Code for Moving Objects and Other Electrical Stimuli," *J. Comp. Physiol.*, **144**:465-479, 1981.

[17] Scheich, H., Bullock, T.H., and Hamstra, R.H., "Coding Properties of Two Classes of Afferent Nerve Fibers: High-Frequency Electroreceptors in the Electric Fish, *Eigenmannia*," *J. Neurophys.*, **36**:39-60, 1973.

[18] Viancour, T.A., "Electroreceptors of a Weakly Electric Fish. I. Characterization of Tuberous Receptor Organ Tuning," *J. Comp. Physiol.*, **133**:317-325, 1979.

[19] Hopkins, C.D., "Stimulus Filtering and Electroreception: Tuberous Electroreceptors in Three Species of Gymnotid Fish," *J. Comp. Physiol.*, **111**:171-207, 1976.

[20] Knudsen, E.I., "Behavioral Thresholds to Electric Signals in High Frequency Electric Fish," *J. Comp. Physiol.*, **91**:333-353, 1974.

[21] Fleishman, L.J., "Communication in the Weakly Electric Fish *Sternopygus* marurus I. The Neural Basis of Conspecific EOD Detection," *J. Comp. Physiol.*, **170**:335-348, 1992.

[22] Yager, D.D. and Hopkins, C.D., "Directional Characteristics of Tuberous Electroreceptors in the Weakly Electric Fish, Hypopomus (Gymnotifromes)," *J. Comp. Physiol.*, **173**:401-414, 1993.

[23] Schluger, J.H. and Hopkins, C.D., "Electric Fish Approach Stationary Signal Sources by Following Electric Current Lines," *J. Exp. Biol.*, **130**:359-367, 1987.

[24] Davis, E.A. and Hopkins, C.D., "Behavioral Analysis of Electric Signal Localization in the Electric Fish, *Gymnotus carapo* (Gymnotiformes)," *Anim. Behav.*, **36**:1658-1671, 1988.

[25] McKibben, J.R., Hopkins, C.D., and Yager, D.D., "Directional Sensitivity of Tuberous Electroreceptors: Polarity Preferences and Frequency Tuning," *J. Comp. Physiol.*, **173**:415-424, 1993.

[26] Montgomery, J.C. and Bodznick, D., "Hindbrain Circuitry Mediating Common Mode Suppression of Ventilatory Reafference in the Electrosensory System of the Little Skate, *Raja erinacea*," *J. Exp. Biol.*, **183**:203-215, 1993.

[27] Carr, C.E., Maler, L., and Sas, E., "Peripheral Organization and Central Projections of the Electrosensory Nerves in Gymnotiform Fish," *J. Comp. Neurol.*, **211**:139-153, 1982.

[28] Bennett, M.V.L., "Electroreception," in *Fish Physiology*, Hoar, W.S. and H., R.D. (Eds.), pp. 493-574, Academic Press, 1971.

[29] Knudsen, E., "Spatial Aspects of the Electric Fields Generated by Weakly Electric Fish," *J. Comp. Physiol.*, **99**:103-118, 1975.

[30] McGreggor, P.K. and Max Westby, G.W., "Discrimination of Individually Characteristic Electric Organ Discharges by a Weakly Electric Fish," *Anim. Behav.*, **43**:977-986, 1992.

[31] Kramer, B. and Otto, B., "Waveform Discrimination in the Electric Fish Eigenmannia: Sensitivity for the Phase Differences Between the Spectral Components of a Stimulus Wave," *J. Exp. Biol.*, **159**:1-22.

[32] Max Westby, G.W., "The Ecology, Discharge Diversity and Predatory Behavior of Gymnotiforme Electric Fish in the Costal Streams of French Guiana," *Behav. Ecol. Sociobiol.*, **22**:341-354, 1988.

Chapter 5
The Effects of Simple Objects on the Electric Field of *Apteronotus*

5.1. Introduction

Several diverse groups of animals possess sensory systems specialized for the detection of weak electric fields [1]. Electric fields permeate aquatic environments, arising from neuronal and muscle activity, and even the motion of the animal in the geomagnetic field [2]. Two families of freshwater fish have extended their electric sense to detect electrically passive objects. These fish have electric organs that generate a stable high frequency electric field [3], which is modulated by nearby objects with different impedance than the surrounding water [4]. In addition to their electric field generator organ, weakly electric fish have thousands of receptor organs in their skin, that are tuned and exquisitely sensitive to modulations in their electric organ discharge (EOD) [5].

In the previous chapters, we presented high spatial and temporal resolution maps of the electric field generated by the weakly electric fish, *Apteronotus*. Here we explore how the fish's electric field is modulated or perturbed by objects, and how the fish may detect these perturbations. Consider a small spherical object at some distance from the fish. The fish's electric field induces a surface charge distribution on the sphere, resulting in a dipolar perturbation superimposed on the fish's electric field. The fish detects this perturbation with an array of electroreceptor organs within its skin. The pattern of the perturbation on the skin constitutes an "electric image" of the object.

In this chapter, we present images of objects derived from two complementary methods. Using small, flexible electrodes placed on the fish's skin, we directly measured the electric potential while a metal sphere was positioned in various locations. The perturbation is computed as the difference between the potential at the fish's skin with and

without the object present. A second approach we have taken is to simulate electric images of small objects. These simulations were based on previous measurements of the electric field vector in the absence of objects (see Chapter 4), combined with an analytic model of the object. Being analytic, the simulations provide additional insight into the parameters that affect electric images and their functional dependencies. However, because the simulations depend on certain assumptions and idealizations, they cannot be expected to replicate exactly the electric images of actual objects. A goal of this study is to quantify the accuracy and limitations of this simulator.

An electric image can be described as either a modulation of the electric field or the electric potential at the fish's skin. The fish's electroreceptor organs most likely respond to the potential across their active membranes [6]. An nearby object will likely have greater effect on the potential outside a fish than internally, because the high impedance of the fish's skin relative to the interior acts as a voltage divider, dropping most of the perturbation voltage over the skin. Therefore, to a first-order approximation, the electric image of a nearby object can be described by the change in potential on the skin surface due to the object's presence. Only potential perturbations were measured on the fish's skin, however the simulator can compute changes in both potential and current.

Objects modulate both the EOD amplitude and phase. Electric fish are sensitive to both these parameters, and have separate receptor organs and neural pathways specialized for processing each component [7], [8]. In this study, we focus on the input to the amplitude coding receptors or P-units. These receptors modulate their probability of firing (which is < 1 per cycle) as a function of EOD amplitude. Precisely how the EOD signal is rectified and integrated by these receptors is still being investigated [9], [10]. For this reason, we assume a simple transfer function for the receptors: the change in root-mean-square (RMS) amplitude. Our conclusions do not depend on the detailed functional form of the transfer function.

5.2. Methods

Subject

This experiment was conducted on the same individual *A. leptorhynchus*, and during the same recording session as described in Chapter 4. The recording and analysis methods are the same as described there.

Measurements of electric images

The potential on the fish's skin was measured with a flexible linear array of five silver ball electrodes approximately 5 mm apart. Each electrode was insulated to its tip, which was approximately a 200 μm diameter sphere. Potentials were measured relative to a 1 mm diameter silver ball electrode mounted on the tank wall 30 cm lateral of the fish. Because the object was opaque, the following sequence was used to position the object over the electrode array. The electrodes were placed on the fish's approximate midline and their locations were recorded by a video camera viewing the fish from its side. The array was then removed and the object, a 2.2 cm diameter brass sphere coupled to a manipulator, was placed in contact with the skin to calibrate its lateral distance. The object was moved 2 mm away and the electrode array was repositioned against the skin. Although every effort was made to reposition the electrodes in their previous positions, errors on the order of 1 mm were not unlikely. Measurements were taken as the object was stepped away from the fish. The sequence of object distances was repeated twice at three locations along the fish's rostro-caudal axis, and once at a more caudal location.

Simulations of electric images

A conducting sphere of radius a placed in a uniform electric field $\mathbf{E}_0$ generates a purely dipolar potential proportional to the field. For the simulations presented here, we assumed the electric field was uniform and equal to the measured value at the object's

center (before placing the object there). At a position **r** from the object, the perturbation is given by (see Appendix 1 for derivation):

$$\delta\varphi(\mathbf{r}) = \mathbf{E}_0 \cdot \mathbf{r}\left(\frac{a}{r}\right)^3 \frac{\rho_1 - \rho_2 + i\omega\rho_1\rho_2(\varepsilon_2 - \varepsilon_1)}{2\rho_2 + \rho_1 + i\omega\rho_1\rho_2(2\varepsilon_1 + \varepsilon_2)} \qquad (5.1)$$

where ρ_1 = 5 kΩ-cm is the conductivity of the water; $\varepsilon_1 = 80\varepsilon_0 \cong 7.1$ pF/cm is the dielectric constant of water; ρ_2 and ε_2 are the conductivity and dielectric strength of the sphere of radius *a*; $\omega = 2\pi f$ is the angular frequency of the unperturbed electric field, $\mathbf{E}_0$; and $i = \sqrt{-1}$. The simulation can be run independently for each EOD harmonic and the results superposed.

For a perfect conductor ($\rho_2 = 0$), Eqn. 5.1 simplifies to:

$$\delta\varphi(\mathbf{r}) = \frac{a^3\mathbf{E}_0 \cdot \mathbf{r}}{r^3}. \qquad (5.2)$$

For insulators such as plexiglass or quartz, with $\rho_2 >> \rho_1$ and $\varepsilon_2 \leq \varepsilon_1$, it reduces to:

$$\delta\varphi(\mathbf{r}) = -\frac{a^3\mathbf{E}_0 \cdot \mathbf{r}}{2r^3}. \qquad (5.3)$$

The electric field vector, $\mathbf{E}_0$, was measured in the fish's midplane as described in Chapter 4. The electric field at selected object points was interpolated from the measured $\mathbf{E}_0$. The fish's body was outlined in the same experiment, which defined the set $\{\mathbf{r}\}$ of field points for the simulations.

5.3. Results

Waveforms of object perturbations

Figure 5.1 shows the effect of a brass sphere on the EOD potential waveform recorded between the fish's skin directly below the object and a distant electrode. The EOD waveforms are shown in rows 1 and 3 as the center of a 11 mm sphere moved from 13–43 mm lateral of the fish's skin (skin to object-center distance) at four rostro-caudal positions (A-D, see insets). The lowest amplitudes correspond to the object nearest the fish (conducting objects reduce the EOD amplitude on the fish's skin). The second and fourth rows show the object modulations, computed by subtracting the potential with the

object present from the potential without the object. Even at its nearest distance, where the edge of the 22 mm diameter sphere was a mere 2 mm from the fish's skin, the EOD amplitude was reduced by less than 15 percent.

Some distinctive features of these electric images are that the object does not simply perturb the EOD potential by a multiplicative factor. In all four rostrocaudal positions, certain phases are more perturbed than others. Certain phases in the EOD cycle have invariant (and nonzero) amplitude with respect to object distance. The relative amplitudes of the double peaks and the potential perturbation at Fig. 5.2D are also opposite each other. To understand what may cause such nonlinear modulations, we examined the electric field without the object, in the space where the object was placed. It is expected on theoretical grounds (see below and Methods) that the perturbation directly below the object should be proportional to the lateral electric field at the object. We next use the simulator to quantitatively compare the measured potential changes on the fish's skin with the electric field at the object.

Figure 5.1. (Next page) A conducting sphere decreases the EOD potential measured between the fish's skin below it and a distant electrode. The potential waveforms and the change in potential due to the object are shown at four rostrocaudal positions (A-D) for seven object-fish distances (insets). The perturbation is not a simple multiplication of the potential waveform.

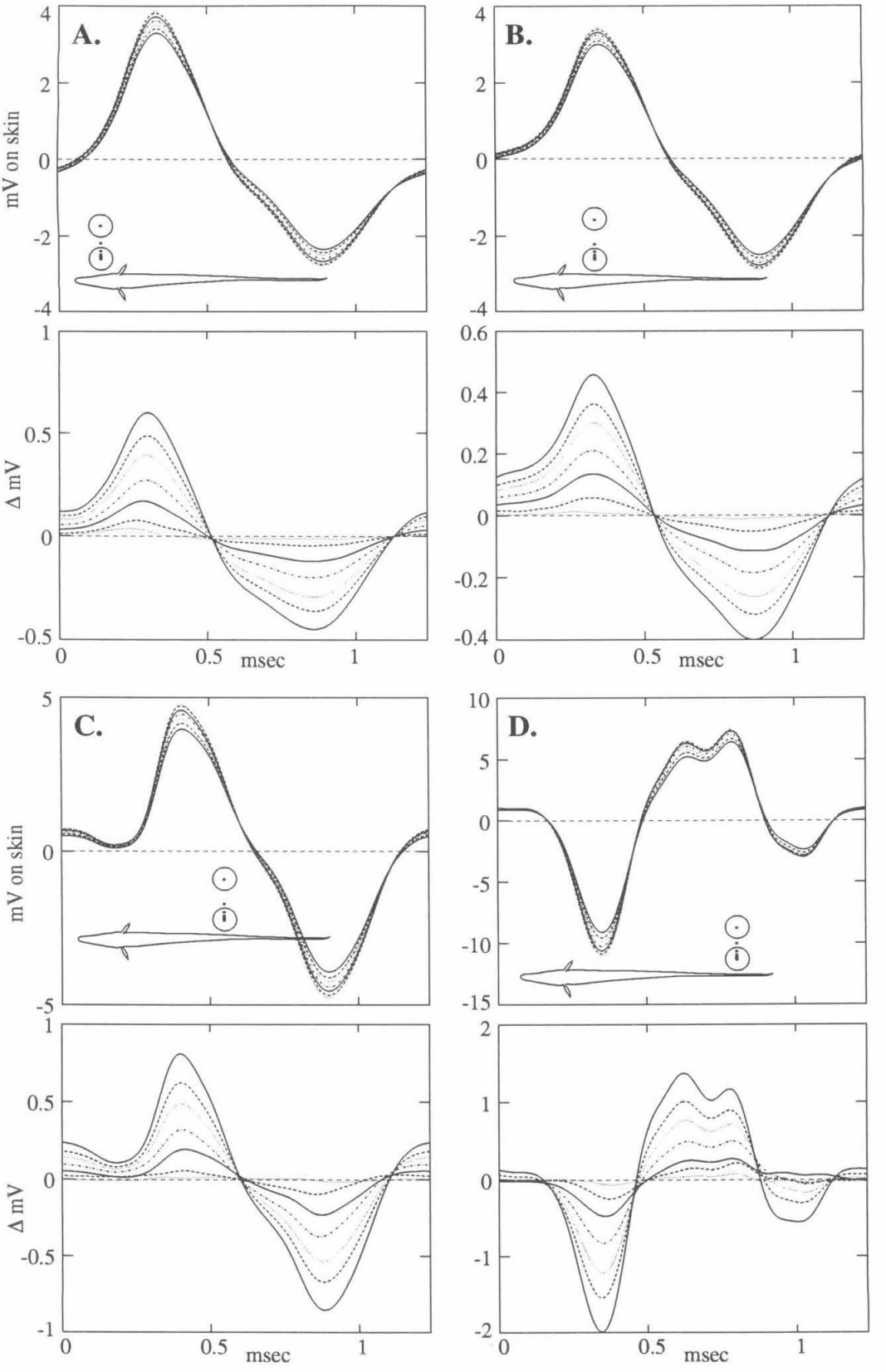
A.
B.
C.
D.
mV on skin
Δ mV
msec
0.5
0
1

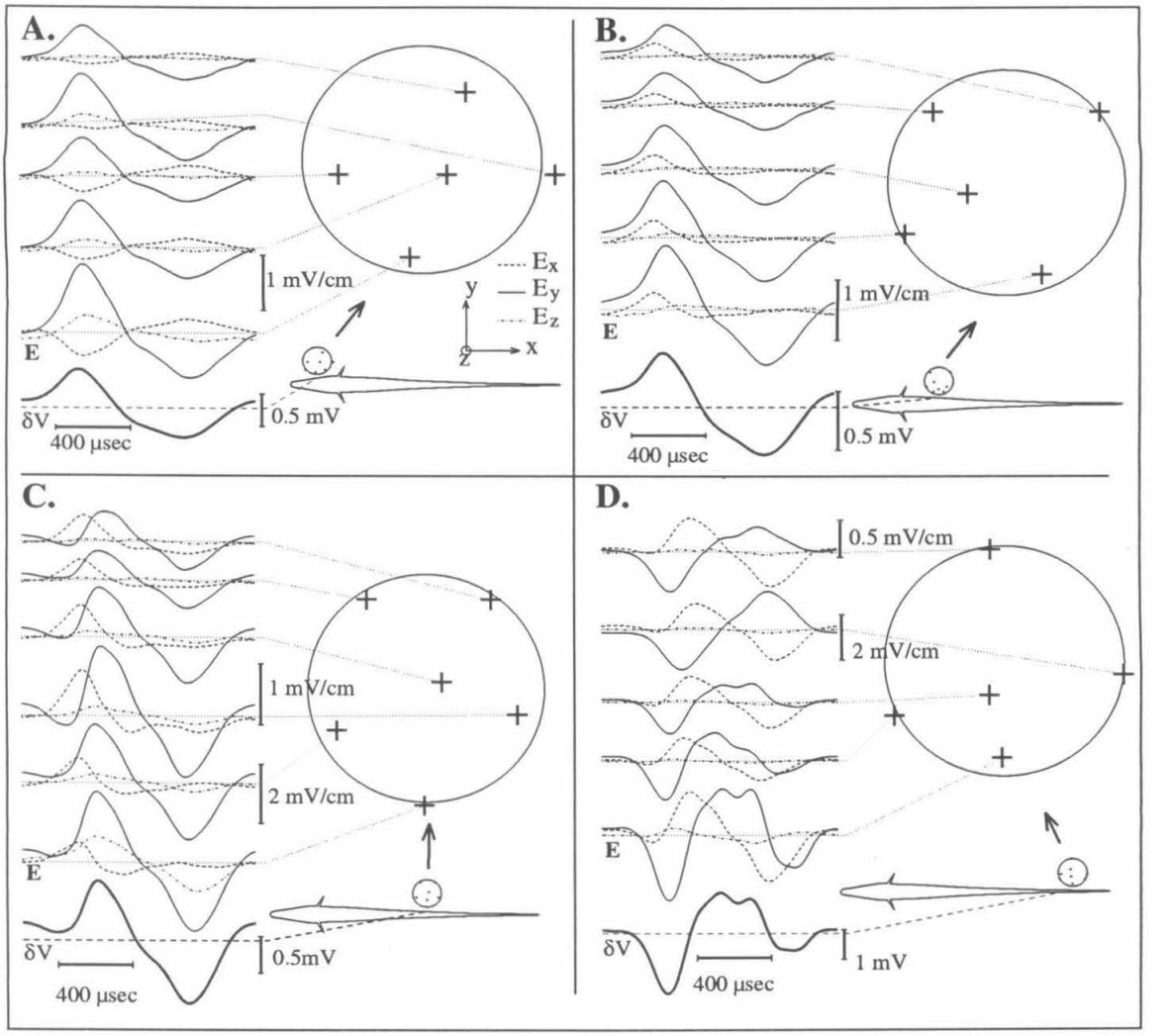

Figure 5.2. A. The Cartesian electric field components are shown at several locations which will be within or near the metal sphere at its closest position to the fish. The potential perturbation, measured on the fish's skin with the object at this position (lowest waveform) is similar to the lateral electric field component (E_y). The figure is repeated in B-D at three other rostrocaudal locations. The electric field becomes much more variable near the tail.

Figure 5.2 shows the electric field components in the area of the midplane that was occupied by the sphere. At the head, the waveform of the object modulation (Fig. 5.2A, lowest curve) is similar to the lateral electric field. At the tail (Fig. 5.2D), the electric field is much more variable over the area of the object. Of the two positive peaks of the lateral field at D, the first peak is largest at the rostral side of the object and the second peak is dominant caudally. The perturbation caused by the object closely resembles the lateral field waveform near the lower center of the object. We next quantitatively compare the measured potential changes on the fish's skin with the electric field.

Simulations of object waveforms

The simplest approach to simulate the object perturbation at the fish's skin is to treat the electric field as spatially uniform, with value equal to that at the center of the object's position. Directly below the object, Eqn. 5.2 reduces to:

$$\delta\varphi(y) = \frac{a^3 E_{0y}}{y^2} \qquad (5.4)$$

where y is the lateral distance between the fish's skin and object center. The simulated potential perturbation is independent of the tangential components of the electric field.

Figure 5.3 shows the simulated and measured waveforms of the perturbation potential below the object at four lateral distances and at four rostro-caudal positions. The amplitudes of the simulations and measurements generally agree, although the waveforms differ slightly. The largest difference between simulation and measurement occurs at the most caudal position with the object nearest the fish, precisely where the electric field is least spatially uniform. If instead of using E_y at the object's center for this simulation, we had used E_y at a point slightly rostral, there would be much closer agreement between the simulations and measurements.

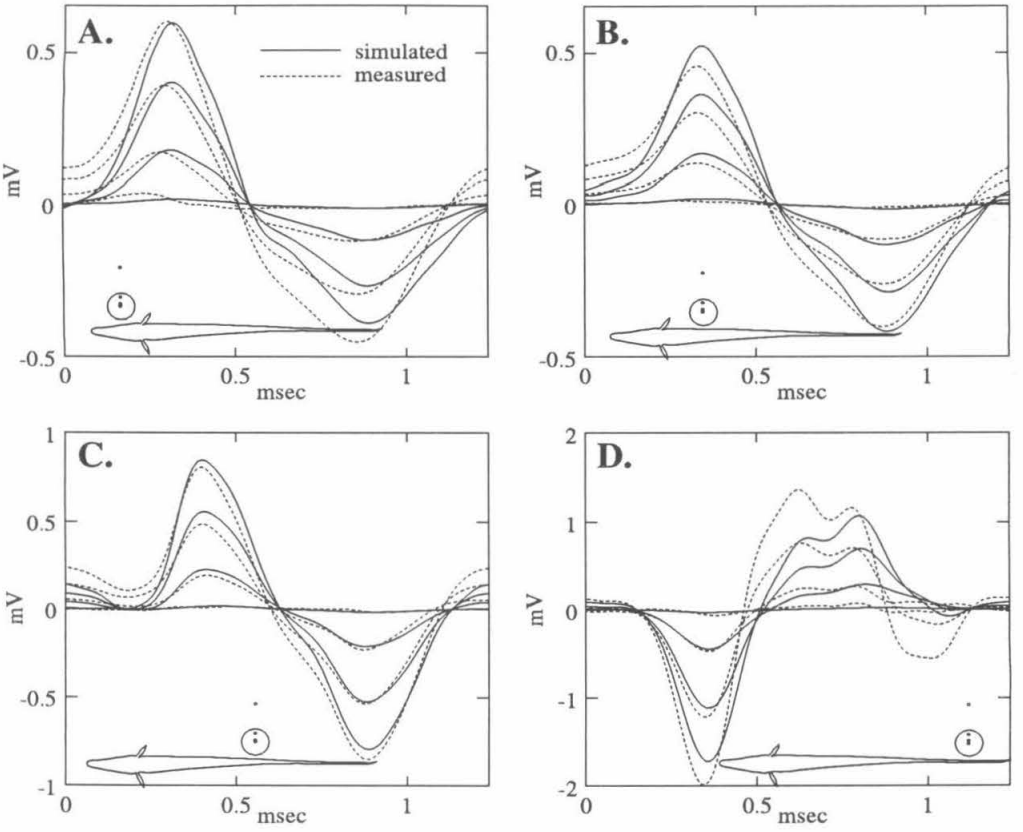

Figure 5.3. Simulated and measured potential perturbations are compared at four rostrocaudal positions. The object was a 11 mm radius brass sphere at distances of 13, 15, 20, and 43 mm between the center of the object and the fish's skin. The average amplitudes generally agree, although the waveforms differ slightly between the two methods.

Fourier analysis of the waveforms in Fig. 5.3 reveals a 12-20° phase lag between the simulated and measured fundamental frequencies at each rostrocaudal location, which is independent of the object-fish distance. The phases of the harmonics tend to agree within a few degrees when the object is nearest the fish's body, but diverge with increasing object distance. However, the amplitudes of the fundamental and all harmonics closely agree. This suggests a more sophisticated model of the object and the fish's field is required to accurately predict the phase shifts induced by this object.

Amplitude vs. lateral distance

The RMS amplitude of the object perturbation as a function of object distance from the fish is shown in Fig. 5.4. The measurements and simulations generally agree over two orders of magnitude. Far from the fish, the electric field is more uniform over the object, and thus the simulation may become more accurate. However the measured object perturbations become more susceptible to noise. At object-fish center-to-center distances

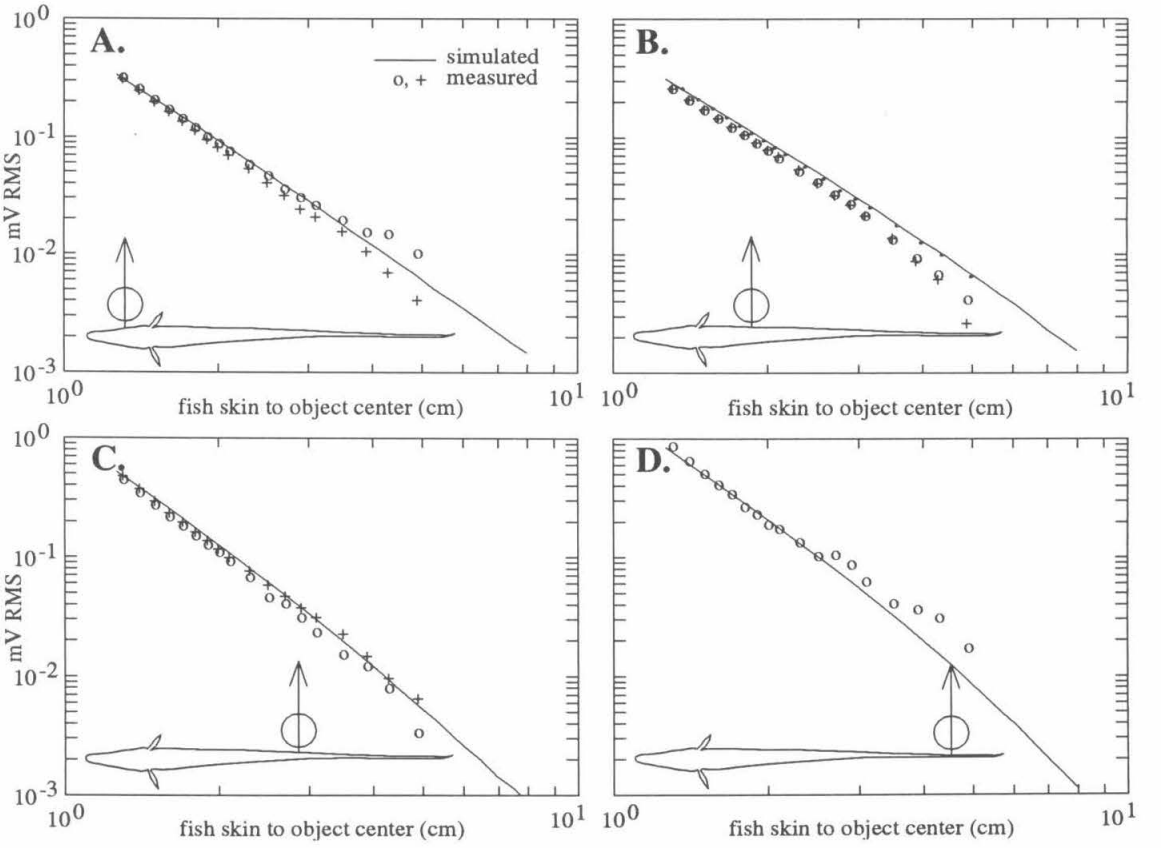

Figure 5.4. Simulated and measured RMS amplitude of the potential perturbation on the fish's skin below the object, as a function of object-fish distance. The sequence of measurements was repeated twice in A-C. In B, the dots represent the '+' measurements after two corrections were applied (see text).

greater than approximately 4 cm, the perturbation amplitude is less than one percent of the EOD. Therefore the measured image is a small difference between two large measurements, which is an unfavorable condition for data analysis due to error propagation.

In Fig. 5.4B, the measured amplitudes are consistently less than the simulation, and attenuate more quickly in the far field. These anomalies were explored numerically to uncover possible systematic errors. A single erroneously low EOD measurement without the object would result in an accelerated decay. Adding a 4 μV offset to the measured 1.85 mV EOD with the object at infinity (a 0.2% correction) eliminates this anomaly. However, it still leaves all the measurements consistently below the simulated amplitudes. This could result from the series of object measurements being slightly further from the fish. A systematic error of 0.5 mm would explain this difference. Measured values with these two corrections applied are shown as dots in Fig. 5.4B. Both these errors are reasonable. As shown in Chapter 4, the EOD amplitude variance is of this order of magnitude. The object-fish distance was determined by positioning the object against the fish's skin to calibrate a manipulator, and subsequently the electrode array was placed against the fish. It is possible that while positioning the array against the fish's skin, the electrodes could have pushed the fish's body further from the object. Furthermore, measuring absolute distances near the fish to submillimeter resolution, given the optical distortions due to the water, plexiglass tank, and the object, is a difficult task.

The simulated data from Fig. 5.4 are shown together in Fig. 5.5. For small lateral distances, perturbations from objects at the tail are much larger than for equidistant objects near the head. This is because the electric field is larger at the tail, and the perturbation is proportional to the lateral electric field (Eqn. 5.4). Like the electric field, the perturbations attenuate more rapidly with lateral distance at the tail. The average decay rate or the slope in Fig. 5.5 was computed by least squares fit to a power law: perturbation amplitude $\propto$ (fish surface to object center distance)$^{-\gamma}$. The average exponent, γ ranged from 2.9–3.6,

with larger values near the tail. For objects beyond several centimeters from the tail, γ is slightly greater than four.

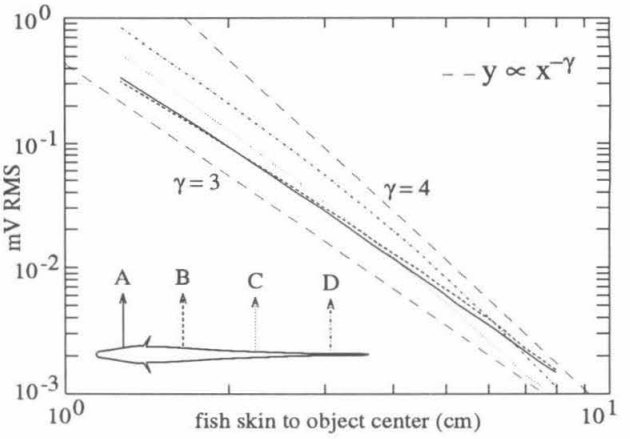

Figure 5.5. RMS amplitude of the simulated EOD perturbation below a 1.1 cm radius conducting sphere, at four rostrocaudal positions. The amplitudes decay as distance to the –2.9 to –4th power.

Images across the skin

We next examine the spatial properties of electric images in the midplane. The potential modulation on the fish's skin was recorded with an array of 5 flexible electrodes approximately 0.5 cm apart (the measurements shown above were from just the central electrode). Fig. 5.6 shows simulated and measured potential images for the same object positions as in Fig. 5.3. Although the measurements show considerable variance, they generally agree with the simulations. The electric images broaden as the object recedes from the fish, and the peaks of the images are slightly offset from the location of the object. These phenomena are explored further below (Fig. 5.8).

The simulator permits us to dissect the relative contributions of different electric field components to an object's electric image. Fig. 5.7 shows the simulated electric images of a 1 cm radius conducting sphere at four orientations of the electric field that occur during the EOD cycle. Even when the electric field is nearly tangential to the fish's skin (phase 1), there is a finite perturbation. Furthermore, this orientation of the electric

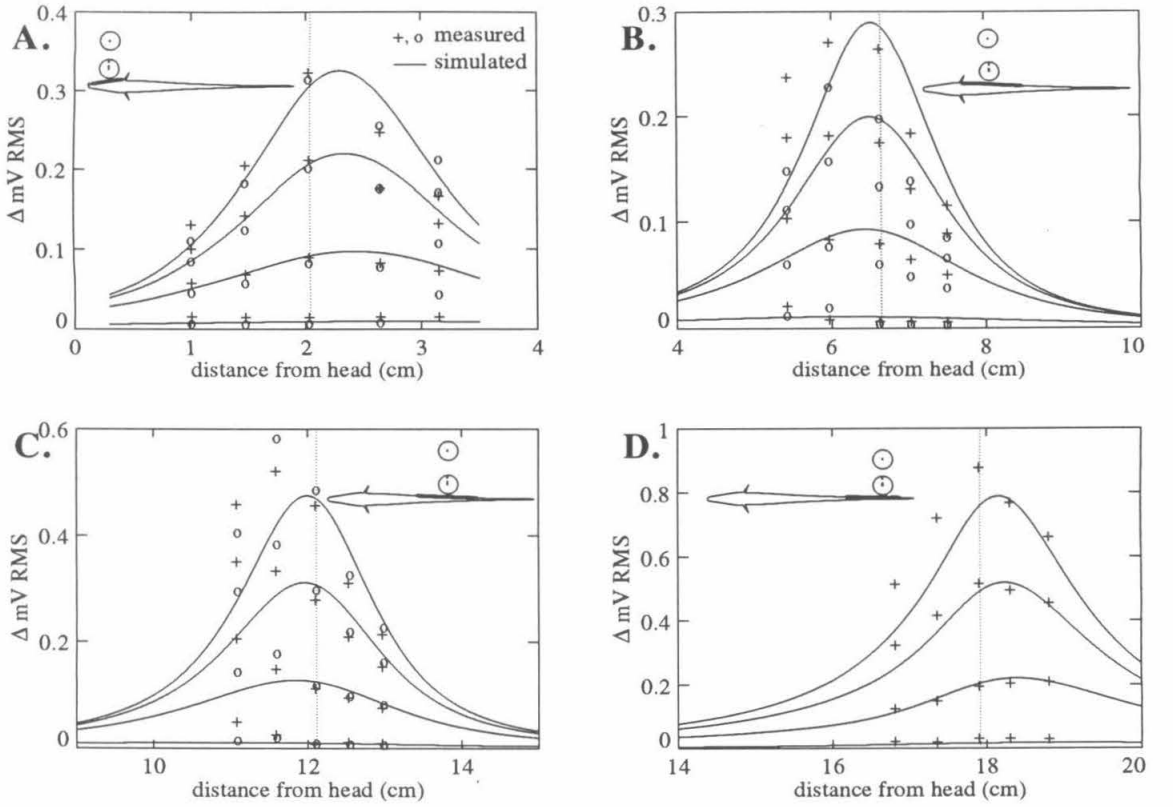

Figure 5.6. Simulated and measured potential perturbations for the same object positions as in Fig. 5.3. The vertical lines indicate the rostrocaudal locations of the object center.

field creates the largest amplitude perturbation at the flanks of the electric image, rostral and caudal of the object (arrows in Fig. 5.7B). The influence of the rostral electric field is largest rostral and caudal of the object because the local perturbation is:

$$\delta\varphi \propto \mathbf{E} \cdot \mathbf{r} \propto E_{rostral} \sin\theta + E_{lateral} \cos\theta \qquad (5.5)$$

where θ is the angle between the object and the normal vector at the measurement point on the fish's skin. Moving along the body away from the point below the object increases θ and the influence of the rostral field.

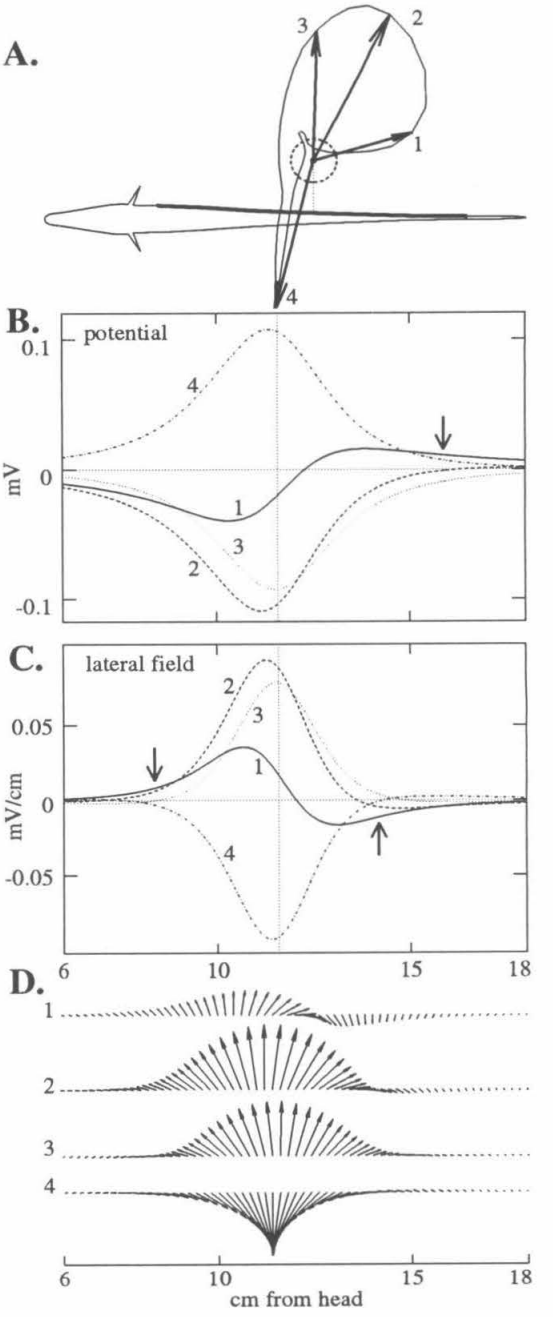

Figure 5.7. A. The outline of the electric field vector is shown at a point where the perturbation of a 1 cm radius conducting sphere is simulated. The potential perturbation (B) and the perturbation of the lateral electric field (C) on the bolded region of the fish's skin at the four EOD phases denoted by arrows in A. Even when the electric field at the object is nearly tangential to the skin (phase 1), the perturbations are significant, and in the locations shown by arrows, exceed the perturbations of the other phases. D. Vector representation of the simulated electric field perturbation during the same four phases of the EOD.

The simulator can also predict the object's effect on the electric field or current at the fish's skin (Fig. 5.7C). The perturbed field decays more rapidly with distance from the object than the corresponding potential, thus the field image is spatially more compressed across the fish's skin. Regarding signs, a conducting sphere causes a local

increase in lateral current and electric field below it. This results in a larger voltage drop over the skin, and consequently a decrease in potential on the outside surface of the skin relative to a distant electrode.

Figures 5.6 and 5.7 show the peaks of the electric image are displaced along the body relative to the position of the object. Consequently the receptors slightly rostral of the object in Fig. 5.7 will respond most vigorously. Figure 5.8A and B show the amount and direction of this offset at several object positions. The offset occurs because the electric field is not normal to the fish's body. The dipole moment of the perturbation is parallel to the electric field (Eqn. 5.1), thus the projection of the dipole lobes on the skin will have their maxima displaced towards where the field vector intersects the fish's skin. The direction of the fish's electric field was shown in Fig. 4.7, and is consistent with the direction of the measured offsets. The curvature of the fish's body also contributes to the peak's offset. Receptors on the skin where the body curves away from the object are further from the object, and thus detect a more attenuated signal than they would if the body were flat.

Electric images can be characterized by their sharpness or spread across the fish's skin. Figure 5.8C and D shows a measure of the image's size as a function of the object's lateral distance and rostrocaudal position. The width of the image at half its peak amplitude increases linearly with object distance for objects near the fish. The slope for the potential image is approximately 1.5. Data was limited to nearby objects at the head and tail because the image at the edge of the fish's body exceeded half the peak amplitude.

The lateral electric field perturbation (Fig. 5.8D) is both narrower and widens with object distance slower than the potential image. However, like the potential image, the slope is smallest at the head and increases monotonically at the four rostrocaudal positions. This suggests that the spatial resolution of electric sense could be higher at the head than at the tail, and less variable with object distance. Note that this result is

independent of object radius and impedance, which globally affect the amplitude (and phase), but not the relative shape of the electric image (Eqn. 5.1).

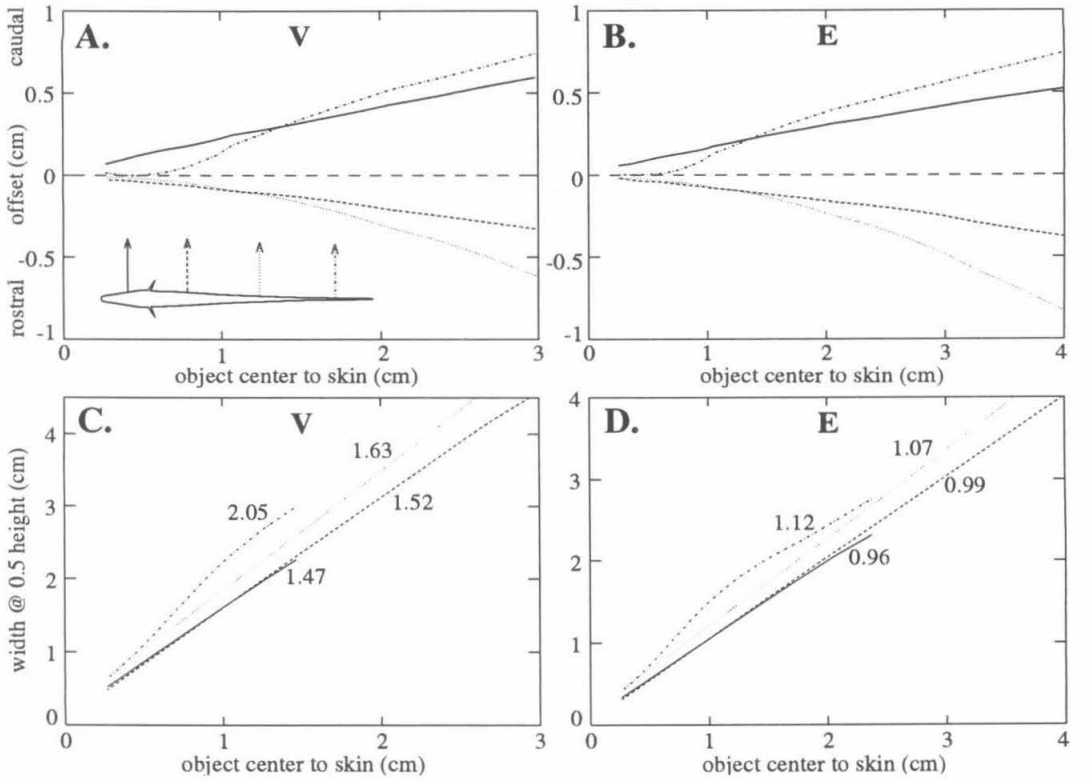

Figure 5.8. The location of the electric image peak is slightly offset from the location of the object. A and B shows how the location of the peak changes as the object is moved away from the fish at four rostrocaudal positions. The locations of the peaks of the potential images and lateral electric field images are similar. C,D. The width of the electric image at half the peak amplitude increases nearly linearly as the object moves away from the fish's body. The numbers give the slope of the curves at the four rostrocaudal locations.

5.4. Discussion

In this study, we have attempted to build an intuition of how weakly electric fish might perceive objects with their high frequency electric sense. We used measurements of potential changes due to a large metal sphere to test the accuracy of a simple semi-analytical model. Despite its oversimplified assumptions, the model quantitatively and qualitatively reproduces many aspects of the measured object perturbations.

We have characterized object perturbations by their amplitude and spatial extent on the fish's skin. This is different from the perspective taken by Bastian [11], which examined the effect of moving objects past single electroreceptors on the fish's skin. Modeling an object as a dipole was first proposed by Bacher [12]. However, Bacher used a pair of line charges to model the fish's unperturbed electric field, and his general solution was in terms of an integral, which we have solved in Eqn. 5.1. We have also defined object distance unconventionally. Whereas it is natural experimentally to measure object distance between the fish's skin and the sphere's surface, the sphere's effects have a simpler functional form in terms of the distance to its center–the point of symmetry of its perturbation. Including the sphere's radius in its distance from the fish has a major influence on the analysis results.

To maximize signal-to-noise ratio, a 22 mm diameter metal sphere was chosen for a test object. Even with the edge of this huge conductor just 2 mm from the fish's skin, the potential between the fish's skin below the object and a distant electrode changed by less than 15 percent. This implies that most of the voltage drop from the EO occurs within the fish. The bulk skin and body of *Apteronotus* have resistivity of approximately 3 kΩ-cm^2 and 300 Ω-cm respectively at the trunk (unpublished measurements and [13]). Therefore most of the potential is across the fish's skin for nearby objects. Since neither the distant reference nor the internal side of the skin are significantly affected by an object, near the fish, the change in potential across the fish's skin (outside–inside) is approximately equal to the change in potential at the skin surface relative to a distant

electrode. Recording the potential relative to a distant electrode eliminates trauma and possible distortion of the electric field at the insertion point of the internal electrode.

Accuracy of the simulator and measurements

Although we use the terms "simulated" and "measured" to label the two methods of deriving electric images, the simulation is based on actual measurements of the unperturbed electric field. The measurements of the fish's electric field components were done simultaneously and differentially, and are thus not as sensitive to EOD variance and instrumentation noise as the measured perturbations. Since the simulated perturbation is proportional to the electric field, only the relative error in the field contributes to its uncertainty. In contrast, the measured perturbations are extremely sensitive to measurement errors (e.g., Fig. 5.4B). Variations of the EOD amplitude by 0.1% during the few minutes that the object was moved from near the fish to infinity can result in a 10% uncertainty of a 1% amplitude modulation. Large common mode signals also require greater precision of the electronic instrumentation, since nonlinearities such as interchannel crosstalk and harmonic distortion are typically proportional to the signal.

There are two major assumptions in the simulator model that are of questionable validity. The unperturbed electric field is assumed uniform over the volume of the object. This is clearly violated, especially near the fish's tail, and to a lesser degree at the trunk and further from the fish (Fig. 5.2). Had we chosen a smaller object, the electric field would have been more uniform, but the perturbation amplitude would have decreased as the cube of the object radius, proportionally reducing the signal-to-noise ratio. A nonuniform field induces a dipole moment proportional to the mean field, and additional higher multipole perturbations. The multipoles attenuate with distance from the object more rapidly than the dipole, and from the data, appear to be relatively weak at the fish's skin, except perhaps near the fish's tail (Fig. 5.3D). Much of the discrepancy between measurement and simulation at the tail could also be the result of a small error in the

rostrocaudal location of the object, since the electric field waveform significantly changes over millimeter distances (Fig. 5.2D).

A second assumption in the model is that there is no fish, i.e., the perturbation at the fish's skin is not affected by the fish's presence. A 1 cm^2 section through the fish's trunk should have a resistance of approximately $R \approx (1\ cm^2)\ (2\ \rho_{skin} + \rho_{body} * 1\ cm) \approx 6\ k\Omega$. The same size section of water has resistance of just over 5 $k\Omega$. We have also already seen that the object perturbation is a small effect on the overall electric field. Therefore the fish should exert a relatively minor affect on the simulation result.

In comparing the object measurements with the simulations, we assumed the brass sphere was a perfect conductor. However metals in water are subject to complicated chemical reactions at their surface that can cause large deviations in their behavior from that of a perfect conductor [14]. For example, the metal surface rapidly oxidizes, and the sphere becomes analogous to a leaky capacitor with the water. It is possible that this is the cause of the observed phase shift between the measured and simulated waveforms. This will be explored in a future study by characterizing the perturbation caused by the sphere in a uniform field. Although the perturbations from insulating spheres are half the amplitude of conducting ones, they should be free of these complex surface phenomena.

In summary, the simulations of object perturbation amplitudes generally agree with measurements to within the uncertainties of the measurements. The simulator accuracy should improve with increasing object distance and decreasing object size, precisely the conditions that are most difficult to accurately measure. The simulator is quite robust to the violations of its assumptions even for large objects very close to the fish. Although it does not predict as accurately the phase shifts due to a metal sphere, this may result from the sphere deviating from an ideal conductor.

Range of active electrolocation

There are several ways to characterize the attenuation of electric images with increasing fish-object distance. When fitting the image amplitude to a functional form,

such as a power law, (distance)$^{-\gamma}$, the distance can be measured from the skin or midline of the fish, to the edge or center of the object, and each choice results in different values for γ. The dipolar perturbation at the fish's skin due to a sphere has the simplest functional form in terms of distance from the fish's skin to the center of the sphere (Eqn. 5.1). Using this scale, least squares fit yields $\gamma = 2.9$ at the head and trunk, which increases caudally to slightly over 4.0 at lateral distances greater than several cm at the tail (Fig. 5.5). The decay rate of the lateral electric field, as a power of distance from the fish's *centerline* was shown in Chapter 4 to be $\gamma_E = 1.2$ at the head and 2.0 at the tail (Fig. 4.8D). From Eqn. 5.4, the object perturbation decays proportionally to the lateral field and the (distance between the object center and the fish's *skin*)$^{-2}$. The distance from the fish's skin to the fish's centerline decreases the decay exponent slightly from $\gamma_E + 2$. We also compared these results with those of Bastian [11]. His decay exponents were around 1.2, because he fitted the amplitude to the distance between the fish's skin and object surface. Reanalysis of some of his data (the highest curve in Fig. 8C of [11]; it is not evident where on the body this data comes from), gives a decay rate of 3.1 in our units. Furthermore, his data fits much closer to this power law over the entire range of object distances.

Although the amplitude of electric images is proportional to the cube of the object radius (Eqn. 5.1), the rate of attenuation with lateral distance is independent of the radius. Thus for a given object, it should be a simple matter to compute a maximum distance at which it will cause sufficient perturbation to be detected by an electroreceptor. Electroreceptor sensitivity thresholds have been estimated in several studies, based on behavioral thresholds [15]; electroreceptor responses to objects and applied fields [11], [16]; and simulations [17]. However, correlating the perturbation amplitude to electroreceptor stimulus is complicated because the receptors do not respond only to the EOD amplitude. P-receptors adapt to continual stimulus, with a time "constant" of 0.5–3.5 seconds (the adaptation time depends on stimulus amplitude) [16]. These receptors have

other complicated temporal filtering properties [11] as well as directional preferences [18]. Additionally, electroreceptors are more sensitive than the apparatuses that have been used to study them, so their thresholds were usually extrapolated from larger perturbations. Thus, electroreceptor thresholds should only be interpreted as rough estimates.

Applying a uniform field at the EOD frequency between distant plates lateral to the fish, Knudsen observed behavioral responses to field strengths as low as 0.2 μV/cm [15]. Measuring the response of single electroreceptor afferents to the same kind of stimulus, Bastian found a 20 μV/cm field caused a measurable change in electroreceptor firing rate of 20 Hz [11]. He extrapolated that a field strength of 0.9 μV/cm would cause a 1 Hz change in firing rate, which suggests that *Apteronotus* can achieve its behavioral threshold by averaging over approximately 20 receptors. Bastian also measured the change in transdermal potential between electrodes on the skin and inside the fish's gut caused by moving metal spheres. He related a change in transdermal potential of x mV caused the same change in receptor firing rate as an applied field with strength $0.84x$ mV/cm. This suggests that electroreceptor thresholds may be on the order of 1 μV. Another threshold estimate by Bastian is that of a 6.4 mm diameter metal sphere at a distance of 8 mm (skin to edge) [4], or 11.2 mm between the skin and sphere's center. Extrapolating from Fig. 5.5 to this distance from the trunk, and attenuating the amplitude by the cube of the ratio of the radii, yields a threshold of 10 μV. From Fig. 5.5, the 1 μV threshold corresponds to a 9 cm maximum range for the 2.2 cm diameter sphere lateral of the head and trunk, and an 8 cm range lateral of the tail. A 10 μV threshold yields a maximum range around 4.2 cm over the trunk and 4.7 cm at the tail.

Whereas our 2.2 cm sphere has a similar range of detectability along the fish's rostrocaudal axis, the same is not true of much smaller or larger objects. A smaller object will shift all the curves in Fig. 5.5 downward. This would result (assuming a constant threshold) in a greater range of detectability at the tail. Likewise, extrapolating the trends

of the decay exponents, the threshold range for large objects would be greater at the fish's head and trunk. We hope these predictions will be tested experimentally.

Spatial resolution and localization of objects

The shape or relative amplitudes of electric images on the fish's skin are independent of a sphere's radius (Eqn. 5.1). Therefore the images shown in Fig. 5.6 will be the same for any size of sphere, to within a vertical scale factor. Compared to vision, electric images are extremely fuzzy. The fish can increase the resolution only by moving closer to the object. Whereas this was known previously [17], Fig. 5.8C shows that the spread of electric potential images, measured as the full width at half of peak amplitude, increases linearly with increasing object-skin distance. The slope is relatively constant over the rostral part of the body. This suggests a very simple algorithm for determining a spherical object's distance, and resolving the difference between a nearby small sphere and a more distant and larger one. The fish would only need to determine the size of the electric image at a particular amplitude relative to the peak. Since fish-object distance may be one of the most important parameters to a fish, we suggest that physiologists look for neurons within the electrosensory tract that encode these features.

The location of an object is another parameter of critical importance. Fig. 5.8A shows the peaks of the electric image lie within a few mm of the rostrocaudal position of the sphere. The offset increases slowly with increasing object distance compared to the broadening of the electric image. For example, the width at half height of an object 3 cm from the fish is 4–5 cm, and the maximum offset of the peak relative to the object position is 0.5 cm. Thus objects are approximately located above the peak in electroreceptor activity, and the offset error becomes less as the object and fish become closer. More accurate localization could be achieved by considering the unperturbed electric field direction, and the already established object's distance.

Nonconducting and nonspherical objects

Thus far we have focused our attention on the electric images of conducting spheres. However the simulator permits exploration of the effects of homogeneous spheres with general linear electrical properties. Eqn. 5.3 describes the perturbation due to typical insulators such as most (spherical) rocks, with $\rho_2 >> \rho_1$ and $\varepsilon_2 \leq \varepsilon_1$. The perturbation has opposite sign and half the amplitude relative to ideal conductors. If the fish's environment contained only ideal conducting and insulating spheres, the sign of the perturbation could be used to determine the object's impedance. The proposed algorithm for determining the object's distance is equally applicable to nonconductors because it depends only on relative amplitudes and their locations. Knowing the conductivity and distance, the object's size could be determined from the magnitude of the peak perturbation. Spheres with time constants ($\tau = \rho\varepsilon$) of the order of the EOD period will produce intermediate magnitudes and phase shifts relative to E_o. Therefore impedance and size remain confounded. For example, a large sphere with impedance slightly different from the water could have a similar dipole moment amplitude as a smaller sphere with a greater difference in impedance. The phase of the perturbation, however would be different in these two cases. Weakly electric fish are extremely sensitive to phase and temporal shifts in their EOD. Thresholds as low as 0.4 μsec have been measured in some species [19].

The literature contains sparse references to the electrical properties of aquatic objects that electric fish naturally encounter. Many biological objects have huge dielectric strengths, because of their thin membranes and high concentrations of polar molecules. Heiligenberg measured the resistivity and capacitance of the leaves of two species of aquatic plant that provide camouflage for *Eigenmannia* [20]. *Hygrophilia* has resistivity ρ_2 = 200 kΩ-cm, capacitance C = 76 nF/cm^2, and a thickness of 0.2 mm. This corresponds to a dielectric constant ε_2 = 1.6 nF/cm. Imagining a spherical "leaf" of this material, in

water with $\rho_1 = 5$ kΩ-cm and $\varepsilon_1 = 80\varepsilon_0 = 7$ pF/cm, the perturbation becomes (from Eqn. 5.1):

$$\delta\varphi(\mathbf{r}) = \frac{a^3\mathbf{E}_0 \cdot \mathbf{r}}{r^3}\left(\frac{-195 + i10.1f}{405 + i10.1f}\right) \tag{5.6}$$

where f is the harmonic frequency in kHz. At the 800 Hz fundamental frequency of this fish, the complex term is –0.48 + 0.03i, only slightly different from a rock (a 3.5 degree phase shift). The lowest *k* harmonics are shifted by approximately 3.5*k* degrees (as long as $\sin\theta \approx \theta$). This result does not imply that *Hygrophilia* has insignificant effect on EOD phase, for the geometry of actual leaves may considerably increase their capacitive effects.

The phase shift of "spherical *Hygrophilia*" becomes much larger in higher resistivity water. Seasonal variation in rainfall cause water resistivity changes of several orders of magnitude. *Apteronotus* normally experiences water resistivity between 2 kΩ-cm in the dry season to 100 kΩ-cm in the rainy season [15]. In 50 kΩ-cm water, the complex term in Eqn. 5.6 becomes –0.29 + 0.23i at 800 Hz, or in polar coordinates, –0.37 at a phase of 38°. This suggests that the electric images of certain objects may dramatically change with seasonal periodicity, and even change over hours due to heavy rains. This raises questions about whether and how electric fish may achieve invariant perceptions of such objects.

We have also begun to investigate how robust the above results are for nonspherical objects by simulating the perturbation due to an ellipsoid. A general ellipsoid is defined by the surface:

$$\frac{x^2}{a^2} + \frac{y^2}{b^2} + \frac{z^2}{c^2} = 1. \tag{5.7}$$

The analysis is greatly simplified by making the cross section along one axis symmetrical, i.e., setting a = b. The perturbation potential at a distance $\mathbf{r}=(x,y,z)$ from such a conducting ellipsoid is (modified from [21]):

$$\delta\varphi(\mathbf{r}) = \left(xE_x + yE_y\right)\frac{\Psi\left(\frac{u}{v}\right) - \frac{uv}{\xi + a^2}}{\Psi\left(\frac{u}{c}\right) - \frac{uc}{a^2}} - zE_z\frac{\Psi\left(\frac{u}{v}\right) - \frac{u}{v}}{\Psi\left(\frac{u}{c}\right) - \frac{u}{c}} \tag{5.8}$$

where $\Psi(\upsilon) = \tanh^{-1}(\upsilon)$ for an oblate spheroid (a=b<c) or $\Psi(\upsilon) = \tan^{-1}(\upsilon)$ for a prolate spheroid (a=b>c); E_x, E_y, and E_z are the electric field components at the center; ξ is analogous to the radial spherical coordinate, defined by:

$$\frac{x^2 + y^2}{a^2 + \xi} + \frac{z^2}{c^2 + \xi} = 1 \tag{5.9}$$

and u and v are given by:

$$u = \sqrt{\left|a^2 - c^2\right|}, \quad v = \sqrt{c^2 + \xi}\,. \tag{5.10}$$

The shapes of the perturbations for some ellipsoids with eccentricity of 2 are similar to spheres. However, for more eccentric and large objects, this algorithm breaks down. In these cases, nonuniformity of the electric field and asymmetry of the objects may generate additional spatial features and multipole moments in the electric images.

Rostro-caudal differences and other electrolocation cues

We have shown in this and the previous chapter several parameters that differ between the rostral and caudal regions of the fish. In summary, at the tail, the field is larger; less uniform; has more temporal harmonics; has more directional components; and decays faster than at the head and trunk. Therefore object perturbations or electric images have greater amplitude, greater width across the body, and attenuate faster with lateral distance. It is difficult to attribute functional significance to these differences without knowing more about the respective electroreceptor populations. As we suggested in Chapter 3, the order of magnitude larger EOD at the tail requires that caudal electroreceptors have different sensitivities and/or spontaneous firing rates. The steeper attenuation of perturbations likewise implies rostrocaudal differences in gain and/or dynamic range as well. Because of the uncertainty in electroreceptor thresholds, it is

difficult to even conclude whether the range of active electrolocation is the same or different across the fish's body for a given sized object. Although we proposed that distant large objects will generate smaller perturbations at the tail than at the trunk, differences in receptor thresholds could compensate for these effects, as could the fish's behavior. Electric fish wag their tails at much higher velocities than they can move their bodies laterally. This could cause amplitude modulations of much higher frequency, to which the receptors have greater sensitivity. We also note that errors in determining an object's distance could result in collisions, which would be less injurious at the tail than at the much more massive (and perhaps more fragile) body.

Although we have primarily focused here on the amplitude of electric images, other EOD cues are involved in electrolocation. Perhaps most important is motion. Electric fish actively explore objects by moving their bodies and tails laterally and rostrocaudally around objects. Toerring and Belbenoit classified a repertoire of probing motor acts used by a mormyrid while exploring novel objects [22]. Similar work is underway with *Apteronotus* in our lab (Assad, personal communication). Once the exploratory movements of *Apteronotus* are stereotyped, the simulator can model object motion by a sequence of images.

We have also restricted our view of electric images to the fish's midline. Although it is a simple matter to compute images on the fish's 2-dimensional surface, visualizing the additional dimension becomes more involved. This will probably take on greater importance for analysis of images produced by moving and asymmetrical objects.

Finally, the phase distortions caused by objects are of interest because of the acute phase sensitivity of electric fish. Most behavioral assays of electrolocation to date have dealt with the fish's ability to distinguish metals from water and insulators, or resistive and capacitive shunts [23], [24]. We hope these results will promote experiments to determine how well electric fish are able to discriminate shape, size, and conductivity of natural objects.

References

[1] Bastian, J., "Electrosensory Organisms," *Physics Today*, **47**:30-37, 1994.

[2] Kalmijn, A.J., "Detection of Weak Electric Fields," in *Sensory Biology of Aquatic Animals*, Atema, J., Fay, R., Popper, A., and Tavolga, W. (Eds.), pp. 151-186, Springer Verlag, 1986.

[3] Rasnow, B., Assad, C., and Bower, J.M., "Phase and Amplitude Maps of the Electric Organ Discharge of the Weakly Electric Fish, *Apteronotus leptorhynchus*," *J. Comp. Physiol.*, **172**:481-491, 1993.

[4] Bastian, J., "Electrolocation," in *Electroreception*, Bullock, T.H. and Heiligenberg, W. (Eds.), pp. 577-612, Wiley & Sons, 1986.

[5] Bullock, T.H. and Heiligenberg, W., *Electroreception*, John Wiley & Sons, Inc., 1986.

[6] Bennett, M.V.L. and Shosaku, O., "Ionic Mechanisms and Pharmacology of Electroreceptors," in *Electroreception*, Bullock, T.H. and Heiligenberg, W. (Eds.), pp. 157-182, Wiley, 1986.

[7] Carr, C.E., "Neuroethology of Electric Fish," *BioScience*, **40**:259-267, 1990.

[8] Scheich, H., Bullock, T.H., and Hamstra, R.H., "Coding Properties of Two Classes of Afferent Nerve Fibers: High-Frequency Electroreceptors in the Electric Fish, *Eigenmannia*," *J. Neurophys.*, **36**:39-60, 1973.

[9] Nelson, M.E., Payne, J.R., and Xu, Z., "Modeling and Simulation of Primary Electrosensory Afferent Response Dynamics in the Weakly Electric Fish, *Apteronotus leptorhynchus*," *J. Comp. Physiol. A*, **173**:746, 1993.

[10] Yager, D.D. and Hopkins, C.D., "Directional Characteristics of Tuberous Electroreceptors in the Weakly Electric Fish, *Hypopomus* (Gymnotifromes)," *J. Comp. Physiol.*, **173**:401-414, 1993.

[11] Bastian, J., "Electrolocation I. How the Electroreceptors of *Apteronotus albifrons* Code for Moving Objects and Other Electrical Stimuli," *J. Comp. Physiol.*, **144**:465-479, 1981.

[12] Bacher, M., "A New Method for the Simulation of Electric Fields, Generated by Electric Fish, and their Distorsions by Objects," *Biol. Cybern.*, **47**:51-58, 1983.

[13] Bennett, M.V.L., "Electroreception," in *Fish Physiology*, Hoar, W.S. and H., R.D. (Eds.), pp. 493-574, Academic Press, 1971.

[14] Robinson, D.A., "The Electrical Properties of Metal Microelectrodes," *Proc. IEEE*, **56**:1065-1071, 1968.

[15] Knudsen, E.I., "Behavioral Thresholds to Electric Signals in High Frequency Electric Fish," *J. Comp. Physiol.*, **91**:333-353, 1974.

[16] Hopkins, C.D., "Stimulus Filtering and Electroreception: Tuberous Electroreceptors in Three Species of Gymnotid Fish," *J. Comp. Physiol.*, **111**:171-207, 1976.

[17] Heiligenberg, W., "Theoretical and Experimental Approaches to Spatial Aspects of Electrolocation," *J. Comp. Physiol.*, **103**:247-272, 1975.

[18] McKibben, J.R., Hopkins, C.D., and Yager, D.D., "Directional Sensitivity of Tuberous Electroreceptors: Polarity Preferences and Frequency Tuning," *J. Comp. Physiol.*, **173**:415-424, 1993.

[19] Rose, G. and Heiligenberg, W., "Temporal Hyperacuity in the Electric Sense of Fish," *Nature*, **318**:178-180, 1985.

[20] Heiligenberg, W., "Electrolocation of Objects in the Electric Fish, *Eigenmannia* (Rhamphichthyidae, Gymnotoidei)," *J. Comp. Phys.*, **87**:137-164, 1973.

[21] Landau, L.D., Lifshitz, E.M., and Pitaevskii, L.P., *Electrodynamics of Continuous Media*, 2nd Edition, Pergamon Press, 1984.

[22] Toerring, M.J. and Belbenoit, P., "Motor Programmes and Electroreception in Mormyrid Fish," *Behav. Ecol. Sociobiol.*, **4**:369-379, 1979.

[23] Meyer, J.H., "Behavioral Responses of Weakly Electric Fish to Complex Impedances," *J. Comp. Physiol.*, **145**:459-470, 1982.

[24] von der Emde, G., "Discrimination of Objects Through Electrolocation in the Weakly Electric Fish, *Gnathonemus petersii*," *J. Comp. Physiol.*, **167**:413-421, 1990.

Appendix 1

A Sphere in a Uniform Electric Field

The perturbation due to a sphere in a uniform electric field can be solved as a boundary value problem. The adjacent figure shows the idealized problem. A sphere of radius a, with dielectric constant ε_2 and resistivity ρ_2, is located at the origin in a uniform horizontal electric field of magnitude E_o. The sphere is surrounded by media with dielectric constant ε_1 and resistivity ρ_1. We wish to solve for the electric field at a point **r** in region 1. There are no free charges near the sphere, thus we seek a solution to Laplace's equation and boundary conditions:

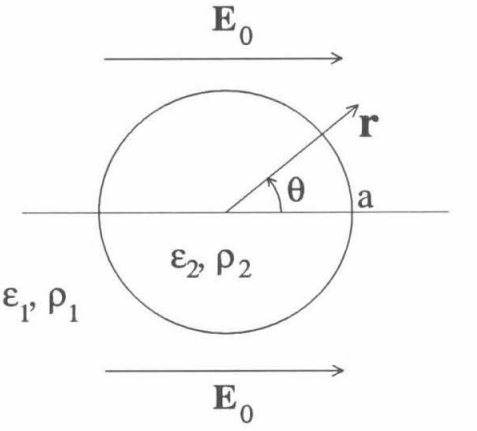

$$E_{1\tan} = E_{2\tan} \qquad \text{and} \qquad g_1 E_{1r} + \varepsilon_1 \frac{\partial E_{1r}}{\partial t} = g_2 E_{2r} + \varepsilon_2 \frac{\partial E_{2r}}{\partial t}$$

where $g = 1/\rho$ is the conductivity. Because of azimuthal symmetry, the potential in each domain can be written as Legendre series. Additional constraints are the potential at the origin must be finite. The perturbation from the sphere must tend towards zero at infinity, while the potential gradient approaches $\mathbf{E}_o$. These constraints force all the terms in the Legendre series to zero except:

$$\varphi_1(r,\theta) = -E_0 r\cos\theta + \frac{C}{r^2}\cos\theta \qquad \varphi_2(r,\theta) = Ar\cos\theta.$$

The two remaining constants are solved by the two boundary conditions at the surface of the sphere:

$$E_{1\tan} = E_{2\tan} = -\frac{\partial\varphi}{\partial\theta} \quad \Rightarrow \quad -E_0 a + \frac{C}{a^2} = Aa \quad \Rightarrow \quad A = \frac{C}{a^3} - E_0.$$

The second boundary condition can be simplified by assuming the potential (and $\mathbf{E}_o$) have sinusoidal time dependence:

$$\varphi(\mathbf{x},t) = \varphi(\mathbf{x})e^{i\omega t}.$$

The equations can be solved independently for multiple frequencies. The boundary condition reduces to:

$$(g_1 + i\omega\varepsilon_1)\left.\frac{\partial\varphi_1}{\partial r}\right|_{r=a} = (g_2 + i\omega\varepsilon_2)\left.\frac{\partial\varphi_2}{\partial r}\right|_{r=a}.$$

Defining $\xi = 1 + i\omega\varepsilon\rho$ simplifies the algebra, with the result:

$$C = \frac{\rho_1\xi_2 - \rho_2\xi_1}{2\rho_2\xi_1 + \rho_1\xi_2}E_0 a^3$$

or substituting back:

$$C = \frac{\rho_1 - \rho_2 + i\omega\rho_1\rho_2(\varepsilon_2 - \varepsilon_1)}{2\rho_2 + \rho_1 + i\omega\rho_1\rho_2(2\varepsilon_1 + \varepsilon_2)}E_0 a^3$$

and finally, the perturbation due to the sphere is given by:

$$\delta\varphi(\mathbf{r}) = \mathbf{E}_0 \cdot \mathbf{r}\left(\frac{a}{r}\right)^3 \frac{\rho_1 - \rho_2 + i\omega\rho_1\rho_2(\varepsilon_2 - \varepsilon_1)}{2\rho_2 + \rho_1 + i\omega\rho_1\rho_2(2\varepsilon_1 + \varepsilon_2)}.$$

This is the potential of a dipole with complex amplitude or phase shift. Simplification for special cases of ε and ρ are treated in Chapter 5.